sid.inpe.br/mtc-m21c/2021/03.04.13.54-TDI

DEM-BASED MORPHOTECTONIC ANALYSIS OF A PASSIVE CONTINENTAL MARGIN OF SOUTH AMERICA: NORTHERN PARAÍBA BASIN, NE BRAZIL

Fabio Corrêa Alves

Doctorate Thesis of the Graduate Course in Remote Sensing, guided by Drs. Márcio de Morisson Valeriano, and Dilce de Fátima Rossetti, approved in January 22, 2021.

URL of the original document:
<http://urlib.net/8JMKD3MGP3W34R/449LS8B>

INPE
São José dos Campos
2021

PUBLISHED BY:

Instituto Nacional de Pesquisas Espaciais - INPE
Coordenação de Ensino, Pesquisa e Extensão (COEPE)
Divisão de Biblioteca (DIBIB)
CEP 12.227-010
São José dos Campos - SP - Brasil
Tel.:(012) 3208-6923/7348
E-mail: pubtc@inpe.br

sid.inpe.br/mtc-m21c/2021/03.04.13.54-TDI

DEM-BASED MORPHOTECTONIC ANALYSIS OF A PASSIVE CONTINENTAL MARGIN OF SOUTH AMERICA: NORTHERN PARAÍBA BASIN, NE BRAZIL

Fabio Corrêa Alves

Doctorate Thesis of the Graduate Course in Remote Sensing, guided by Drs. Márcio de Morisson Valeriano, and Dilce de Fátima Rossetti, approved in January 22, 2021.

URL of the original document:
<http://urlib.net/8JMKD3MGP3W34R/449LS8B>

INPE
São José dos Campos
2021

Cataloging in Publication Data

Alves, Fabio Corrêa.

Al87d Dem-based morphotectonic analysis of a passive continental margin of South America: northern Paraíba Basin, NE Brazil / Fabio Corrêa Alves. – São José dos Campos : INPE, 2021.

xxii + 139 p. ; (sid.inpe.br/mtc-m21c/2021/03.04.13.54-TDI)

Thesis (Doctorate in Remote Sensing) – Instituto Nacional de Pesquisas Espaciais, São José dos Campos, 2021.

Guiding : Drs. Márcio de Morisson Valeriano, and Dilce de Fátima Rossetti.

1. Tectonic uplifiting. 2. Intraplate compression. 3. Far-field stress. 4. Late Pleistocene. 5. Remote Sensing. I.Title.

CDU 528.8:551.24(81)

MINISTÉRIO DA CIÊNCIA, TECNOLOGIA E INOVAÇÕES

INSTITUTO NACIONAL DE PESQUISAS ESPACIAIS

Serviço de Pós Graduação - SEPGR

Pós-Graduação em Sensoriamento Remoto

DEFESA FINAL DE TESE DE FABIO CORRÊA ALVES

No dia 22 de janeiro de 2021, as 09h00min, por teleconferência, o(a) aluno(a) mencionado(a) acima defendeu seu trabalho final (apresentação oral seguida de arguição) perante uma Banca Examinadora, cujos membros estão listados abaixo. O aluno foi APROVADO pela Banca Examinadora, por maioria simples, em cumprimento ao requisito exigido para obtenção do Título de Doutor em Sensoriamento Remoto. O trabalho precisa da incorporação das correções sugeridas pela Banca Examinadora e revisão final pelo(s) orientador(es).

Título: "DEM-BASED MORPHOTECTONIC ANALYSIS OF A PASSIVE CONTINENTAL MARGIN OF SOUTH AMERICA: NORTHERN PARAÍBA BASIN, NE BRAZIL"

O trabalho precisa da incorporação das correções sugeridas pela Banca Examinadora e revisão final pelo(s) Orientador(es)

Observações da Banca: As correções serão implementadas segundo critério de relevância dos orientadores.

Eu, Evlyn Marcia Leao De Moraes Novo, como Presidente da Banca Examinadora, assino esta ATA em nome de todos os membros.

Membros da Banca

Dra. Evlyn Marcia Leao De Moraes Novo - Presidente INPE/DSR

Dr. Márcio de Morisson Valeriano - Orientador INPE/DSR

Dra. Dilce de Fátima Rossetti - Orientadora INPE/DSR

Dr. Francisco Hilario Rego Bezerra - Convidado UFRN

Dr. David Lino Vasconcelos - Convidado UFCG

Documento assinado eletronicamente por **Evlyn Marcia Leão de Moraes Novo**, **Pesquisador**, em 31/01/2021, às 07:14 (horário oficial de Brasília), com fundamento no art. 6º, § 1º, do Decreto nº 8.539, de 8 de outubro de 2015.

A autenticidade deste documento pode ser conferida no site http://sei.mctic.gov.br/verifica.html, informando o código verificador **6446636** e o código CRC **0EC328EE**.

Referência: Processo nº 01340.000680/2021-14 SEI nº 6446636

"Afinal, o que é um cientista? É um homem curioso olhando por um buraco de fechadura, o buraco de fechadura da natureza, tentando saber o que está acontecendo".

JACQUES-YVES COUSTEAU

A meus pais ***Daize Razza*** *e* ***Eugênio Alves*** *(in memoriam), e ao meu avô* ***Pedro Alves*** *(in memoriam)*

ACKNOWLEDGEMENTS

Aos orientadores Márcio M. Valeriano e Dilce F. Rossetti pela orientação, suporte, compromisso, confiança e incentivo para seguir com a desafiante carreira científica.

Aos orientadores britânicos, Martin Stokes e Sarah Boulton, por todo apoio, suporte e conhecimentos transmitidos. Ao *School of Geography, Earth and Environmental Sciences* da *University of Plymouth* pela instalação e infraestrutura cedida durante o período de intercâmbio científico na Inglaterra.

Ao programa de pós-graduação em Sensoriamento Remoto do INPE, corpo docente e funcionários por toda ajuda, acesso às instalações do instituto, e pelo substancial aprendizado durante o doutorado.

O presente trabalho foi realizado com apoio da Coordenação de Aperfeiçoamento de Pessoal de Nível Superior - Brasil (CAPES) - Código de Financiamento 001, com bolsa no país e exterior (programa PrInt/CAPES), fundamental para o desenvolvimento desta pesquisa.

Ao Clódis O. Andrades Filho, Édipo Cremon e Lino Augusto pela amizade e valiosas discussões científicas.

Aos companheiros de sala do ASA, João Bosco, Matheus e Pétala pela amizade e momentos de descontração durante os cafés. Aos demais amigos do Sensoriamento Remoto, Victor, Caio, Wesley, Daniel, Rogério, Denis, Arian e Lucas. Aos amigos externos pelas resenhas durante as partidas intensas de futebol no INPE. Aos companheiros de sala no exterior, Wycliff, Jesse, Joshua, Symeon, Luis e killian por todo suporte, discussões científicas, e momentos de alegria compartilhados em *Plymouth*. Aos *housemates* de *Exeter*, David, Sally, Owen, Nathan e Saj pela amizade e por me proporcionarem uma experiência maravilhosa no SW da Inglaterra, mesmo durante os momentos difíceis enfrentados com o início da pandemia. Os amigos brasileiros de *Exeter* são também lembrados aqui pelas várias experiências compartilhadas.

A todos os ex e atuais moradores/moradoras da república "Cabaré da Leila" pelos diversos momentos de alegria.

A meus pais, irmão e à Maria Aparecida do Prado Asensão e família, pela confiança, carinho e suporte.

A minha namorada Luciana, por todo suporte, carinho e companheirismo.

ABSTRACT

The evolution of the relief in several areas of northeastern Brazil has been increasingly related to tectonics. This is the case of the central and southern sectors of the Paraíba Basin, where basin inversion has been suggested by an abundance of faults and folds in Miocene and late Pleistocene deposits displaying domic relief. A previous geomorphological investigation revealed a similar relief in Quaternary deposits to the north in this basin. However, rock exposures in this sector are scarce, making it difficult to carry out a detailed geological investigation to verify whether the domic relief was also due to basin inversion. This work aimed to investigate if qualitative and quantitative analyses of digital elevation model (DEM) data can explain if the dome at the northern sector of the Paraíba Basin is related to the tectonic inversion in the Late Quaternary. This development used the 1 arc-second DEM of the Shuttle Radar Topography Mission (SRTM) as data source for different applications. The morphological analysis of the domic reliefs was based on drainage networks, swath topographic profiles and geomorphic indices, analysis of drainage divides, as well as detection and study of knickpoints. A methodology for geological discrimination of sedimentary units was developed through geomorphometric regionalization and revealed that the slope, elevation, hypsometric integral, topographic coherence, and valley depth were the most suitable variables to discriminate Miocene from Quaternary units. This method resulted satisfactory overall (80.6 %) and by class accuracies (Post-Barreiras terrain: producer's accuracies = 83% and user's accuracies = 90.7 %). The morphological analysis of the domic reliefs revealed radial to recurved trellis patterns; tilted and asymmetric sub-basins; and anomalous river profiles. The analysis of drainage divide indicated some mobile segments with direction towards a high-elevation, chevron-shaped plateau related to lithological control by differences in bedrock erodibility. Although this was the cause of some knickpoints detected in the study area, river profiles with slope-break knickpoints, and steep channels with high incision and elevation values recorded mostly on homogeneous lithology were more likely related to tectonics. Statistical analysis suggested that the lowest knickpoints in each river were formed during a single tectonic event not older than the Miocene. The geomorphometric evidence of tectonic control, added to the domic relief, suggested that the northern Paraíba Basin might have also been affected by the basin inversion that produced the folding of correlated strata in the central and southern sectors of the Paraíba Basin. This event is correlated with the Andean Quechuan tectonic phase. Therefore, the most likely is that a pulse of rock upwarping could have triggered the lowering of river base levels and the propagation of knickpoints upstream river profiles, probably due to intraplate compression by the combined pushes of the Mid-Atlantic Ridge (towards the W) and the Andes (towards the E), as suggested for other areas in NE Brazil. These results corroborate the proposal that the passive margin of the South American plate remained under tectonic stress long after the main rifting in the late Jurassic-early Cretaceous.

Keywords: Dome. Tectonic uplifiting. Intraplate compression. Far-field stress. Late Pleistocene. Remote Sensing.

ANÁLISE MORFOTECTÔNICA BASEADA EM MDE DE UMA MARGEM CONTINENTAL PASSIVA DA AMÉRICA DO SUL: NORTE DA BACIA PARAÍBA, NE DO BRASIL

RESUMO

A evolução do relevo de várias áreas do nordeste do Brasil tem sido frequentemente relacionada à tectônica. Esse é o caso dos setores central e sul da Bacia Paraíba, onde uma abundância de falhas e dobras em depósitos miocênicos e pleistocênicos tardios que exibem relevo dômico sugerem a inversão de bacia. Uma investigação geomorfológica prévia revelou um relevo similar em depósitos quaternários para o norte desta bacia. Porém, exposições rochosas neste setor são escassas, tornando difícil conduzir uma investigação geológica de detalhe para verificar se o relevo dômico foi também relacionado à inversão de bacia. Esse trabalho teve como objetivo investigar se análises qualitativas e quantitativas de dados de modelo digital de elevação (MDE) podem explicar se o domo no norte da Bacia Paraíba está relacionado à inversão tectônica no Quaternário tardio. Esse desenvolvimento baseou-se no MDE de 1 arco-segundo da missão de topografia de radar orbital (SRTM) como fonte de dados para diferentes aplicações. A análise morfológica dos relevos dômicos baseou-se nas redes de drenagem, perfis topográficos em faixa e índices geomórficos, análise de divisores de drenagem, bem como detecção e estudo de *knickpoints*. Uma metodologia para discriminação geológica de unidades sedimentares foi desenvolvida através da regionalização geomorfométrica e revelou que a declividade, elevação, integral hipsométrica, coherência topográfica e profundidade de vale foram as variáveis mais adequadas para separar as unidades miocênicas das quaternárias. Esse método resultou em exatidão geral (80,6%) e por classe (terreno Pós-Barreiras: exatidão do produtor = 83% e exatidão do usuário = 90,7%) satisfatórias. A análise morfológica dos relevos dômicos revelou padrões treliça recurvada à radial; sub-bacias assimétricas e basculadas; e perfis longitudinais anômalos. A análise do divisor de drenagem indicou alguns segmentos móveis com direção para um plateau elevado com forma em V relacionados à controle litológico por diferenças de erodibilidade do leito. Embora essa foi a causa de alguns *knickpoints* detectados na área de estudo, perfis longitudinais com *knickpoints slope-break* e canais inclinados com valores de incisão e elevação altos registrados principalmente sobre litologias homogêneas foram provavelmente relacionados a tectônica. Análises estatísticas sugeriram que os *knickpoints* mais baixos em cada perfil foram formados por um único evento tectônico, de idade pelo menos do Mioceno. A evidência geomorfométrica de controle tectônico, aliado ao relevo dômico, sugeriu que a borda norte da Bacia Paraíba pode ter sido também afetada por inversão de bacia que produziu o dobramento de estratos correlatos nos setores central e sul da Bacia Paraíba. Esse evento está correlacionado com a fase tectônica Andina Quechua. Portanto, o mais provável é que um pulso de soerguimento poderia ter levado ao rebaixamento do nível de base dos rios e a propagação de *knickpoints* a montante dos perfis longitudinais, possivelmente devido à compressão intraplaca pelos empurrões combinados da dorsal mesoatlântica (em direção W) e Andes (em direção E), como sugerido para outras áreas do NE do Brasil. Esses resultados corroboram a proposta de que a margem passiva da placa Sul-Americana

permaneceu sobre esforços tectônicos muito tempo depois do rifteamento principal no Juro-Cretáceo inferior.

Palavras-chave: Domo. Soerguimento tectônico. Compressão intraplaca. Campo de tensão distal. Pleistoceno tardio. Sensoriamento Remoto.

LIST OF FIGURES

Page

LIST OF TABLES

Page

CONTENTS

1 INTRODUCTION

Neotectonic studies of many reliefs on Earth have generally included morphotectonic investigation based on the analysis of drainage networks (HOWARD, 1967; DEFFONTAINES; CHOROWICZ, 1991), geomorphic indices (KELLER; PINTER, 1996) and knickpoint modelling (KIRBY; WHIPPLE, 2012). The development of new methods for assessing the stability/mobility of drainage divide and divide motion is important for discriminating how much relief responds to rock erodibility or a tectonic control (WILLETT et al., 2014; FORTE; WHIPPLE, 2018). The geomorphometric analysis has the advantage of allowing recognize the tectonic signature of extensive areas with difficult access and scarcity of outcrops. However, the efficiency of many geomorphic indices for recognizing tectonically-controlled landforms varies from method to method and from area to area, resulting in inconclusive interpretations. Therefore, approaching geomorphic indices based on a multiscale analysis (i.e., rivers, river profiles, and drainage basins) integrated with geological data has been recommended (El HAMDOUNI et al., 2008; MAHMOOD; GLOAGUEN, 2012; ANDREANI et al., 2014; SCOTTI et al., 2014; OWONO et al., 2016).

The advance of digital data processing techniques and the manipulation of digital topographic data from remote sensing have facilitated the morphotectonic analysis. This task has been favoured by semi-automatic algorithms and computer programming languages applied to topographic data from digital elevation models (DEMs) (SHAHZAD; GLOAGUEN, 2011; SCHWANGHART; SCHERLER, 2014; GALLEN; WEGMANN, 2017; PÉREZ-PEÑA et al., 2017; FORTE; WHIPPLE, 2019), such as the interferometric synthetic aperture radar (InSAR) C-band of the Shuttle Radar Topography Mission (SRTM)(RABUS et al., 2003). However, the efficiency of these methods remains to be tested in diverse geological and tectonic settings.

There are a few applications of geomorphic indices to detect tectonic activity on relatively stable areas of passive continental margins (KALE; SHEJWALKAR, 2008; GALLEN et al., 2013; ALVES; ROSSETTI, 2017). This is generally due to: the poor surface expression of faults or fault scarps, a situation particularly important in humid tropical regions, where faults can be buried by thick soil horizons (MARLIYANI et al., 2016); and the lower fault slip rates and lower magnitude earthquakes than active margins (BEZERRA; VITA-FINZI, 2000). As a result, landscape evolution in many passive margins has often been attributed to climate, such as in northeastern Brazil (KING, 1956; KING, 1967; MABESOONE; CASTRO, 1976). In addition, some geomorphological models (e.g., downwarp, scarp retreat and pinned divide of an elevated

rifted margin) (GALLAGHER et al., 1998) were based on the common assumption that continental passive margins have no significant post-rift deposition, arguably due to the topographically elevated location since the main rifting, which did not favour deposition (JAPSEN et al., 2012b). The overall lack of interest in investigating the post-rift sections of passive margins led to the misconception that they are stable areas (BEZERRA et al., 2008). An increased number of publications in several passive margins worldwide, however, have shown that they experienced several episodes of uplift and subsidence long after rifting (JAPSEN et al., 2006; JAPSEN et al., 2012a; JAPSEN et al., 2012b).

There have been increased publications evidencing that Neogene and Quaternary tectonic reactivations played a key role in shaping the relief of areas of the northeastern South American passive plate (NOGUEIRA et al., 2010; GURGEL et al., 2013; BEZERRA et al., 2014). This is particularly the case of the Paraíba Basin because of its late disconnection from the African plate (SUGUIO; MARTIN, 1996). Evidence of tectonic deformation in the Paraíba Basin is available for its central and southern sectors (BEZERRA et al., 2001; BRITO-NEVES et al., 2004; BEZERRA et al., 2008; BRITO-NEVES et al., 2009; ROSSETTI et al., 2011a; ROSSETTI et al., 2011b; BEZERRA et al., 2014; GANDINI et al., 2014; ANDRADES-FILHO; ROSSETTI, 2015; LIMA et al., 2017), while the northern sector was less studied, chiefly due to the scarcity of outcrops.

Dome-like reliefs typify the north of Paraíba Basin, where Quaternary deposits have been displaced to a higher position relative to adjacent areas of Precambrian basement rocks. The positive morphology of Quaternary deposits led to suggest a geologically recent tectonic deformation due to basin inversion (ALVES et al., 2017), as also recorded in other sedimentary basins of northeastern Brazil (MAIA; BEZERRA, 2014; MARQUES et al., 2014; NOGUEIRA et al., 2015; VASCONCELOS et al., 2019b; BEZERRA et al., 2020). However, geomorphological and geological studies are still needed to better characterize the dome-like reliefs of the north of Paraíba Basin and reconstruct deformation dynamics during the late stages of evolution of the South American passive margin. In addition, folds are still incompletely characterized in the Paraíba Basin to allow a broader understanding of the relationship between extension and compression that have affected this passive margin sector.

DEM-based geomorphometric analyses provide key data for geomorphological and thus geological mapping by providing qualitative and quantitative information of terrain, from simple and local data to regional characterization and classification. It is expected that DEM-based techniques have the potential to contribute in investi-

gations aiming to determine the origin of the domic relief verified in the northern sector of Paraíba Basin, thus contributing to analyze its possible link with the neotectonic history of the South American passive margin. This work is presumed to answer if the domic morphologies of the northern Paraíba Basin are due to a tectonic inversion in the Quaternary, and if the river profile analyses of DEM allow to verify changes in the drainage network indicative of tectonic uplifting.

Despite the recent availability of broad coverage and high resolution DEM and processing techniques, the development of specific applications remains necessary to effectively contribute to the refinement of pre-existing geological information. The central aim of this work was to apply a morphotectonic approach based on SRTM-DEM data to analyze if the sector of South America passive continental margin located in the Paraíba Basin, northeastern Brazil, was tectonically inverted in the Late Quaternary. Specific aims included:

a) To assess the relationship between domic reliefs and underlying lithology based on the qualitative morphological analysis of the drainage network;

b) To carry out a quantitative analysis of geomorphic indices derived from SRTM-DEM data to investigate the genesis of domic reliefs;

c) To analyze how knickpoints extracted from river profiles, normalized steepness index (k_{sn}) and drainage divides are related to lithology and/or tectonics;

d) To analyze the spatial patterns and behaviours of knickpoints;

e) To establish a methodology based on the regionalization of geomorphometric variables for the geological discrimination of Miocene and Quaternary sedimentary units in the northern Paraíba Basin.

2 THEORETICAL BACKGROUND

2.1 Tectonics, neotectonics and scales of investigation

Tectonics is a key factor which can create topography and maintain the relief. The identification of reliefs originated by tectonics requires refined and systematic studies, including qualitative and quantitative geomorphological analyses.

Neotectonics refers to the reactivation of pre-existing tectonic structures and the formation of new ones in the last 23 million years (i.e., from Neogene) (OBRUCHEV, 1948). The increased record of Neogene tectonic structures in the Brazilian territory evidences the decisive role of neotectonics in the shaping of the modern landscape in several regions, including the Northeastern (SAADI et al., 2005).

Studies aiming to investigate the role of tectonic processes on the reliefs vary from direct investigation of in situ geological data to indirect investigation based on remote sensing data (FOSSEN, 2010). However, field data collection may be problematic in large areas of difficult access and scarce outcrops. In addition, many of the features of interest are of dimensions that require identification on more general scales than direct observations. The use of remote sensing data is a viable alternative for the first case and mandatory for the second. In particular, qualitative and quantitative morphotectonic analysis based on the drainage network (HOWARD, 1967; DEFFONTAINES; CHOROWICZ, 1991), morphostructural lineaments (O'LEARY et al., 1976), and geomorphic indices (KELLER; PINTER, 1996), are the approaches most used in this type of investigation.

2.1.1 Tectonic structures and resulting reliefs

Basically, rock deformation occurs by compressional, tensional and/or shear stresses. Rocks under these stresses can bend (ductile deformation), fracture (brittle deformation), or exhibit both behaviors (FOSSEN, 2010). Brittle deformation generates fractured structures, such as joints and faults. Faults are grouped into three classes, according to the relative motion of the displaced blocks: normal, reverse and strike-slip (Figure 2.1a). Normal faults generated by tensional stress move vertically, with the hanging wall being lowered relative to the footwall. Reverse faults generated by compressional stress also move vertically, but with the hanging wall moving upward relative to the footwall. Strike-slip faults generated by shear stress move horizontally, being classified as dextral (right-lateral motion) or sinistral (left-lateral motion) in a plan view. Faults can occur at different scales, resulting in micro faults of a few cen-

timeters to regional faults of tens of kilometers. Ductile deformation generates folds, which are classified as: synclines, when they present concave shapes and younger rock layers towards the fold core; and anticlines, when they have convex shapes and younger rock layers further away from the fold core (FOSSEN, 2010) (Figure 2.1b).

Figure 2.1 - Type of tectonic structures and resulting reliefs.

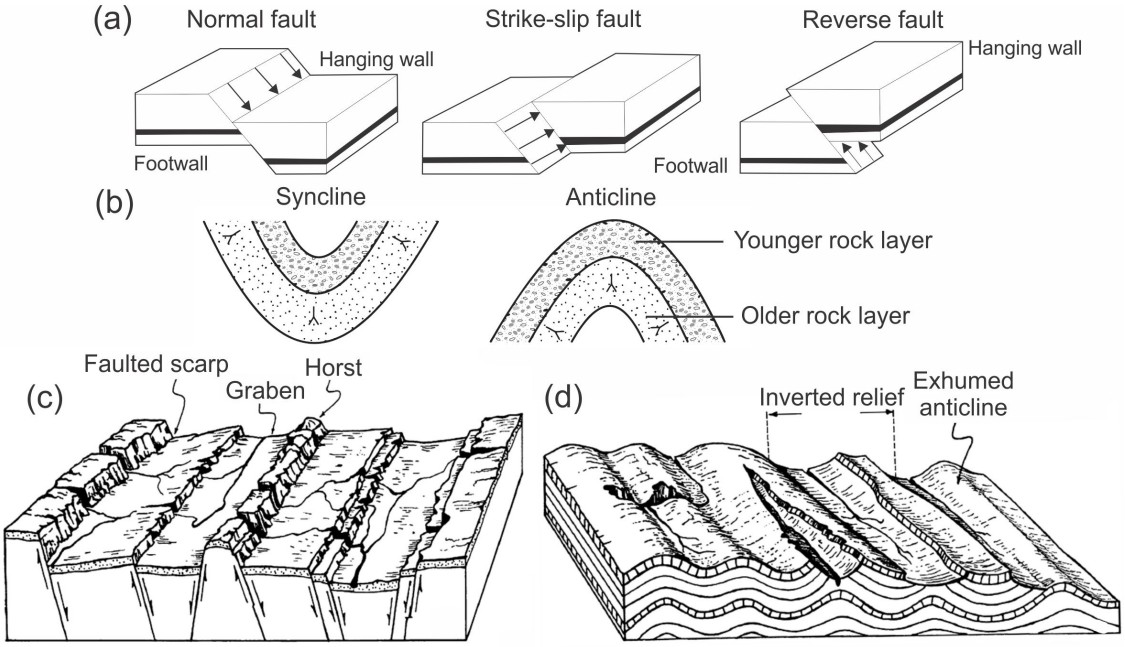

(a-b) Classes of faults (a) and folds (b). (c-d) Reliefs related with faults (c) and folds (d).

SOURCE: Adapted from Fossen (2010) and Suertegaray et al. (2003).

The topographic expression of faulted reliefs is generally marked by fault scarps in the classical geomorphological model (CASSETI, 1994). Fault block scale terrains are characterized by uplifted (horst) and subsided (graben) blocks (CASSETI, 1994; SUERTEGARAY et al., 2003) (Figure 2.1c). Folded reliefs occur as a succession of folds, which are generally marked by well-preserved relief shapes displaying anticline crests and syncline valleys (SUERTEGARAY et al., 2003) (Figure 2.1d).

The investigation of reliefs affected by tectonics in areas lacking outcrops has been performed by visual interpretation of some morphotectonic elements extracted from remote sensing data (e.g., optical images and DEMs), such as lineaments (O'LEARY et al., 1976), drainage patterns and drainage anomalies (HOWARD, 1967;

DEFFONTAINES; CHOROWICZ, 1991), as well as morphometric indices (KELLER; PINTER, 1996). The analysis of these elements has been mostly applied for the morphological characterization of faulted reliefs (MAHMOOD; GLOAGUEN, 2012; ANDREANI et al., 2014), while only a few studies have investigated the reliefs affected by folds, particularly those over sedimentary basins. For example, Das et al. (2010) carried out a morphological characterization of folded reliefs dominated by Late Tertiary sedimentary rocks in northeastern India and Bangladesh. The authors applied principal component analysis (PCA) and image fusion combining ETM+/Landsat-7 optical images and SRTM-DEM. They found a series of crests and valleys related to anticlines and synclines, as well as folds of various geometries.

2.1.2 Morphological analysis of drainage network

Drainage systems can provide important information about the tectonic influence on modern reliefs, given their sensitivity to environmental changes. Changes in drainage systems may vary both in space (e.g., at local and regional scales) and time. The visual interpretation of drainage patterns has been widely used in geomorphological studies focused on the identification of reliefs under tectonic effects (Figure 2.2 and Table 2.1). Howard (1967) and Deffontaines and Chorowicz (1991) are classic examples of geomorphological studies involving the description of drainage patterns.

Figure 2.2 - Basic (a) and modified drainage patterns (b).

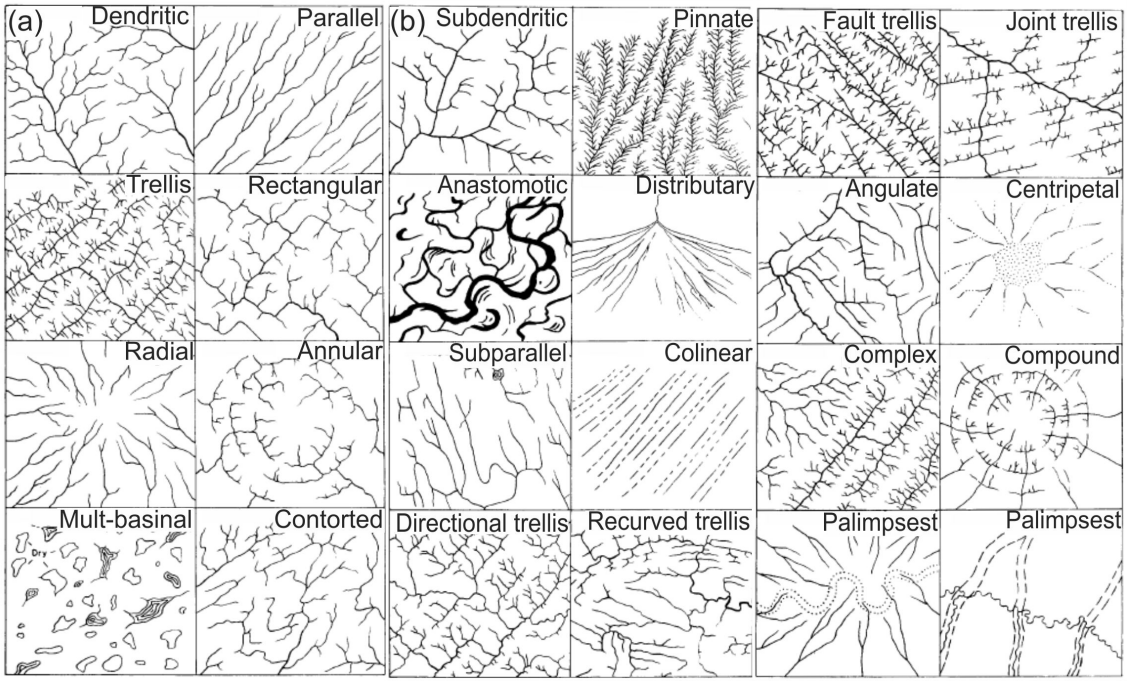

SOURCE: Adapted from Howard (1967).

The drainage pattern is represented by the arrangement of fluvial channels within a drainage system (HOWARD, 1967). The qualitative investigation of the drainage network is a simple and robust way to extract information about topography and lithology. It also allows the recognition of important elements to infer tectonic structures, such as faults and folds, when the lithological boundaries are absent. The dendritic, parallel, trellis, rectangular, radial, annular, multibasinal and contorted patterns (Figure 2.2a and Table 2.1) are examples of basic drainage patterns. The modified drainage patterns are variations from the basic patterns, as they retain part of characteristics of the former. Examples of modified drainage patterns are: subdendritic, pinnate, anastomotic, distributary, angulate, centripetal, subparallel, colinear, complex, compound and palimpsest patterns, and variations of trellis (Figure 2.2b and Table 2.1) (HOWARD, 1967).

Table 2.1 - Summary of some basic and modified drainage patterns with the corresponding geological significance.

Drainage pattern		General characteristics	Significance
Dendritic	Basic	- Irregular branching in all directions - Tree-like branching - Tributaries joining main streams at all angles	- Rocks which have suffered intense metamorphism - Significant structural control is lacking
Trellis		- Drainage pattern intermediate between dendritic and rectangular	- Folded or tilted strata of mature, dissected coastal plains - Dipping or folded sedimentary, volcanic, or low-grade metasedimentary rocks - Areas of parallel fractures
Radial		-Streams radiate from a central area	- Consequent drainage of domes, mountains (volcanoes, monadnocks, erosion residuals)
Sub-dendritic	Modified	- Tributaries extend horizontally - Fairly common variation of dendritic - Tributaries diverge from the trunk stream	- Slight structural or topographic control in homogeneous rocks
Directional trellis		-Dominant trellis directions controlled by structure or lithology-tributaries on one side longer than on the other	- Series of parallel faults or joints, planes of weakness
Fault trellis		- Branching, converging, diverging, roughly parallel faults	- Parallel faults, planes of weakness
Joint trellis		- Straight parallel faults and or joints	- Alternating grabens and horsts or a succession of parallel rifts
Recurved trellis		-Sweeping curves around folds	- Strong topographic and structural control - This pattern occurs around "fold's nose"

SOURCE: Adapted from Howard (1967) and Deffontaines and Chorowicz (1991).

2.2 Morphometry applied to the identification of tectonic reliefs

The quantitative approach through the morphometric analysis is of additional interest in studies focused on detecting the tectonic effect in the reliefs. This approach can be performed by applying swath profiles and indices. Regarding the indices, there is no common sense in their specification, and various terms have been applied, such as morphometric, geomorphic, geomorphological, morphotectonic and geomorphometric indices. The term geomorphic index was adopted throughout this thesis.

Geomorphic indices have been commonly used in morphotectonic analysis, especially to verify recent tectonic processes that act on relief (KELLER; PINTER, 1996), although other causes may also be involved (e.g., lithological control). Several indices were proposed in the classical geomorphological and geological literature in the last decades. However, most of them were developed for landscapes with environmental characteristics (e.g., climate) from the northern hemisphere, thus the need to adapt and test their potential for tropical regions persists. The analysis of these indices allows to infer relief sectors related to tectonic processes (MAHMOOD; GLOAGUEN, 2012). There is an increasing number of semi-automatic and less subjective algorithms for extracting geomorphic indices. DEM-based geomorphic indices can be extracted automatically as a result of the advance in computer programming languages and Geographic Information System (GIS) softwares (SHAHZAD; GLOAGUEN, 2011; SCHWANGHART; SCHERLER, 2014; GALLEN; WEGMANN, 2017; FORTE; WHIPPLE, 2019). However, some techniques to carry out this task remain to be tested considering a larger number of geological and tectonic settings. Swath profiles and examples of some geomorphic indices with high potential to recognize tectonic reliefs are described in the following sections. The analysis of knickpoints and divide stability are also presented here, given their potential to investigate reliefs controlled by lithology and/or tectonics.

2.2.1 Swath topographic profiles

Swath topographic profiles are useful geomorphological tools for performing numerical investigations to detect reliefs with tectonic control; see Telbisz et al. (2013) for a review. Swath profiles are created from the construction of lines parallel to the swath baseline to define transverse limits for data sampling and are operated with two parameters: sampling width and step-size. This kind of profile allows to extract detailed statistical information that combines elevation (e.g., mean, maximum and minimum values) and geomorphometric variables, such as relative relief (range of

elevation values).

Swath profiles can be characterized by hypsometric curves, which represent the distribution of the relative elevation and the area of a given drainage basin (KELLER; PINTER, 1996). The shape of the hypsometric curves determines the hypsometric integral, which corresponds to the area below the curve. The relationship between hypsometric integral and erosion cycle allows its use as an indicator of the relief evolution stage (STRAHLER, 1952; KELLER; PINTER, 1996). An approximation of the hypsometric integral calculation (STRAHLER, 1952) is obtained by the elevation-relief ratio - E (PIKE; WILSON, 1971), as follows:

$$E = (hmean - hmin)/(hmax - hmin) \tag{2.1}$$

where, $hmean$, $hmin$, and $hmax$ correspond to mean, minimum and maximum elevations. E values near 0 are related to mature reliefs with a high degree of dissection, whereas E values close to 1 are associated with less dissected, young transient reliefs (KELLER; PINTER, 1996). The latter condition has been commonly interpreted as an indicator of a relief affected by tectonic uplifting, where rivers are entrenched (El HAMDOUNI et al., 2008; MAHMOOD; GLOAGUEN, 2012; ANDREANI et al., 2014; SCOTTI et al., 2014). However, the direct calculation of E in the swath topographic profiles may produce some artifacts. For example, in flat areas with closely-spaced elevation curves (maximum, minimum, and mean), subtle variations in the mean elevation can produce large differences in E values (PÉREZ-PEÑA et al., 2017). The enhanced transverse hypsometry index ($THi*$) was proposed to avoid these artifacts (PÉREZ-PEÑA et al., 2017). The E values in the $THi*$ index are weighted for the local relative relief by adjusting a logarithmic normalization function, which results in higher weights in areas of low relative relief. E values are also re-scaled from the 0.2 to 0.8 interval to improve the comparison of hypsometry in the swath profiles, considering that values under and above these thresholds are generally rare in most reliefs on Earth (PÉREZ-PEÑA et al., 2009).

2.2.2 Drainage basin asymmetry

The analysis of basin asymmetry consists in the measurement of the transverse tilting, perpendicular to the main direction of the trunk stream on the scale of drainage basins (El HAMDOUNI et al., 2008; SCOTTI et al., 2014; OWONO et al., 2016), and can be estimated by the asymmetry factor - AF index (HARE; GARDNER, 1985) (Figure 2.3).

Figure 2.3 - Diagram illustrating the response of the drainage basin to the tectonic tilting.

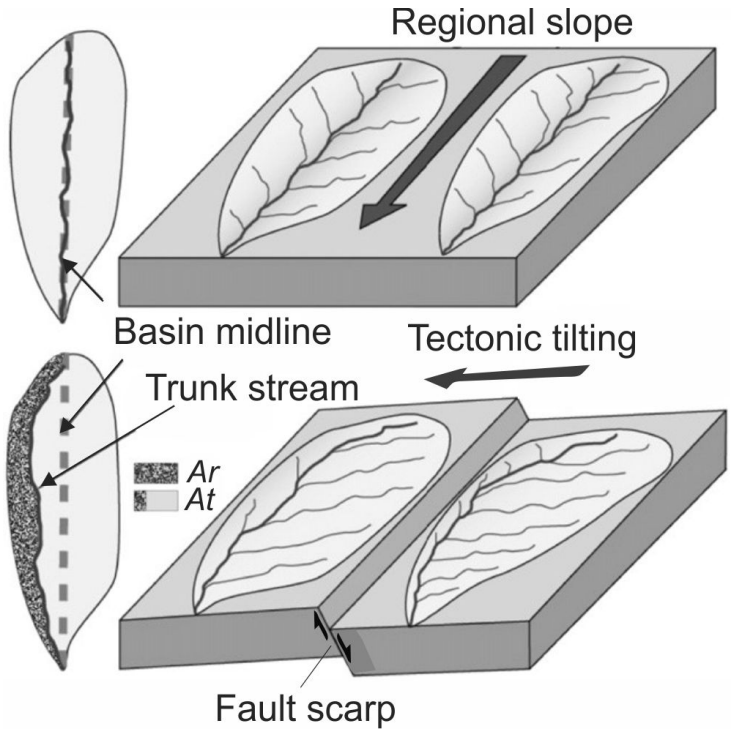

SOURCE: Adapted from Keller and Pinter (1996) and Mahmood and Gloaguen (2012).

The AF index is defined as:

$$AF = Ar/At \times 100 \tag{2.2}$$

where, Ar is the area of the right margin of the drainage basin (i.e., facing downstream); and At is the total area of the drainage basin. AF values significantly higher or lower than 50 may suggest transverse tilting, considering areas of homogeneous lithologies (HARE; GARDNER, 1985). Drainage basins with AF values close to 50 are symmetrical, as they have little or no tectonic influence (HARE; GARDNER, 1985).

2.2.3 River profile analysis

2.2.3.1 Normalized river long profiles

A long profile is a useful representation that shows the variation of the channel gradient of a river along its entire length (CHRISTOFOLETTI, 1981). Rivers in equilibrium

(graded river) display typical concave or semi-logarithmic longitudinal profiles and higher gradient upstream than downstream, which generally indicate mature and steady-state landscapes (MACKIN, 1948). Changes in the concavity of the equilibrium profiles can be used as indicators of lithological variation and/or tectonic uplifting (DEMOULIN, 1998; WHIPPLE; TUCKER, 1999). The long profiles of normalized rivers (DEMOULIN, 1998) provide relevant information on the degree of grading of profiles in rivers with different lengths and gradients, based on the concavity (E_r), maximum concavity (H_{max}) and position concerning the river source (E_q; Figure 2.4). E_r is defined as the percentage area of a triangle formed between the river long profile and an assumed original profile that connects the headwater to the mouth by a straight line (DEMOULIN, 1998). Whereas H_{max} is redundant to concavity, its normalized distance to the river source E_q is an additional indicator of the degree of grading of long profiles. Low E_q values represent rivers with graded profiles (DEMOULIN, 1998).

Figure 2.4 - Diagram illustrating the extracted parameters for a hypothetical river long profile.

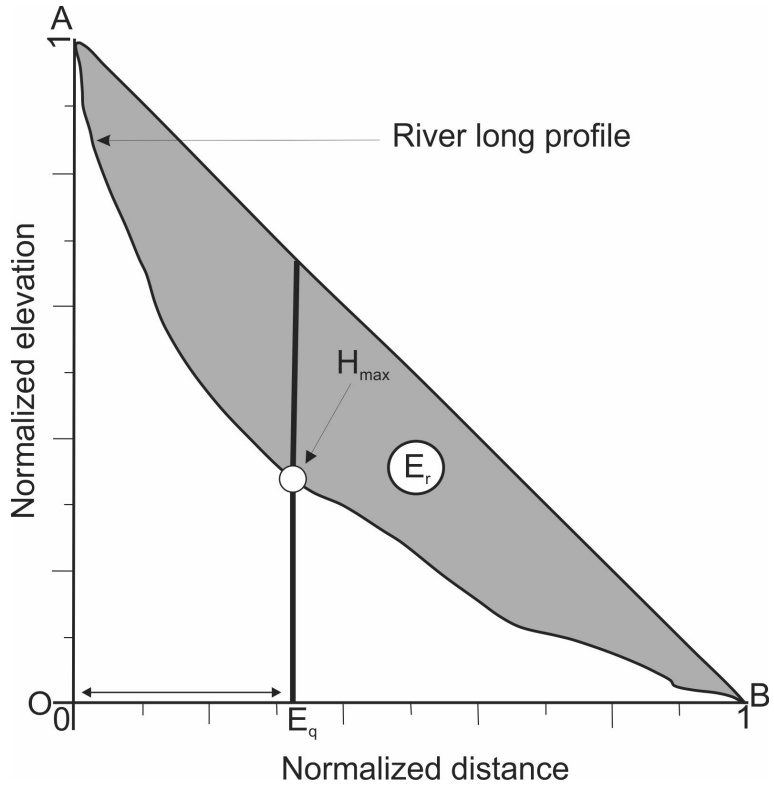

A = river source; B = river outlet; E_r = percentage area of the triangle OAB; H_{max} is expressed relative to OA; E_q is expressed relative to OB.

SOURCE: Adapted from Demoulin (1998).

2.2.3.2 Normalized channel steepness index - k_{sn}

The analysis of river profiles based on river incision models in erosional reliefs has had notable progress in recent years (KIRBY; WHIPPLE, 2012), especially in tectonically active mountainous terrains (SNYDER et al., 2000; WOBUS et al., 2006; KIRBY; WHIPPLE, 2012; ANDREANI; GLOAGUEN, 2016; GALLEN; WEGMANN, 2017). This type of analysis has allowed inferences about climate, lithology, as well as spatial and temporal changes of uplifting (WOBUS et al., 2006). The stream power family of river incision models has been commonly used to investigate river profiles worldwide, despite some limitations in capturing important aspects of channel dynamics (LAGUE, 2014). The generalized equation of the stream power model (HOWARD et al., 1994; SNYDER et al., 2000) based on the principle of mass conservation is written as follows:

$$\frac{dz}{dt} = U - E = U - KA^m S^n \tag{2.3}$$

where, dz/dt is the rate of change of river bed elevation; U is the rock uplift rate; E is the long-term erosion rate; A is the upstream drainage area, S is the channel slope, K is the erodibility coefficient; and m and n are empirical constants. In steady-state reliefs, where $dz/dt = 0$ (i.e., uplift equals erosion), equation 2.3 can be rewritten as:

$$S = \left(\frac{U}{K}\right)^{1/n} A^{-m/n} \tag{2.4}$$

The terms of equation 2.4 can be described by an empirical power law relationship (HACK, 1957; HACK, 1973) between channel slope and upstream drainage area:

$$S = k_s A^{-\Theta} \tag{2.5}$$

$$\theta = m/n \tag{2.6}$$

$$K_s = \left(\frac{U}{K}\right)^{1/n} \tag{2.7}$$

where k_s is referred as the channel steepness index ($m^{2\theta}$); and θ as the channel concavity index (dimensionless) (SNYDER et al., 2000). The term "concavity index" is used here to refer to the exponent in equation 2.5, which distinguishes it from the concavity of the normalized river profiles (DEMOULIN, 1998). Spatial variability in k_s values may reflect spatial or temporal variations in uplifting rates in reliefs with homogeneous lithological and climatic conditions (WOBUS et al., 2006; WHIPPLE et al., 2013). To compare k_s values from river profiles with different sizes, the normalized channel steepness index k_{sn} is obtained based on a fixed reference θ (θref) (WOBUS et al., 2006). Given the sensitivity of θ values to noises in the DEMs, a careful selection of a θ value is recommended for an adequate investigation of the channel steepness (MUDD et al., 2018). In general, empirical studies have shown that θ varies between 0.4–0.6, but a fixed reference concavity of 0.45 is frequently used for characterizing steady-state channels in several reliefs (SNYDER et al., 2000; WOBUS et al., 2006; KIRBY; WHIPPLE, 2012).

The parameters S and A can be extracted directly from DEMs, while the k_{sn} and θ have been extracted from the linear regression between S and A on a log-log graph. However, the channel slope may enhance significant scatter with the direct influence on the k_s calculation, since the topographic data have noisy variations (microrrelief, artifacts and errors), which are propagated to the slope (1st order derivative of elevation). The transformation of river profiles to chi plots (χ or integral method) (PERRON; ROYDEN, 2013) has been proposed to reduce the noise of topographic data and extract more reliable k_s values. Basically, this method integrates both sides of the equation 2.5 and uses drainage area (A_0) as reference for a more convenient unit (PERRON; ROYDEN, 2013). The chi plots (χ-elevation space) are represented as an independent variable (x axis) by the integral of the drainage area and the elevation as a dependent variable (y axis), while the channel steepness is related to the local slope of a transformed profile.

2.2.3.3 Type of knickpoint

The convex-upward discontinuities (knickpoints) in river profiles have been used as an indicative of rivers with a transient response due to perturbations related to local base level changes. These are caused by tectonics (e.g., increase in uplifting and fault slip rates), sea level oscillation and/or climatic variations, which can enhance or reduce the efficiency of river incision (WHITTAKER et al., 2008; KIRBY; WHIPPLE, 2012; WHIPPLE et al., 2013). As a result, a transient signal in the form of knickpoint is propagated upstream through the channel network over time, as a kine-

matic wave of incision (TUCKER; WHIPPLE, 2002; WHIPPLE; TUCKER, 2002) (Figure 2.5a). Knickpoints are classified into two end-member morphologies, i.e., vertical-step or slope-break, depending on the nature of the perturbation and mechanisms of river incision (HAVIV et al., 2010; WHIPPLE et al., 2013) (Figure 2.5b-e). Vertical-step knickpoints may be generated by a discrete event (e.g., a locally resistant substrate, debris flow or landslide) and can be recognized as a spike in slope values (WHIPPLE et al., 2013) (Figure 2.5b-c). They are generally anchored in space and have no direct tectonic significance (KIRBY; WHIPPLE, 2012). Slope-break knickpoints, generated by persistent changes (i.e., spatial or temporal) in boundary conditions, are recognized as breaks in log-log slope-area graphs, followed by an increase in k_s in the downstream segment (KIRBY; WHIPPLE, 2012; BOULTON et al., 2014)(Figure 2.5d-e). This type of knickpoint, key to the interpretation of tectonics in erosional reliefs (WOBUS et al., 2006; KIRBY; WHIPPLE, 2012), defines two mobile boundaries in the river profile: a downstream sector related with the region that adjusts to the new perturbation; and an upstream sector, which holds characteristics from the residual relief (WHIPPLE et al., 2013).

Figure 2.5 - Propagation of knickpoints through time in a hypothetical basin and type of knickpoints.

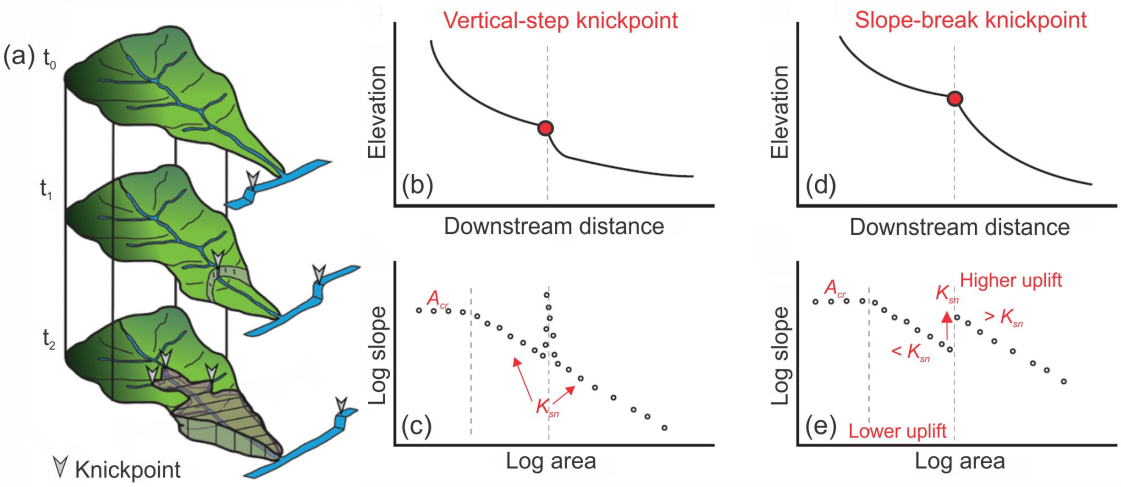

(a) Diagram illustrating a drainage basin with base level lowering and propagation of knickpoints as a kinematic wave through time (t_0-t_2). (b) Knickpoint end-member morphologies (vertical-step and slope-break) and their representation in distance-elevation (b-d) and log-log slope-area graphs (c-e). A_{cr} = critical threshold drainage area.

SOURCE: Diagrams modified from Gallen et al. (2013) and Kirby and Whipple (2012).

Theoretically, mobile knickpoints propagate upstream at constant vertical rates, so they should occur at similar elevations and follow contour lines (NIEMANN et al., 2001; WOBUS et al., 2006). However, it is important to note that several factors can affect and disperse the knickpoint heights during the knickpoint migration (e.g., spatial variations in uplift rates and absence of a pre-existing steady-state) (BOULTON et al., 2014). In contrast, studies have shown that the horizontal celerity of a knickpoint is primarily a function of the drainage area (CROSBY; WHIPPLE, 2006). Hence, the largest the drainage area, the highest the velocity of the knickpoint migration upstream river profile.

2.2.4 Divide stability analysis

In addition to river profiles, the divide stability analysis is of additional interest to investigate the dynamic reorganization of drainage networks and basins (WILLETT et al., 2014). Many routine topographic analyses assume that the topology of the drainage network and the geometry of river basins are static. However, recent publications using geomorphological evidence (e.g., river capture) have demonstrated that drainage divides are more mobile than thought (WILLETT et al., 2014; WHIPPLE et al., 2017; FORTE; WHIPPLE, 2018).

Maps of the drainage network coloured by χ (χ-maps) have the potential to investigate the mobility of drainage divides. This is because significant variations in χ on opposite sides of drainage divides (χ-anomalies) may suggest a divide migration (e.g., due to a river capture), which is driven by differences in erosion rates of river channels (Figure 2.6a) (WILLETT et al., 2014). In this case, the divide is suggested to move from the lower (aggressor side) to the higher (victim side) χ values at the divide boundaries. Some recent studies have interpreted active divide migration due to differences in bedrock erodibility or tectonics (YANG et al., 2015; STRONG et al., 2019; ZONDERVAN et al., 2020). However, the straightforward interpretation of χ may produce anomalies, and difficult the interpretation of mobile divides in transient reliefs (WILLETT et al., 2014; WHIPPLE et al., 2017). On the other hand, divide instability has been suggested to be more reliable by interpreting across-divide differences in some topographic metrics (Gilbert metrics), as they are topographic proxies for erosion rates. Gilbert metrics include the elevation at the channel head, upstream relative relief and upstream gradient (WHIPPLE et al., 2017; FORTE; WHIPPLE, 2018) (Figure 2.6b). Similarly to the χ, the divide is expected to move from lower to higher channel elevation values, while for gradient and relative relief values, the divide is expected to move to the side with lower values at the channel heads (Figure 2.6b).

Figure 2.6 - Diagram of the Gilbert metrics for the analysis of drainage divide stability.

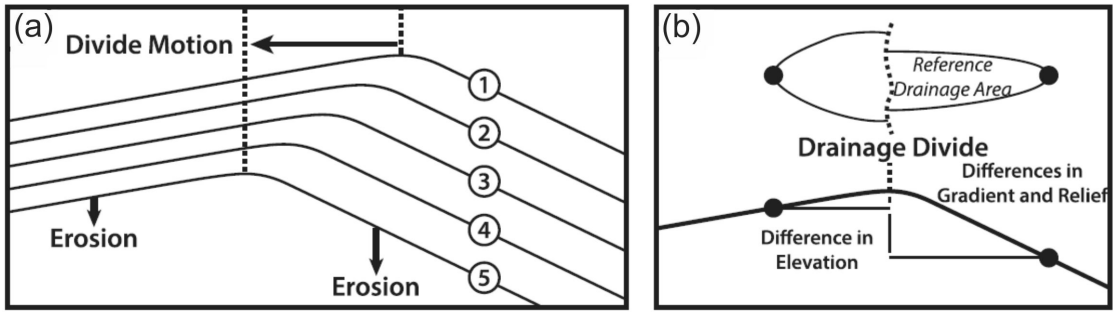

(a) Drainage divide is suggested to move toward the side of the divide with lower erosion rates, where channels have low gradients. (b) Based on the Gilbert metrics, the drainage divide is expected to move towards the side of the divide with higher headwater channel elevations, as well as lower gradient and relative relief values.

SOURCE: Diagram simplified from Forte and Whipple (2018).

2.3 Geological discrimination by remote sensing

For a long time, geological discrimination techniques were based on the analysis of key-elements of image interpretation (e.g., tone, colour, texture, shape, pattern, location, and association) from aerial photographs (SOARES; FIORI, 1976). One of the best-known initiatives for collecting data on natural resources in Brazil, including geological information, was the RADAMBRASIL project (ALLEVATO; PINGARILHO, 1979). This project was developed based on aerial images derived from an X-band real aperture radar (RAR) system to generate cartographic products for the entire Brazilian territory at the 1:1000000 scale.

In the last decades, the advancement of space technology with the new generation of sensors with different spectral bands has allowed the development of studies from low to high spatial resolutions in different areas of knowledge. Orbital remote sensing data provide a synoptic view of the Earth's surface, with the discrimination of large continental areas. In general, geological discrimination by optical remote sensing (hyperspectral and multispectral images) focuses on relatively medium to small areas, from 100 to 10000 km² (Figure 2.7). However, in areas with frequent cloud and dense vegetation cover, such as in tropical regions, the use of optical imagery constitutes a barrier to the direct observation of geological features, as it records only the information on the target's surface. In contrast, synthetic aperture radar (SAR)

systems that operate in the microwave region allow data acquisition independently of weather conditions and solar source. Additionally, longer microwave wavelengths (e.g., L and P bands) penetrates in dense vegetation, allowing the observation of canopy and terrain characteristics (HENDERSON; LEWIS, 1998). Similarly to optical images, SAR images can be used to discriminate medium to small geological areas (Figure 2.7). Both optical and radar data have been applied to the surface cover characterization or of cover elements, including planimetric analyses and plan morphology descriptors; in contrast to the extraction of topographic information, as required by some morphotectonic analyses, as described in the previous sections (2.1.2, 2.2.1, 2.2.2, 2.2.3, and 2.2.4). The 3D terrestrial and airborne light detection and ranging (LIDAR) are exceptions because they collect geographic point cloud data to generate DEMs and develop 3D analyses. Despite the higher potential of LIDAR data to develop studies with high spatial resolution, its use for geological discrimination is restricted due to its small aerial/terrestrial coverages (0.1 to 100 km², Figure 2.7).

Figure 2.7 - Scales of investigation, spatial resolution and type of remote sensing data.

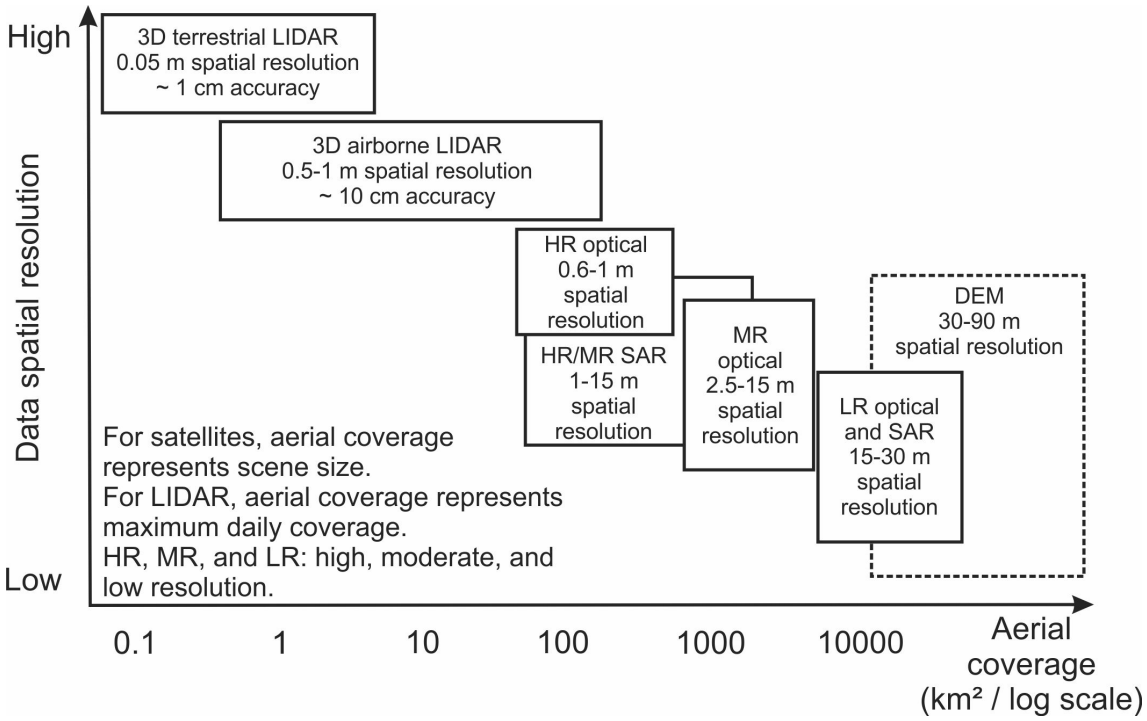

SOURCE: Adapted from Rathje and Adams (2008).

Alternatively, globally available DEMs, such as the free SRTM-DEM, have the potential to perform geological discrimination from medium to large areas (e.g., 10000 km² and higher; Figure 2.7), such as the sector of northeastern Brazil investigated in the present work. The number of publications that use DEMs and geomorphometric variables for geological discrimination is still scarce. However, some available studies have demonstrated that integrated with geological information, techniques based on DEMs and their geomorphometric variables allow to infer substrate characteristics (MILIARESIS et al., 2009; ANDRADES-FILHO et al., 2014; VALERIANO; ROSSETTI, 2017).

Miliaresis et al. (2009) assessed the potential of classification and segmentation techniques from DEMs and geomorphometric variables (slope and aspect) to advance with the geological characterization of volcanic terrains in Ischia island, Italy. The methodology used by the authors included: definition of segments (regions) using the aspect; calculation of statistics by region (e.g., mean and standard deviation) from elevation and slope; and application of unsupervised classifications to identify clusters of segments with similar geological patterns. The integration of the data revealed clusters of segments compatible with the spatial distribution of volcanic deposits.

Andrades-Filho et al. (2014) tested a geological mapping methodology based on a pixel supervised classification in a decision tree structure using geomorphometric variables, such as slope and relief-dissection and aerial geophysical data (gamaspectrometric images) in the central Paraiba Basin. The results obtained by the authors allowed the discrimination of older terrains constituted by crystalline basement rocks and younger terrains of Miocene and Quaternary deposits. Although the methodology tested by Andrades-Filho et al. (2014) was applied in a relatively small area with some well-exposed geological outcrops, the results motivate experiments using geomorphometry also in sedimentary terrains with less exposed outcrops.

Recently, Valeriano and Rossetti (2017) found promising results for the geological discrimination of sedimentary units between the Solimões and Amazonas basins (central Amazonia), applying regionalization techniques based on geomorphometric variables (e.g., elevation, slope, profile curvature, and relative relief). Basically, these techniques consist in the attribution of data for each region or mapping unit chosen from the distribution of its internal values. The experimental area must be divided into sub-areas by segmentation techniques, watersheds or other regions of interest based on the spatial distribution of numerically continuous original variables. The

data to be used in each sub-area might be a measure of central tendency (e.g., mean, mode and median) or any other formulation applied to the internal set of local data, including topographic indices of implicit regional nature, for example, relative relief and hypsometric integral. The authors established sub-areas from the segmentation of elevation, so that the mapping units had limits compatible with the different sedimentary units of the studied region. The results revealed that the regionalized variables had a higher statistical correlation each other than the local variables. These experiments motivate further investigations to discriminate sedimentary units in other sedimentary basins of Brazil.

2.3.1 DEMs

DEMs are digital representations of the Earth's surface elevation (MOORE et al., 1991). Elevation can be represented by means of regular grids with georeferenced rows and columns, triangulated irregular networks (TIN), and contour lines. In literature, there is a distinction between the term DEM, such as those that discriminate digital surface models (DSMs) and digital terrain models (DTMs), the later are representations of the bare terrain surface. In this work, we understand that DEMs represent elevation as a numerical quantity, regardless the terrain cover.

DEMs can be generated by manipulating: elevation information from contour lines and elevation points of topographic maps; stereo satellite imagery from optical or SAR multi-sensor; LIDAR point cloud data; and interferometric synthetic aperture radar (InSAR) techniques (MOORE et al., 1991; TOUTIN; GRAY, 2000; RABUS et al., 2003). Examples of DEMs derived from optical images include the 30 m spatial resolution ASTER GDEM (ABRAMS, 2000) and ALOS World 3D (AW3D) DEM (TADONO et al., 2015) (Table 2.2). DEMs derived from optical data may have artifacts due to their higher sensitivity to land and cloud cover present in the original images, which restricts their use, especially in tropical areas. Radar systems may have higher potential for use in these areas, due to the ability to penetrate through cloud targets. Moreover, while DEMs derived from radar by shorter wavelength bands (e.g., X = 3 cm and C = 5.6 cm) may be more sensitive to vegetation canopy, DEMs derived from longer wavelength bands (e.g., L = 23 cm and P = 78 cm) are the less sensitive to the so called canopy effect (HENDERSON; LEWIS, 1998).

Table 2.2 - Summary of the main characteristics of moderate spatial resolution DEMs.

DEM	Coverage (Latitude)	Wavelength	Acquisition	Spatial resolution (m)
ASTER GDEM	83°N - 83°S	0.76 – 0.86 µm	Optical stereoscopy	∼30
ALOS AW3D	82°N - 82°S	0.52 – 0.77 µm		∼30
SRTM	60°N - 56°S	∼ 3 cm (X band) and ∼5.6 cm (C band)	InSAR	∼30 and 90
WorldDEM	90°N - 90°S	∼ 3 cm (X band)		∼12

SOURCE: Abrams (2000), Rabus et al. (2003), Farr et al. (2007), Riegler et al. (2015), Tadono et al. (2015).

The generation of DEMs, such as those derived from the SRTM mission (RABUS et al., 2003), was an essential initiative by produce DEMs on an almost global scale for latitudes between 56°S and 60°N (Table 2.2). The SRTM aimed to collect topographic data using InSAR techniques on-board the Space Shuttle Endeavour during a 11-days orbit in February 2000 (RABUS et al., 2003). An antenna was located at the end of a mast 60 m away from a platform. This positioning was necessary to ensure the phase difference between the target backscattering responses (FARR et al., 2007). Initially, C-band interferometric techniques produced free 90 m spatial resolution DEMs for regions outside the United States. Recently, the 30 m spatial resolution SRTM-DEM v.3 was released in worldwide coverage, representing for many regions the highest detail of accessible data for geological discrimination. X-band SRTM-DEMs do not have global coverage and are restricted in use. Even considering the sensitivity of the SRTM-DEMs to vegetation cover (FARR et al., 2007), previous publications have shown these data may reflect land variations in areas without significant differences in tree heights (MANTELLI et al., 2009). In addition, statistical analysis comparing elevations from the top of canopy to the surface of the terrain revealed a high statistical correlation at more generalized scales in Amazonia (POLIDORI; SIMONETTO, 2014). These results suggest that large geomorphological features can be observed from SRTM data.

A first version of a global DEM called “NASADEM” is available (CRIPPEN et al., 2016). NASADEM consists in a reprocessing of the SRTM dataset. Major improvements included: precise vertical adjustments to elevation data using laser measures

from the Ice, Cloud, and Land Elevation Satellite (ICESat); reduction of SRTM data artifacts based on improved interferometric processing techniques; and use of a new topographic dataset, for instance, from ASTER GDEM, when available, to fill residual topographic gaps (CRIPPEN et al., 2016). As the results of several experiments depend on the quality DEM as input data, there remains a need to assess the potential of new versions of the SRTM-DEM, such as SRTM v.3 and NASADEM. Previous analysis (not shown here) in the study area located in low latitudes did not suggest significant differences between these versions of the SRTM-DEM.

The availability of new elevation data, such as the 12 m spatial resolution WorldDEM, derived from X-band InSAR techniques by the TerraSAR-X and TanDEM-X satellites (RIEGLER et al., 2015) (Table 2.2), has potential to carry out geological discrimination in detail scales. However, this DEM is not free and was derived using the X band, with less capacity for penetrating electromagnetic radiation through targets (HENDERSON; LEWIS, 1998). Also, a 90 m spatial resolution WorldDEM product, derived from the 12 m DEM, is now available free of charge (https://download.geoservice.dlr.de/TDM90/).

2.3.2 Geomorphometry

Geomorphometry is defined as the study of relief under a numerical approach (EVANS, 1972; PIKE et al., 2009), through terrain descriptors or geomorphometric variables. The geomorphometric variables are obtained by manipulating the digital elevation data of the DEMs (geomorphometric derivation). The Topodata project (INPE, 2008) is a Brazilian topographic database with national coverage, which provides geomorphometric variables derived from the SRTM-DEM, such as slope, aspect, and curvatures for various applications.

The manipulation of digital elevation data from DEMs allows the production of a series of local and non-local (regional) geomorphometric variables (SHARY et al., 2002). Local geomorphometric variables (e.g., slope, aspect, and curvatures) are derived from a small neighborhood of pixels around a given point. In contrast, regional geomorphometric variables (e.g., relative relief, relative height, relief-dissection, predominance, and topographic coherence) are derived from observing a large number of pixels composing a region, which may be terrain features or larger extensions of moving windows (SHARY et al., 2002).

General geomorphometric variables most used to perform geological discrimination are elevation, slope, profile curvature, and relative relief (MILIARESIS et al., 2009;

VALERIANO; ROSSETTI, 2017). Some variables used for soil and geomophological studies, but also with potential to carry out a geological discrimination are the relative height, relief-dissection (MUÑOZ; VALERIANO, 2009) and valley depth (CONRAD et al., 2015), as well as topographic coherence (VALERIANO; ROSSETTI, 2011). The hypsometric integral described previously (see section 2.2.1) is also a specific descriptor used to discriminate terrains with distinct geological characteristics (MILIARESIS et al., 2009), given its relationship with the degree of terrain maturity (e.g., old and young terrains).

Elevation (zero-order derivative) is the vertical distance of a point in the Earth's surface concerning a given reference, commonly being the mean sea level (EVANS, 1972; MOORE et al., 1991). Elevation values are represented by each pixel in DEMs. The slope (first-order derivative of elevation) can be defined as the inclination angle of the Earth's surface in relation to a horizontal plane (EVANS, 1972; MARK, 1975). This variable varies from 0 to 90°, although it can also be expressed as a percentage, from zero to infinite. The profile curvature (second-order derivative of elevation) is defined as a measure of the slope variation along a given horizontal distance, and it represents the terrain shape (i.e., concave, rectilinear, and convex) when observed in profile (PIKE, 1988; MOORE et al., 1991). Profile curvature is generally expressed in degrees per meter, with positive values related to convex terrains, negative values associated with concave terrains, and values toward zero attributed to rectilinear hillsides.

The relative relief corresponds to the difference between the maximum and minimum elevations for a given area, which can be obtained by manipulating elevation data through moving window operations (MARK, 1975). The choice of the moving window size is particularly important in the interpretation of relative relief data. The moving window size must generally be large enough to include at least two main crests or valleys. Otherwise, the results will not represent the relative relief, but only the terrain slope (EVANS, 1972). However, it is worth mentioning that there is no a universal size for the moving window, and its choice depends on the particularities of the terrain analyzed.

The relative height represents the vertical distance between a given point on the topographic surface and its projection on a reference surface (e.g., the surface of minimum elevations) (MUÑOZ; VALERIANO, 2009) (Figure 2.8a). In contrast, the relief dissection represents the vertical distance between a point on the topographic surface and its projection on the surface of maximum elevations (MUÑOZ; VALERI-

ANO, 2009) (Figure 2.8a). For instance, dissected terrains are generally related to mature terrains of older ages, while gentle and less dissected terrains may be associated with relatively younger terrains. Both the maximum and minimum elevation surfaces are derived for a given region using moving window operations. Similar to the relief-dissection is the calculation of valley depth, but using an interpolated surface from points of ridges as the reference surface of maximum elevations (CONRAD et al., 2015) (Figure 2.8a). The topographic coherence is obtained by decomposing the aspect (0 to 360°) in sines and cosines; integrating these two components by moving window; and calculating the resulting component for a given area of pixels (VALERIANO; ROSSETTI, 2011). Values of topographic coherence close to 1 are related to terrains organized in a coherent pattern (i.e., the high similarity of neighbouring aspects), while coherence values close to 0 are associated with terrains characterized by a diffuse aspect pattern.

While the size of the moving window affects the derivation of scale-dependent regional variables (Figure 2.8b), the extraction of local geomorphometric variables may be affected by the spatial resolution of the DEM. For example, the degradation of the DEM for coarser spatial resolutions did not affect statistics of elevation data, but it affected the statistics derived from the geomorphometric variables, such as slope, aspect and curvatures; the later showed low statistical correlations in coarser spatial resolutions (EL HAGE et al., 2010; GROHMANN, 2015).

Figure 2.8 - Reference surfaces to calculate regional geomorphometric variables and moving window effects.

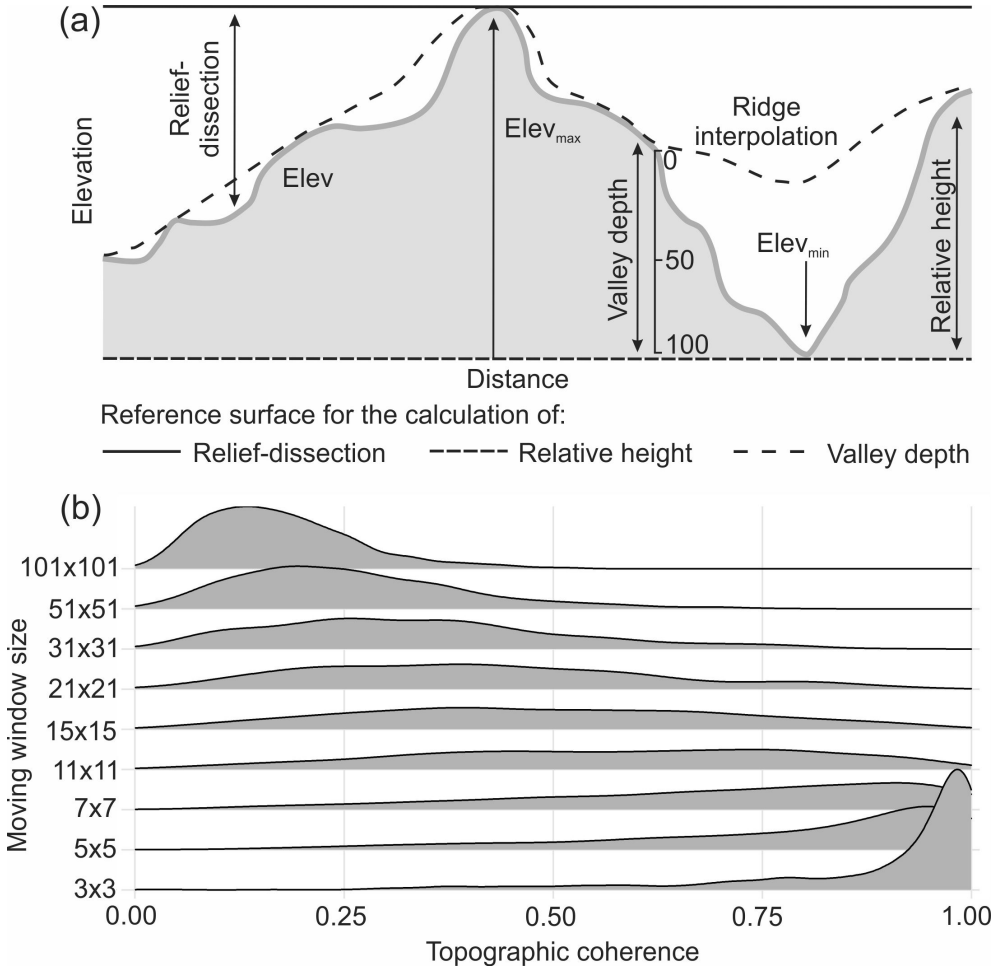

(a) Diagram representing the reference surfaces to derive the relative height, relief-dissection and valley depth (a). Elev = elevation; $Elev_{max}$ = maximum elevation; and $Elev_{min}$ = minimum elevation. (b) Effect of the size of the moving window in the derivation of topographic coherence, a scale-dependent variable. Note in b that there is a shift in the distributions, as the size of the moving window increases.

SOURCE: Diagram was modified from Muñoz and Valeriano (2009).

Histograms with asymmetric distributions, long tails and outliers can affect an adequate averaging of the geomorphometric variables, such as slope and profile curvature, as well as compromise the results of statistical analysis (e.g., parametric statistical analysis). Csillik et al. (2015) tested several methods to transform geomorphometric variables, aiming to minimize problems related to outliers and distribution shapes (e.g., skewness and kurtosis). The results obtained by these authors showed that the Box-Cox (for slope) and arctangent (for curvature) methods were

the best to normalize these variables based on several reliefs and DEMs. The methods commonly used to obtain well-behaved distributions are based on transforming (i.e., normalizing) the original scale of the geomorphometric variables to another scale by changing their original skewness and kurtosis close to the normal distribution shape; see Csillik et al. (2015) and references therein. The Box-Cox transformation (BOX; COX, 1964) can be used to approximate the distribution of geomorphometric data to a normal distribution model. To obtain a normal distribution, this method identifies an exponent (λ) for which all the values are raised (CSILLIK et al., 2015)(Table 2.3). These authors found that the normalization of slopes and curvatures can be obtained mostly by restricting the λ intervals between -4 and 4.

Table 2.3 - Interval of λ exponents based on the Box-Cox transformation for the normalization of geomorphometric data (y).

λ	-4.0	-3.0	-2.0	-1.0	-0.5	0.0	0.5	1.0	2.0	3.0	4.0
y	$1/x^4$	$1/x^3$	$1/x^2$	$1/x$	$1/\sqrt{x}$	log x	$\sqrt{x}$	x	x^2	x^3	x^4

SOURCE: Adapted from Csillik et al. (2015).

Evans (1984) proposed the following equation for the normalization of curvature distribution:

$$TransformedCurvature = \arctan(k \times curvature) \tag{2.8}$$

where k represents a parameter with a positive value to give normalized curvature with kurtosis close to 0 (EVANS, 1984; CSILLIK et al., 2015).

2.3.3 Techniques for geomorphometric characterization of terrain

Given the global cover of DEMs, such as those of the SRTM, some studies have tested their potential application for the geomorphometric characterization of geomorphological features (DRăGUţ; BLASCHKE, 2006; GERENTE et al., 2018; MOREIRA, 2018) and, secondarily, geological discriminations (MILIARESIS et al., 2009; ANDRADES-FILHO et al., 2014; VALERIANO; ROSSETTI, 2017). Based on these studies, the techniques commonly applied for the geomorphometric characterization of terrain included segmentation, regionalization of geomorphometric variables and image classification. However, it is important to note that the observation of spatial patterns of terrains by visual and/or exploratory data analysis can also help in the

geomorphometric characterization of geological terrains. For instance, older terrains are generally characterized by high dissected topography and the development of hillsides with higher slopes than younger terrains.

Studies related to geographic object-based image analysis (GEOBIA) (BLASCHKE et al., 2014), which takes into account the characteristics of the surrounding pixels, have been suggested with potential for terrain geomorphometric characterization, as opposed to the traditional pixel-by-pixel image analysis (MILIARESIS et al., 2009; DRĂGUŢ; BLASCHKE, 2006; DRĂGUŢ; EISANK, 2011; VALERIANO; ROSSETTI, 2017). Objects, the basic processing units for GEOBIA, can be generated by segmentation algorithms. Basically, the segmentation process consists of dividing the image into objects or regions, which are homogeneous in terms of spatial and spectral characteristics of the pixels (BRITES et al., 2012). Objects derived from segmentation have been used as mapping units in various geomorphometric characterizations (MILIARESIS et al., 2009; DRĂGUŢ; BLASCHKE, 2006; VALERIANO; ROSSETTI, 2017), although other units, such as watersheds (MOREIRA, 2018) or regions defined by some geomorphometric criteria, can also be considered for this purpose. As the mapping units depend on the scale of analysis (DRĂGUŢ; EISANK, 2011), generalization techniques from DEMs may be necessary for discriminations at regional scales. The regionalization of geomorphometric variables is an example of these techniques, as detailed in item 2.3. (MILIARESIS et al., 2009; DRĂGUŢ; BLASCHKE, 2006; VALERIANO; ROSSETTI, 2017).

One of the most used techniques for image segmentation in remote sensing is the region's growing method (BRITES et al., 2012). Basically, this method comprises the following steps: generation of seed points over the image to start the initial regions; comparisons between the surrounding regions by considering a similarity threshold (e.g., average pixel intensity value); and statistical comparison between the means. The definition of a threshold for the area extension is also required. These criteria will define iteratively whether the regions will be grouped or whether they will remain individualized. The multiresolution segmentation algorithm (BAATZ; SCHÄPE, 2000) has shown promising results for the segmentation of remote sensing data, including DEMs (DRĂGUŢ; BLASCHKE, 2006; DRĂGUŢ et al., 2010; EISANK et al., 2014). This algorithm uses a similarity criteria based on the concept of internal heterogeneity of regions (BAATZ; SCHÄPE, 2000) through the scale, shape, color, smoothness, and compactness parameters. The scale (a dimensionless parameter of segmentation) determines the maximum heterogeneity allowed for the image objects. The scale parameter controls the size of objects, in which: higher scale thresholds generate

larger objects and vice versa; the shape and color parameters have weights summing 1, the latter being related to the image brightness characteristics; the shape is further subdivided by the parameters smoothness and compactness, and they have weights summing 1; higher compactness values produce more compact objects, with less smooth edges and vice-versa.

A fundamental step in the segmentation process by the multiresolution segmentation algorithm is the definition of the scale parameter to obtain meaningful objects for the desired analysis, and to avoid, for example, an over or under-segmentation, which produces noisier and weaker segmentations, respectively (DRĂGUŢ; BLASCHKE, 2006). Recently, Drăguţ et al. (2010) developed a semi-automatic ESL algorithm to estimate an optimum value for the scale parameter and to produce more homogeneous objects from remote sensing images, instead of using trial and error-based analyses. The ESL algorithm compares segmentations iteratively at various levels of scale, calculating the local variance (i.e., average standard deviation of the objects in each scale), as an indicator of image variability. However, as this method requires image statistics to calculate the local variance, the presence of outliers and/or artifacts in the original topographic data may generate unreliable objects. Therefore, comparative analysis of objects by visual interpretation is still required to achieve more reliable results.

While segmentation techniques focus on the image objects, general image classification techniques, using semiautomatic algorithms or visual image interpretation group the image objects or pixels into thematic classes or sectors with similar terrain characteristics. A variety of unsupervised (e.g., ISOSEG and k-means) and supervised (e.g., decision tree) classifiers have been applied for the geomorphometric characterization of terrains (MILIARESIS et al., 2009; ANDRADES-FILHO et al., 2014; GERENTE et al., 2018; MOREIRA, 2018). Among them, the Random Forest (RF) (BREIMAN, 2001), a combination of several decision trees, showed promising results in different applications, including geological discrimination; see for instance, Cracknell and Reading (2014).

3 STUDY AREA

The study area is located in northeastern Brazil (Figure 3.1) encompassing the Paraíba, Pernambuco, and Rio Grande do Norte states. The main fluvial systems in this region are the Curimataú, Camaratuba, Mamanguape, and Miriri rivers, and the lower course of the Paraíba River, with discharge into the South Atlantic Ocean (Figures 3.1a and 3.2). Most of these rivers have SW-NE oriented courses following the main trend of regional lineaments. The major trunk streams have wide valleys confined to graben systems in their downstream sectors (BEZERRA et al., 2014). The Paraíba River, the longest one, has a length of 362 km, and a drainage area of $\sim$ 20196 km^2.

The western sector of the study area is composed by a complex of deformed Precambrian terrains of the Borborema Province (ALMEIDA et al., 1981), with various lithologies, ages, origins, and evolutions (BRITO-NEVES et al., 2004; ARTHAUD et al., 2008; VAN SCHMUS et al., 2008). Precambrian metamorphic and igneous rocks (e.g., gneisses, migmatites, schists, and granites) are the most representative group of rocks in this sector, followed by small occurrences of Cretaceous igneous rocks to the east (Itapororoca Formation) (BARBOSA; BRAGA, 1974), and sandstones of the Serra dos Martins Formation, presumably of Paleogene age (MABESOONE, 1966)(Figure 3.2). The Borborema Province covers $\sim$ 900 km long and $\sim$ 600 km wide (BEZERRA et al., 2011) and is bounded by the Sao Francisco Craton to the south, and Parnaíba Basin to the west, as well as several adjacent sedimentary basins (Figure 3.1a). This province was built by the collision of the São Luis/West Africa and São Francisco/Congo cratons (West Gondwana amalgamation) during the Brasiliano/Pan-African orogeny (750-540 Ma) (ALMEIDA et al., 1981; ALMEIDA et al., 2000; ARTHAUD et al., 2008).

Figure 3.1 - Map of northeastern Brazil with the regional tectonic trends, geological framework, main rivers, morphology and location of the study area.

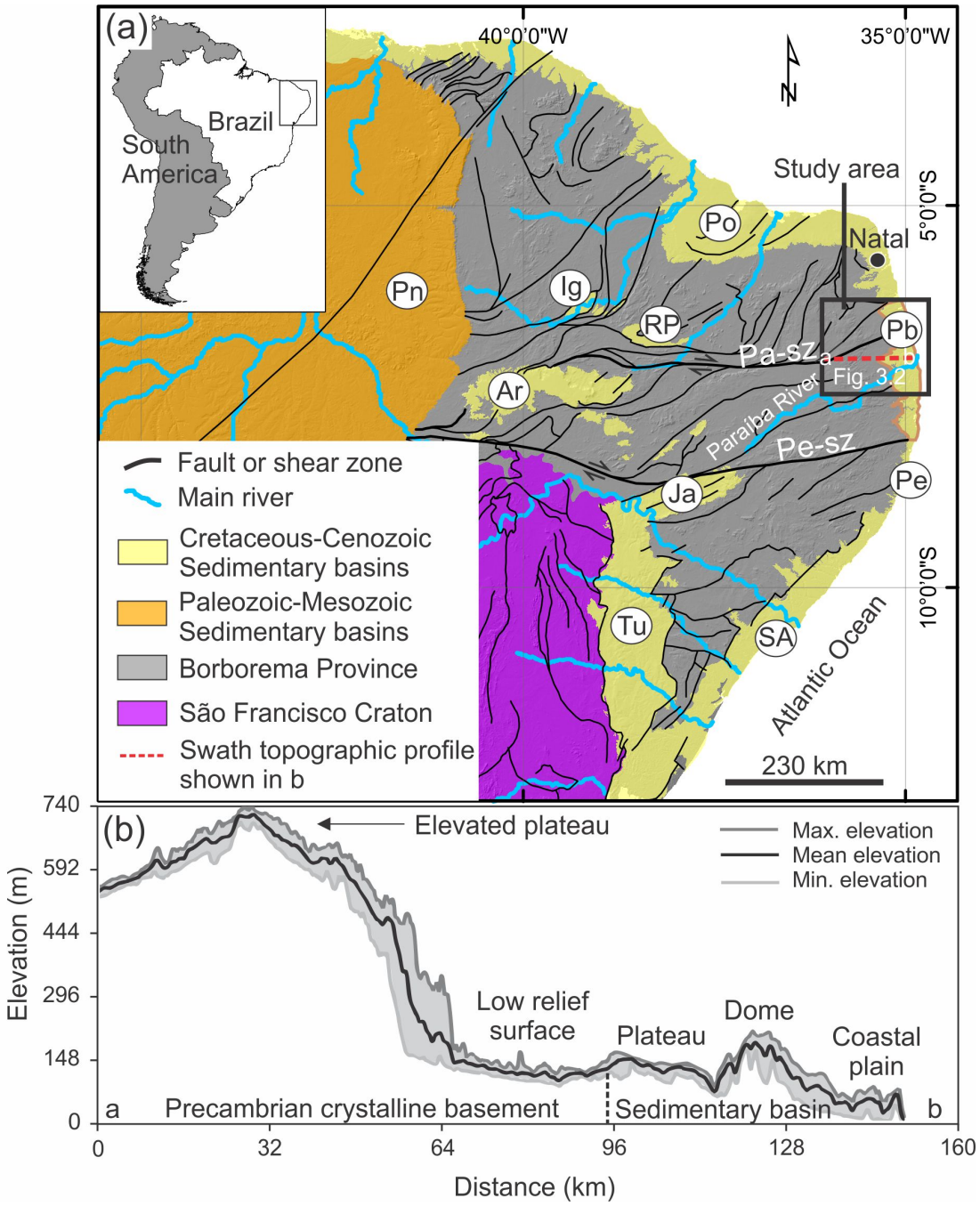

(a) Shear zones in a: Pa = Patos; Pe = Pernambuco. Sedimentary basins: Ar = Araripe; Ig = Iguatú; Ja = Jatobá; Po = Potiguar; Pb = Paraíba (brown boundaries); Pe = Pernambuco; Pn = Parnaíba; RP = Rio do Peixe; SA = Sergipe-Alagoas; Tu = Tucano. (b) Swath topographic profile derived from the SRTM-DEM, showing the regional morphology of the study area.

SOURCE: Gómez et al. (2019).

Figure 3.2 - Regional geology of the study area and location of main trunk streams.

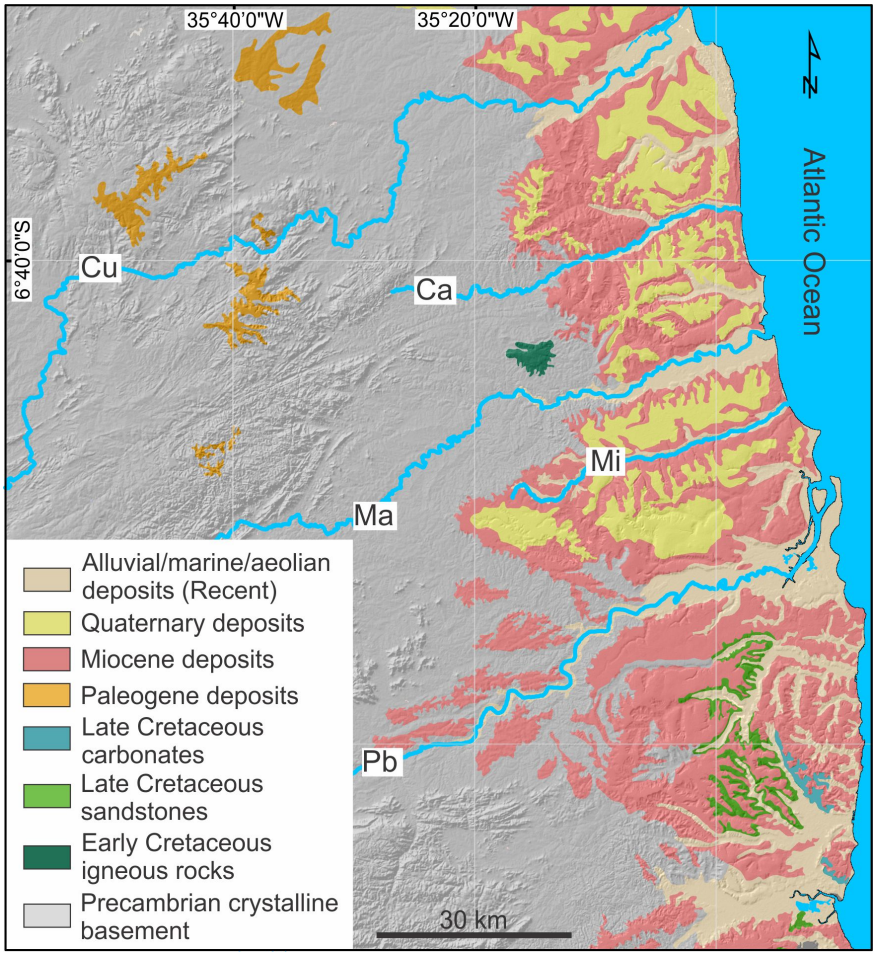

Trunk rivers: Cu = Curimataú; Ma = Mamanguape; Mi = Miriri; Pb = Paraíba. Shaded relief was derived from the SRTM-DEM. Geological units simplified from the CPRM geological map at 1:1000000 scale (http://geosgb.cprm.gov.br/geosgb).

SOURCE: Author's production.

Many pre-existing tectonic structures of the Borborema Province were generated or reactivated during the Brasiliano/Pan-African cycle (BEZERRA et al., 2011). Shear zones, such as the Patos and Pernambuco, are the most prominent tectonic features of this region (ARTHAUD et al., 2008) (Figure 3.1). These are NE and E-striking dextral strike-slip faults, with hundreds of kilometers long and 1 to 10 km wide (BEZERRA et al., 2014). In particular, the Pernambuco shear zone constitutes a present-day active seismogenic zone (FERREIRA et al., 2008; LOPES et al., 2010; LIMA NETO et al., 2013).

The last major tectonic event affecting the Borborema Province and the South Amer-

ica platform after the Brasiliano cycle was the Pangea break-up in the Mesozoic, which culminated with the opening of the South Atlantic Ocean and development of marginal sedimentary basins along the passive margin and intracontinental aborted rifts (MATOS, 1992; BEZERRA et al., 2008). Precambrian shear zones are considered as weakness zones, as they were reactivated in a brittle manner, controlling the location and geometry of many sedimentary basins in NE Brazil during the early rifting stages (BEZERRA et al., 2014; MARQUES et al., 2014; NOGUEIRA et al., 2015; VASCONCELOS et al., 2019b). The reactivation of some shear zones may also have influenced the formation of oceanic fracture zones during the Pangea break-up (VASCONCELOS et al., 2019a). The post-rift evolution of northeastern Brazil is also marked by tectonic reactivation of pre-existing Precambrian structures (ROSSETTI et al., 2011b; GURGEL et al., 2013; BEZERRA et al., 2014; LIMA et al., 2017), as well as basin inversions, as recorded in the Potiguar (BEZERRA et al., 2020), Sergipe-Alagoas (VASCONCELOS et al., 2019b), Araripe (MARQUES et al., 2014) and Rio do Peixe basins (NOGUEIRA et al., 2015) (Figure 3.1).

The Paraíba Basin, which bounds the Borborema Province to the east, was the last bridge between the South American and African continents (SUGUIO; MARTIN, 1996). The Pernambuco shear zone limits this basin to the south and the Mamanguape fault to the north, a branch of the Patos shear zone (brown boundaries in (Figure 3.1a). The oldest geological units of the Paraíba Basin include Cretaceous sandstones of the Beberibe Formation (Coniacian-Santonian) (BEURLEN, 1967), limestones and calciferous sandstones of the Itamaracá Formation (Campanian-Maastrichtian) (KEGEL, 1955), and limestones of the Gramame Formation (Maastrichtian) (BEURLEN, 1967), with the latter being recorded only as small occurrences in the southern sector of the study area (Figure 3.2). The post-rift infill of the Paraíba Basin consists of Miocene (Barreiras Formation) and Late Quaternary deposits (Post-Barreiras Sediments), both represented by sandstones, mudstones and heterolithic deposits, as well as conglomerates (BARBOSA et al., 2003; ROSSETTI et al., 2012). The Barreiras Formation, first attributed to essentially continental environments, was reinterpreted as having deposits formed in various coastal, mainly estuarine environments; see Rossetti et al. (2013) for a review. The Post-Barreiras Sediments (ROSSETTI et al., 2012) include two informal stratigraphic units dated from the late Pleistocene (PB1) and early/middle Holocene (PB2) (Figure 3.3). PB1 consists of sandstones interbedded with mudstones and conglomerates, formed by marine (GANDINI et al., 2014) or alluvial (fluvial and gravitational) processes (ROSSETTI et al., 2012). PB2 is represented by friable and massive, mostly aeolian sands (ROSSETTI et al., 2012). Most of the study area is covered by Miocene and Late

Quaternary deposits (Figure 3.3), which overlay discordantly Precambrian basement rocks to the west. In addition to these geological units, recent (late Holocene) alluvial sediments occur along main fluvial valleys, and marine/aeolian sediments cover coastal plains.

Figure 3.3 - Detailed geological map of the northern Paraíba Basin.

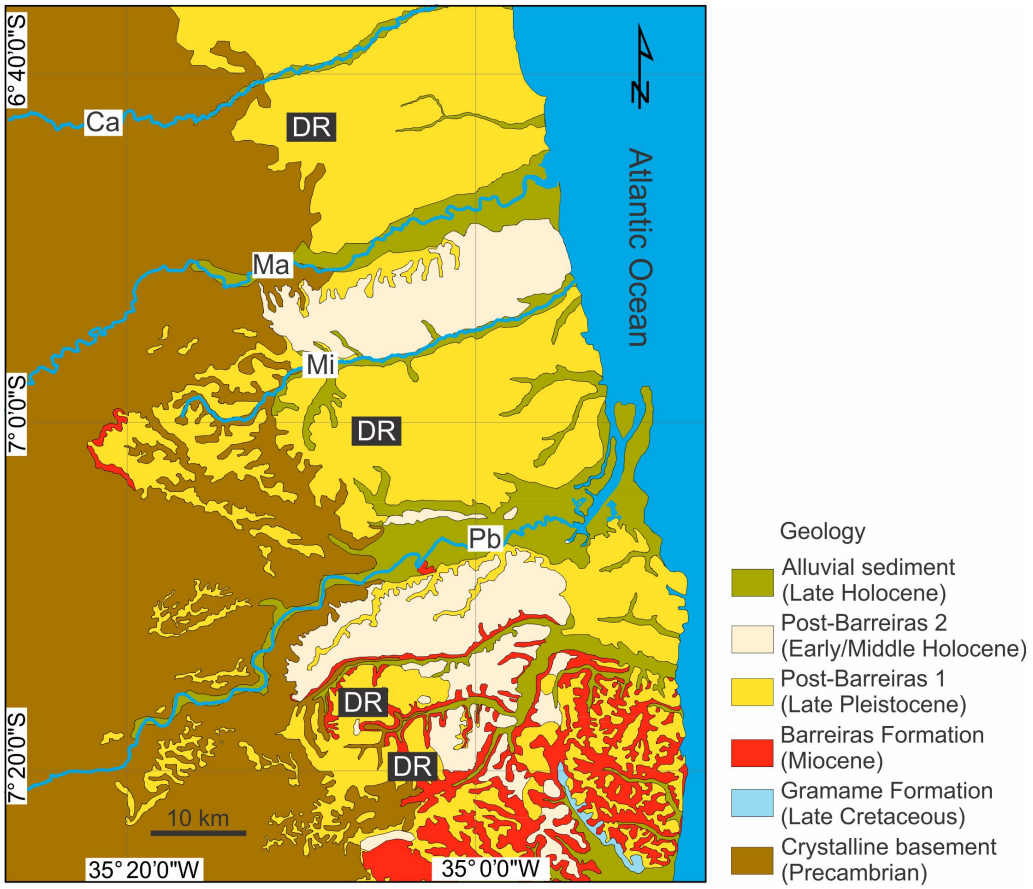

Trunk streams: Ca = Camaratuba; Ma = Mamanguape; Mi = Miriri; Pb = Paraíba. DR = Dome-like relief.

SOURCE: Geological map after Rossetti et al. (2012).

The general landforms of the study area consist of crystalline massifs and low-relief terrains of the Sertaneja Depression or Superfície Pré-litorânea (COSTA et al., 2020) over the Precambrian basement to the west. To the east, this area records: tilted coastal tablelands, which form a series of uplifted and subsided blocks from north to south over the Paraíba Basin; domic morphologies located at higher topographic levels; and a chevron-shaped plateau (Figures 3.1b and 3.3).

4 MATERIALS AND METHODS

This chapter contains the description of data and resources used for data processing. The steps taken to achieve the proposed aims are also described, including: DEM preprocessing; extraction and morphological analyses of the drainage network; calculation of swath profiles and geomorphic indices; fluvial erodibility; knickpoint identification and estimation of incision; assessment of divide stability; geological discrimination by geomorphometry; and validation with geological field data.

4.1 Data

The main cartographic and remote sensing data used in this work included: four tiles of the 30-m spatial resolution SRTM-DEM v.3 and corresponding water body data (http://earthexplorer.usgs.gov/); two tiles of the local geomorphometric data layers of slope, aspect, plan, and profile curvatures provided by Topodata database (http://www.dpi.inpe.br/topodata); airborne magnetometric geophysical data in raster format from Geological Survey of Brazil (CPRM) (http://geosgb.cprm.gov.br/geosgb); geological data in vector format from official geological maps produced by the CPRM at 1:1000000 (Paraíba, Pernambuco and Rio Grande do Norte states; http://geosgb.cprm.gov.br/) and 1:500000 scales (Paraíba State only) (SANTOS et al., 2002), as well as from other publications (ROSSETTI et al., 2012); and geological field data consisting of twenty-three road-cut outcrops, two coastal cliffs, and three groundwater drilling holes provided by CPRM (CPRM, 2001). The field record also included sixty-two ground truth points obtained by the geographic positioning system (GPS) (ANDRADES-FILHO et al., 2014) and some photographs of outcrops from previous field campaigns in the study area. These data were analyzed and integrated using a geographic coordinate system and WGS84 datum within a geodatabase structure in the ArcGIS software. However, when necessary, the data were also converted into UTM coordinates to calculate geomorphic indices and to measure area and distance.

4.2 Softwares, algorithms and available codes

The main softwares, algorithms and codes used in the present work were:

a) TerraHidro v. 0.4.2 (ROSIM et al., 2013), for the extraction of drainage network and sub-basins;

b) TerraView v. 5.2.1. (http://www.dpi.inpe.br/terralib5/wiki/), for the segmentation of geomorphometric variables based on the multiresolution algorithm (BAATZ;

SCHÄPE, 2000);

c) SAGA GIS, for the calculation of the variable valley depth (CONRAD et al., 2015);

d) SwathProfiler and Nprofiler algorithms available in Python (PÉREZ-PEÑA et al., 2017) for the generation of swath profiles and calculation of normalized river long profiles and THi^* index;

e) Codes available in Python, for the normalization of local geomorphometric variables (CSILLIK et al., 2015);

f) R (https://www.r-project.org/) for the processing of geomorphometric variables and statistical analysis, and Matlab (https://www.mathworks.com/) for the calculation of concavity and steepness indices, as well as divide stability analysis;

g) ChiProfiler (GALLEN; WEGMANN, 2017), Topographic Analysis Kit (TAK) (FORTE; WHIPPLE, 2019), DivideTools (FORTE; WHIPPLE, 2018) and TopoToolbox (SCHWANGHART; SCHERLER, 2014) for river profile and divide stability analyses;

h) ArcGIS (https://desktop.arcgis.com) for the creation of geodatabase, data manipulation, spatial analysis, geoprocessing, and elaboration of map layouts.

4.3 DEM preprocessing

The SRTM-DEM was pre-processed by merging the four tiles covering the study area into a mosaic and applying a binary mask created from the SRTM water body data (water = without digital number - NoData; and non-water with digital number = 1) to avoid the influence of spurious values of major water bodies in topographic analyses. This DEM was also clipped using the polygon boundaries of the study area. Lakes/reservoirs-related missing values were filled using minimum topographic values derived from surrounding pixels in order to generate a continuous drainage network. The application of a 3x3 mean moving window was required to smooth the topographic data and eliminate outliers.

4.4 Extraction and morphological analysis of the drainage network

The DEM was used as input to extract the drainage network and the sub-basins with the support of the priority first search (PFS) method, implemented in the TerraHidro software. This algorithm has shown better performance concerning the extraction of drainage networks in relatively flat areas than other traditional methods (ROSIM et al., 2013). The extraction of the drainage network was achieved by

converting the DEM data to flow direction and contribution area, and then converting the drainage cells into vector data. The drainage cells were best identified using a minimum contribution area of 0.9 km². However, even after the extraction of the drainage network, some sectors were identified, represented by either disconnected or missing channels. These sectors were manually edited and guided by visual interpretation over plan curvature, aspect and topographic coherence variables (Chapter 2, item 2.3.2). The later was used due to the ability to highlight thalwegs and ridges. The channels and drainage patterns were characterized based on the criteria presented in the theoretical background (HOWARD, 1967; DEFFONTAINES; CHOROWICZ, 1991)(Chapter 2, item 2.1.2.) on a fixed scale of 1:100.000.

4.5 Calculation of swath profiles and geomorphic indices

SRTM-DEM was used as input for all the topographic analyses in this work. However, some analyses were performed using input vector data (e.g., drainage network and drainage basin) generated by different algorithms and geological maps at different scales. This strategy was used in order to follow specific topographic routines and to avoid scale-related issues. The *AF* index, normalized river profiles and swath profiles were compared with the more detailed geological map of the study area (ROSSETTI et al., 2012), while the k_{sn} and the knickpoint and divide stability analyses, as detailed below, were compared with the regional geological map from CPRM at 1:1000000 scale.

The relief morphology of the study area was investigated by swath profiles. The swath profiles were extracted from the SRTM-DEM (see the location in Figure 5.1) based on the automatic Swath Profiler algorithm, implemented in ArcGIS (PÉREZ-PEÑA et al., 2017). The creation of five rectilinear swath profiles over the dome-shaped reliefs prevented over and under-sampling of topographic data, which are common in the curved segments of swath profiles (TELBISZ et al., 2013). A swath profile parallel to the main river was also created to assess the response of tributaries to base level changes. The swath profiles were calculated using a step size of 45 m and a swath width of 5 km. The latter threshold, which covered most of the dome-shaped reliefs, is considered adequate to avoid arbitrary peaks and to capture large pieces of remnant surfaces (TELBISZ et al., 2013). The mean, maximum, and minimum elevation curves, as well as the relative relief curves, were extracted from the swath profiles. The resulting topographic curves were analyzed to verify tectonic-related morphological features. The potential application of the *THi** (Chapter 2, item 2.2.1) was also tested using a recent algorithm implemented in ArcGIS (PÉREZ-PEÑA et al., 2017).

The $THi*$ index and the relative relief curves were filtered using a mean moving window with a selected interval of approximately 400 m, based on previous tests.

The basin asymmetry was investigated using the AF index (HARE; GARDNER, 1985). This index was calculated through the manipulation of trunk stream and drainage basin vector data and application of the equation 2.2. Eighteen sub-basins (areas $\geq$18 km^2) were extracted from the drainage network, as they represent the main set of basins close to the dome-like reliefs. Hence, these sub-basins may reveal important information about the origin and last stages of evolution of the domic morphologies. The AF values were manipulated as the absolute value minus 50 to represent the degree of asymmetry from 0. Tilting direction was inferred based on the main displacement of the trunk stream in each sub-basin.

Normalized river long profiles were obtained using the NProfiler add-in automatic algorithm (PÉREZ-PEÑA et al., 2017). A smoothing factor was applied to all eighteen profiles to better represent the river curves, using an average moving window based on the percentage of 10 profile points. H_{max} and E_q values (Chapter 2, item 2.2.3.1) were extracted based on the river long profiles. H_{max} values were used to define groups of rivers with similar shapes, based on the cluster analysis.

Forty-three rivers were used to calculate the k_{sn} values based on the integral method (PERRON; ROYDEN, 2013) by adjusting linear regression bounds for river segments above and below knickpoints. These rivers were selected because they flow over a range of lithologies and follow main tectonic structures of the study area. A θref of 0.45 was defined to allow comparisons with other works (see item 2.2.3.2) and the chi integration was calculated using a A_0 of 1 m^2 to ensure that the slope of the profile is the k_{sn} (PERRON; ROYDEN, 2013; GALLEN; WEGMANN, 2017). As additional criteria to better define the river profiles of the study area, we defined: a critical threshold drainage area A_{cr} of 1 km^2 or higher to eliminate upstream river segments dominated by debris-flow processes (WOBUS et al., 2006; KIRBY; WHIPPLE, 2012); and an average moving window size of 250 m to smooth river profiles. The average k_{sn} values were also calculated for drainage segments based on stream segment lengths of 1 km, since k_{sn} values are strongly variable over short distances.

4.6 Fluvial erodibility

In order to assess the influence of spatial variability of rock types on k_{sn}, a fluvial erodibility analysis was required. Quantify the fluvial erodibility of rock types is difficult, as it varies with other parameters (e.g., rock mass strength, jointing,

and weathering) (BURSZTYN et al., 2015). The collection of a significant set of field data, such as mechanical measurements of rock strength (ZONDERVAN et al., 2020), is problematic in extensive areas, as in the instance of the study site. In addition, determining the erodibility coefficient K (equation 2.4) is challenging, which is mostly due to the lack of data and robust methodologies (HAREL et al., 2016). Alternatively, the rock-type average k_{sn} can be used as a simple way to verify the influence of bedrock erodibility on k_{sn} values, as it takes into account only the lithological character of rock-types (MARLIYANI et al., 2016; GALLEN, 2018; BERNARD et al., 2019; ZONDERVAN et al., 2020). The geological map produced by the CPRM at 1:1000000 scale served the purpose of defining rock groups and assigning average k_{sn} values using a total of 10000 random samples. The total number of samples was distributed proportionally to the surface area of the rock groups. For simplification, the geological units of the study area were grouped empirically into three main groups in terms of relative resistance to erosion: (i) low resistant sedimentary rocks; (ii) moderately resistant metamorphosed rocks; and (iii) more or less massive, highly resistant igneous and meta-igneous rocks units (Table 4.1). This analysis was not applied to the alluvial/marine/aeolian deposits in order to avoid abrupt changes in k_{sn} related to depositional channel segments (MARLIYANI et al., 2016).

Table 4.1 - Summary of ages, main lithologies, geological units, and groups of rocks exposed in the study area, according to their relative resistance to erosion.

Age	Main lithology	Name of surface geological unit	Relative resistance to erosion
*Quaternary	Sandstones	Post-Barreiras (PB1 and PB2)	Low resistant sedimentary rocks
Miocene	Sandstones and mudstones	Barreiras	
Paleogene	Sandstones	Serra dos Martins	
Late Cretaceous	Sandstones and limestones	Beberibe and Gramame	
Early Cretaceous	Phonolith and rhyolite	Itapororoca	Igneous, more or less massive, highly resistant
Neoproterozoic	Schists	Seridó	Metamorphosed sediments, moderately resistant
Neoproterozoic, Mesoproterozoic and Paleoproterozoic	Gneisses, migmatites, and granites	Suíte Várzea Alegre, Serrinha Pedro Velho units 1-2-3-4, Cabaceiras, Salgadinho, Serra de Jabitacá, Sertânea, Recanto - Riacho do Forno, São Caetano, Campina Grande, Esperança, Monte de Gameleiras, Serra Redonda, São Lourenço, Sumé, and Dona Inês and Caxexa plutons	Igneous and meta-igneous, more or less massive, highly resistant

* after Rossetti et al. (2012).

SOURCE: Author's production.

4.7 Knickpoint identification and estimation of incision

Knickpoints-related convexities were identified through distance-elevation and χ-elevation plots and classified as vertical-step and slope-break end-member morphologies based on the interpretation of spikes and breaks in log-log slope-area graphs, respectively (Figure 2.5b-e). The vertical (elevation) and horizontal (e.g., distance from mouth and distance from divide) components of knickpoint retreat were extracted and compared to each other based on linear regressions to analyze the formation and behaviour of the studied knickpoints. The horizontal components were also examined with the drainage area using linear regressions in the form of a power-law equation ($L = kA^h$) to be compared to Hack's law (HACK, 1957).

To verify statistically the presence/absence of two clusters of knickpoints, we derived some knickpoint attributes and applied two hypothesis tests, unpaired two-samples T-test and Mann-Whitney U test (NOETHER, 1991; VENABLES; SMITH, 2007). The first test (parametric test) uses the test statistic of difference in means of the two groups, while the second one (non-parametric test) uses the difference in medians as test statistic (NOETHER, 1991). In order to attend the T-test assumptions, the data normality analysis using the Shapiro-Wilk test and homogeneity of variances based on Levene's test was required (VENABLES; SMITH, 2007). The knickpoint attributes compared herein included elevation, slope, relative relief, k_{sn}, total drainage area, and incision. Relative relief and k_{sn} were also tested using three sizes of moving window (1000, 3000 and 5000 m). Only the attributes which failed in the normality analysis (T-test) were submitted to the Mann-Whitney U test. The following null (h_0) and alternative (h_a) hypotheses were defined assuming a significance level (α) of 0.05: h_0 = the means/medians of the two groups of knickpoints are the same; h_a = the means/medians of the two groups of knickpoints are different.

To estimate the incision, we used the approach of projected river profiles (KIRBY; WHIPPLE, 2012). River profiles downstream of knickpoints were projected based on least squares linear fits on the χ-elevation relationship, with a confidence interval of 95% based on TAK (FORTE; WHIPPLE, 2019). The vertical difference between the present-day and projected profile elevations at the fault was taken as the estimated incision of the rivers. The position of the fault at the profile was defined based on the visual interpretation of major morphostructural lineaments in the study area. These lineaments were mapped using magnetometric geophysical data from CPRM and SRTM data at a fixed 1:100.000 scale. Known faults and shear zones were derived from previous publications (BEZERRA et al., 2008; BEZERRA et al., 2014; LIMA et al.,

2017).

4.8 Assessment of divide stability

The χ-map was generated only for the complete drainage basins with outlets > 1 m above sea level (asl) based on DivideTools (FORTE; WHIPPLE, 2018). As criteria to select the drainage divides, we analyzed only the divides bounding the major fluvial systems of the study area and the plateau. The χ and Gilbert metrics extracted at the channel heads were used as basis to assess divide stability/mobility and to infer divide migration direction (c.f., Forte and Whipple (2018)). The drainage divide was assumed to be stable when there was overlap between the mean of one side of the divide and the uncertainty of the mean of the opposite side; otherwise the divide was assumed as mobile (FORTE; WHIPPLE, 2018).

4.9 Geological discrimination by geomorphometry

Geological discrimination based on geomorphometry was achieved through the following steps: (i) manipulation of geomorphometric variables (local and regional); (ii) regionalization of geomorphometric variables (Figure 4.1); and (iii) geomorphometric characterization of geological terrains. These steps are further detailed in the following.

Figure 4.1 - Diagram illustrating the general steps used to perform the geological discrimination of the study area based on the technique of regionalization of geomorphometric variables (see text for further explanation).

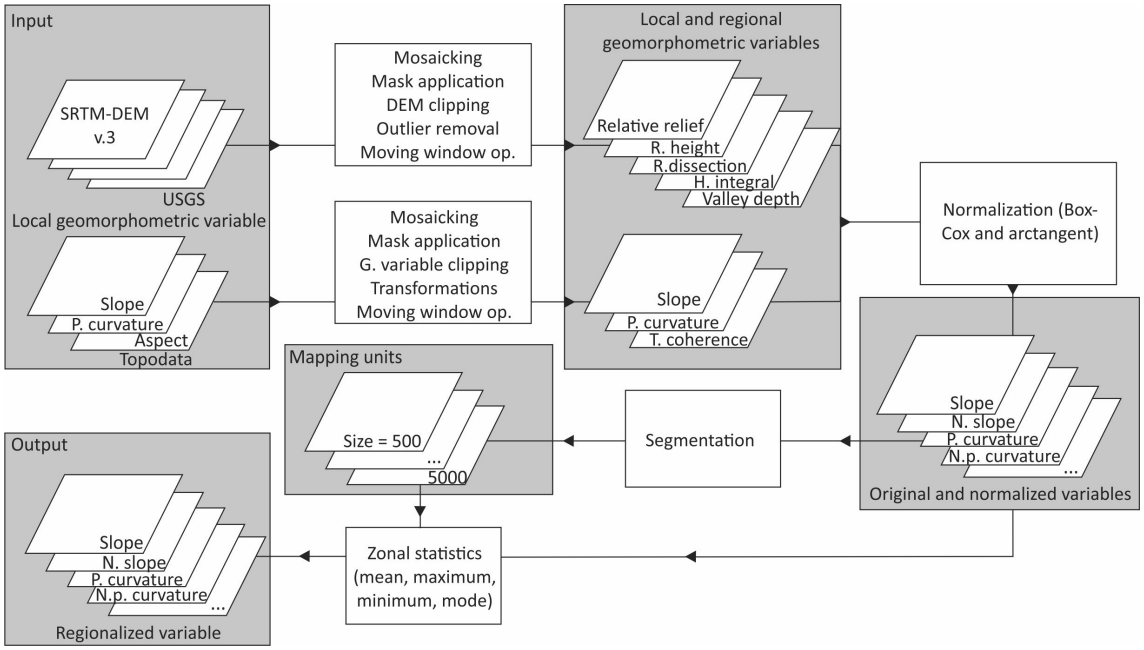

SOURCE: Author's production.

4.9.1 Manipulation of geomorphometric variables

Similar to the SRTM-DEM preprocessing, two tiles of the local geomorphometric variables (slope, profile curvature, and aspect) of Topodata were merged into a mosaic. In order to facilitate the calculation of descriptive statistics, slope data was pre-processed by converting its original percentage values to degrees, and profile curvature values (i.e., negative and positive) were transformed into absolute values (VALERIANO; ROSSETTI, 2017). Relative relief, relative height, relief-dissection, topographic coherence, hypsometric integral, and valley depth were tested as regional variables. The calculation of these variables involved steps of moving window operations (see item 2.3.2). Eight different sizes of moving windows were tested herein (3x3, 5x5, 7x7, 11x11, 15x15, 21x21, 31x31, and 51x51). While smaller moving window sizes produced noisier geomorphometric variables, larger moving window sizes produced more generalized variables with loss of detail. Based on visual image inspections, we defined the 7x7 (area = 0.04 km^2) and 21x21 (area = 0.39 km^2) as optimum moving window sizes to derivate the regional geomorphometric variables.

Only for topographic coherence, two sizes of moving windows were applied (i.e., 7x7 and 21x21), as the results showed different topographic patterns with potential to discriminate the geological units of the study area.

Box-Cox transformation (BOX; COX, 1964) for slope and arctangent for profile curvature (EVANS, 1984) were applied using Python codes developed by Csillik et al. (2015). Box-Cox method was applied using the λ exponent intervals of - 0.5, 0.0, 0.5, 1.0, and 2.0 (Table 2.3). The focus was on this range because the application of extreme exponents did not show reliable results for the geological discrimination, as revealed by previous tests. For the λ exponents ≤ 0, the minimum geomorphometric value (e.g., slope = 0) was transformed to 1 before normalization, since the logarithm of 0 is undefined (CSILLIK et al., 2015). For the profile curvature, iterative simulations of the algorithm by Csillik et al. (2015) using regular intervals to estimate the k parameter suggested a value of 31.4, as the lowest kurtosis value to normalize this variable by the arctangent transformation. Therefore, this value was used to normalize the profile curvature. The statistics of skewness and kurtosis based on R packages were calculated to evaluate the shape of the distributions before and after normalization.

4.9.2 Regionalization of geomorphometric variables

The regionalization of geomorphometric variables was performed based on the following steps of zonal statistics: (i) definition of the mapping unit as a zone layer; (ii) selection of one geomorphometric variable as a basis to calculate the statistics for each zone; and (iii) assignment of the statistics by region. The mapping units (i.e., set of image objects) were generated by the multi-resolution segmentation algorithm based on Baatz and Schäpe (2000) available in the TerraView v. 5.2.1 software. As input parameters to run the algorithm, we tested optimum scale values into the range of 500 to 5000. The other parameters were kept in the default algorithm configuration (color = 0.90; compactness = 0.5; and similarity = 0.030). However, given the dificulty to separete similar geomorphometric signatures between different geological terrains, additional operations to generate new mapping units, for instance, using the geomorphometric similarity of segments through some central tendency measure (e.g., slope mode) were also considered in the present analysis. A total of fifteen variables, i.e., including original variables and after normalization, were tested for regionalization. The mean, maximum, minimum, and mode were tested for the statistics. The original variable values were transformed from float to integer to calculate the mode. For the variables with the range between 0 and 1 (e.g.,

hypsometric integral and topographic coherence), a minimum factor (e.g., 10) was applied to expand their ranges before transforming into integer values.

4.9.3 Geomorphometric characterization and hierarchical levels of geological discrimination

The geomorphometric characterization was carried out to verify the pertinence of attributing a geological meaning to the regionalizations. This step was performed based on visual interpretation of terrain characteristics and by selecting critical thresholds in order to individualize terrain patterns with distinct geomorphometric signatures. Some key geomorphometric elements interpreted from exploratory data analysis were used to help the geological discrimination in two distinct, general and detailed hierarchical levels (Table 4.2). The general level consisted of the discrimination between the Miocene-Quaternary deposits-related terrains (i.e., Barreiras Formation and Post-Barreiras Sediments, respectively) and the underlying pre-Miocene basement rocks. The level of detail included the discrimination between the terrains represented by the units of Barreiras Formation and Post-Barreiras Sediments, using the polygonal boundaries derived from the general level. In addition, the study area was divided into three sectors (north, central, and south) and the geological discrimination was performed for each sector at both levels. This strategy was used aiming to obtain better control of the data (e.g., definition of a specific threshold), considering that local lithological and/or topographic variations may affect the geomorphometric signatures of terrains.

Table 4.2 - Geomorphometric key-elements used to help the geological discriminations (at the general and detail levels) of the study area.

Variable	General level	
	Pre-Miocene basement rocks	Miocene-Quaternary deposits
Valley depth	River valleys with higher depths. The eroded crystalline basement terrains may also present lower values of valley depth	River valleys with lower depths. Major valleys or valleys confined to grabens may also show higher valley depth values. Topographic breaks (paleoshoreline and coastal plain) may also present higher valley depth values
Slope	Terrains with higher slopes. The eroded crystalline basement terrains are exceptions	Terrains with lower slopes
Elevation	Terrains with relatively higher elevations. Eroded crystalline basement terrains with low topography are exceptions	Terrains with relatively lower elevations. Plateaus and dome-related sedimentary terrains with high topography are exceptions
Hypsometric integral	Mature terrains with lower hypsometric values and high degree of dissection	Less dissected younger terrains, with higher hypsometric values
Topographic coherence	Terrains configured by diffuse aspect patterns, with moderate to lower coherence values	Terrains configured by coherent aspect patterns, with moderate to higher coherence values
	Detail level	
	Barreiras Formation	Post-Barreiras Sediments
Slope	Terrains with higher slopes. Proximity with major river valleys	Terrains with lower slopes. Occurrences toward drainage divides
Profile curvature	Terrains with convex and concave hillsides and moderate to higher curvature values	Terrains with more rectilinear hillsides and lower curvature values
Topographic coherence	Terrains configured by diffuse aspect patterns, with lower coherence values	Terrains configured by coherent aspect patterns, with higher coherence values
Relief-dissection	Dissected terrains, with higher dissection values	Less dissected terrains, with lower dissection values

SOURCE: Author's production.

4.10 Validation with geological data

The information extracted from the morphological analysis of drainage networks and DEM-based geomorphic indices was complemented with geological field data. A transect was used to establish the regional stratigraphic correlation of the study area, combining twenty-three geological outcrops and three boreholes (Figure 4.2). These data were grouped into four geological units of interest, including the Post-Barreiras Sediments, Barreiras Formation, Gramame Formation, and crystalline basement. The GPS data provided the location of field points, and the SRTM-DEM allowed the establishment of their altitudinal positions.

The results of the geological discrimination by geomorphometry were visually compared with: some field photographs recording the regional landform descriptions of typical geological terrains (Figure 4.2); and official geological maps of the CPRM at the 1.1000000 and 1:500000 scales (SANTOS et al., 2002), as well as the geological map of Rossetti et al. (2012). There is no general agreement on formation names among the available geological maps. For the limits of the study area, the official geological maps cover the geological classes of eluvial and colluvial deposits and the Barreiras Formation (named as Group in this map); fluvial/marine/aeolian sediments were grouped into a single class. The grouping of eluvial and colluvial deposits and the Barreiras Formation into a single class (Miocene-Quaternary units) was also required for comparison with the results in the general level. In contrast, the more detailed geological map of Rossetti et al. (2012) contains the geological classes of alluvial sediments, Post-Barreiras 1 Sediments, Post-Barreiras 2 Sediments, Barreiras Formation and Gramame Formation. For simplification, the Post-Barreiras Sediments were grouped herein into a single class. For all maps, we grouped the pre-Miocene geological units, as belonging to a unique geological class (pre-Miocene basement rocks). Based on a set of 62 ground truth points as reference data (47 for Post-Barreiras Sediments and 15 for Barreiras Formation; Figure 4.2), we calculated the confusion matrix, followed by the assessment of the overall accuracy and calculation of the metrics by class (producer and user accuracies, and omission and commission errors, respectively)(CONGALTON, 1991). The assessments were carried out only for the southern sector of the study area, considering that our ground truth points are better distributed in this sector.

Figure 4.2 - Geographical distribution of geological field data used for tectonic investigation and geological discrimination.

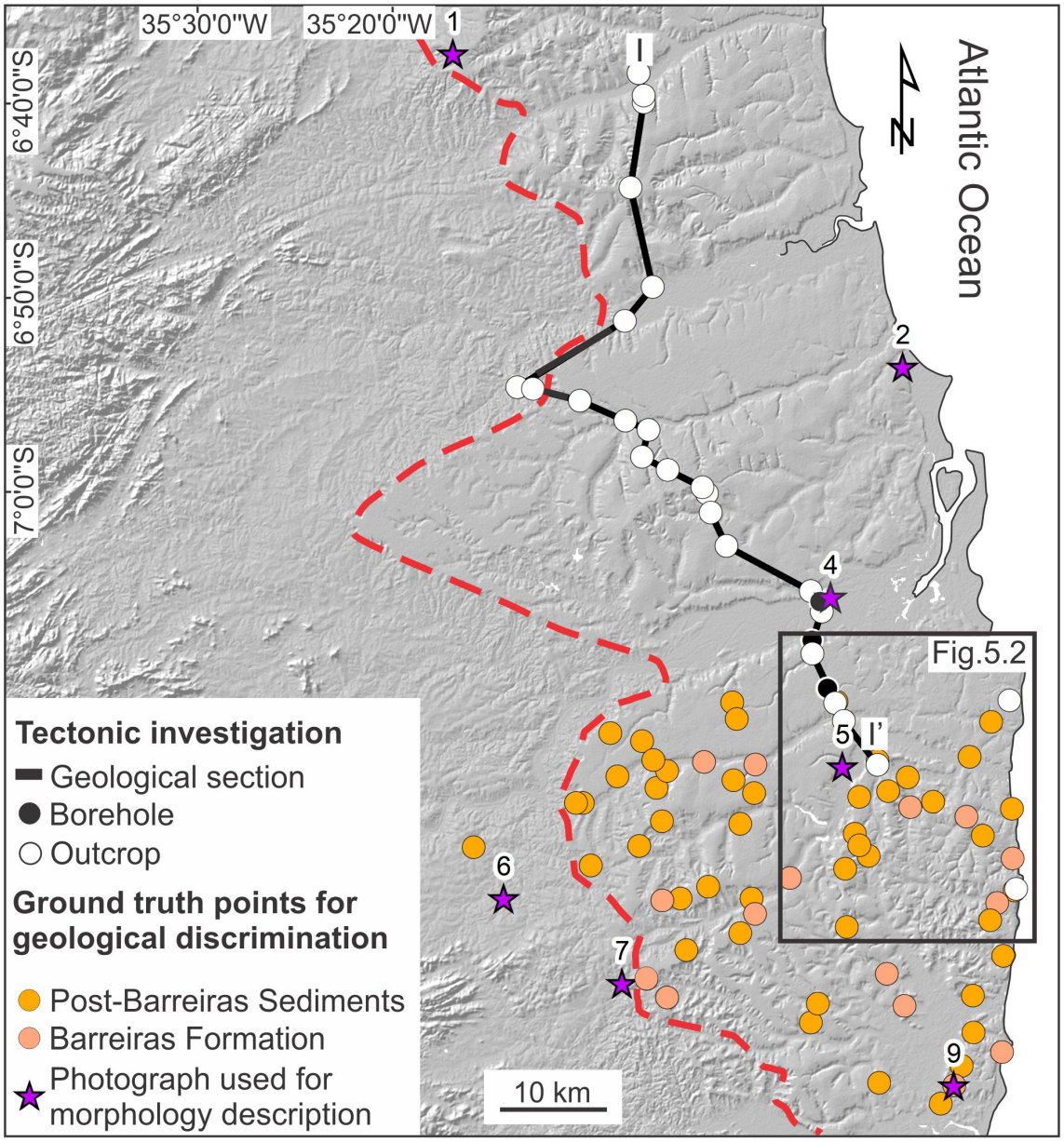

Dashed red line = general limit between the Precambrian basement rocks to the west and sedimentary deposits to the east. Shaded relief was derived from the SRTM-DEM.

SOURCE: Author's production.

5 RESULTS

5.1 Relief morphology

The six swath topographic profiles with widths of 5 km showed asymmetrical patterns along sedimentary terrains, with convex elevation curves around the dome-shaped reliefs, which occurred parallel to the coastline (see DR in Figure 5.1). The swath profiles 1 and 2 from the southern sector displayed closer elevation curves over the crystalline basement domain, with mean elevation values ranging from 45 to 200 m. These two profiles recorded increased elevations over a distance of $\sim$ 12 km of the sedimentary cover domain, with maximum altitudinal values up to 220 m. To the east, the region around the Gramame River, dominated by the Barreiras and Post-Barreiras Sediments (Figure 5.2a-b), shows recurved drainage networks and a succession of alternating high and low terrains with relatively similar altitudinal values (Figure 5.2c).

The first 8 km of the swath profile 3 in the northern sector of the study area (Figure 5.1) recorded mean elevation curves closer to maximum and minimum curves over the crystalline basement rocks, with mean elevation values up to 110 m. This profile recorded increased elevation up to 170 m to the east over the sedimentary terrain. Profile 4 in the central sector recorded a flat area to the west, with the relief progressively decreasing in altitude to the northeast over the Post-Barreiras Sediments and, secondarily, the crystalline basement rocks. At a distance of 25 km along this profile, the elevation curves changed abruptly, and is characterized by a sudden decline followed by a rapid increase, which suggests an ongoing river capture between the upper Miriri River and a tributary of the left margin of the Una River (Figure 5.1). Profile 4 had convex elevation curves around the prominent dome-shaped relief, where the Post-Barreiras Sediments stand at an altitude up to 230 m.

Figure 5.1 - Swath profiles that illustrate the topography of the study site.

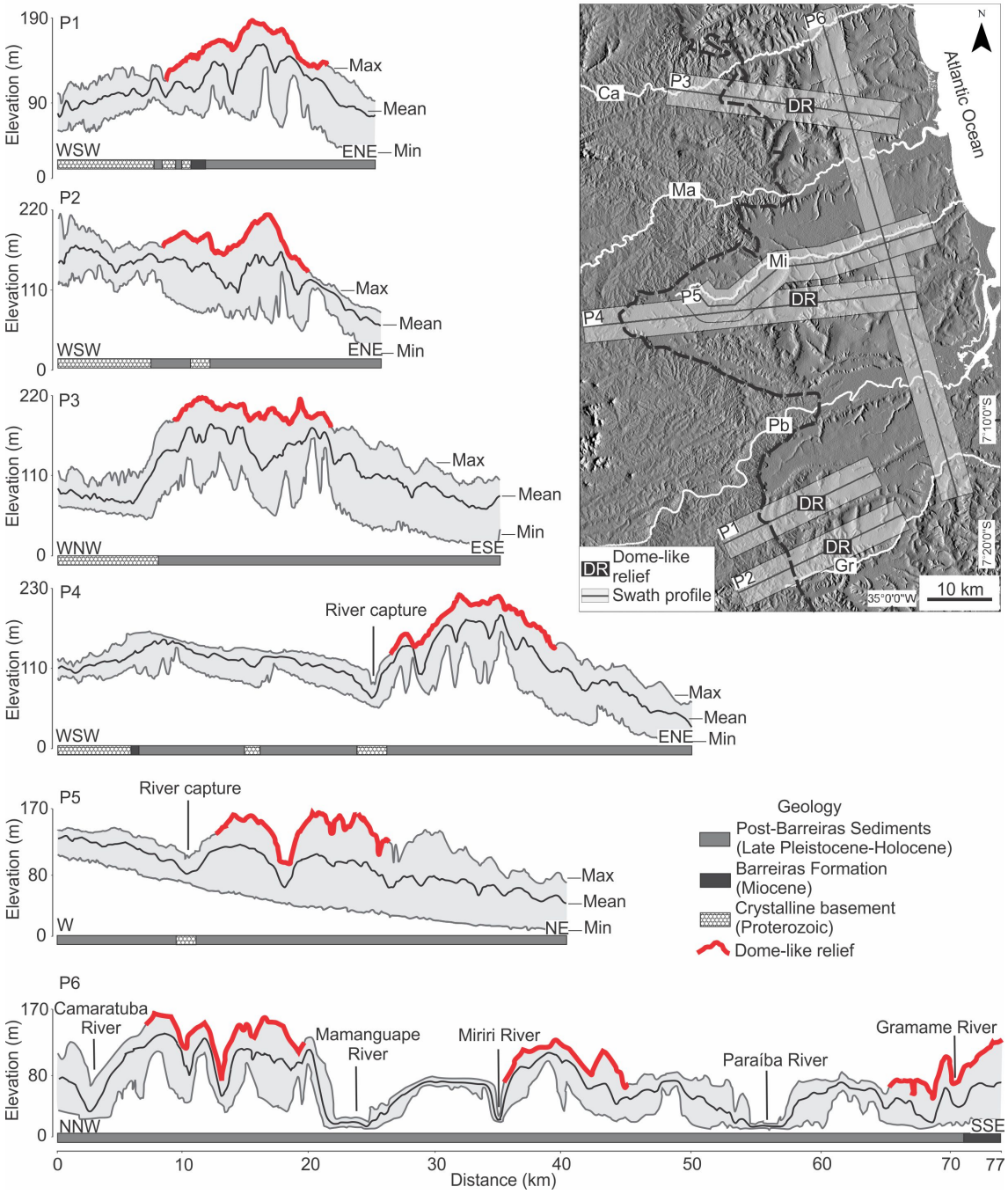

Swath profiles are based on the mean, maximum and minimum elevation curves derived from the 1 arc-second SRTM-DEM. See the location of swath profiles in the upper right side of the figure. Trunk streams: Ca = Camaratuba; Ma = Mamanguape; Mi = Miriri; Pb = Paraíba; Gr = Gramame. Hatched black line = limit between the Precambrian basement rocks to the west and sedimentary deposits to the east. The geological units are shown below each profile. The horizontal axis is the same for all profiles and is shown only below the P6 for simplification.

SOURCE: Author's production.

Figure 5.2 - Relief and geology in the region of the Gramame River.

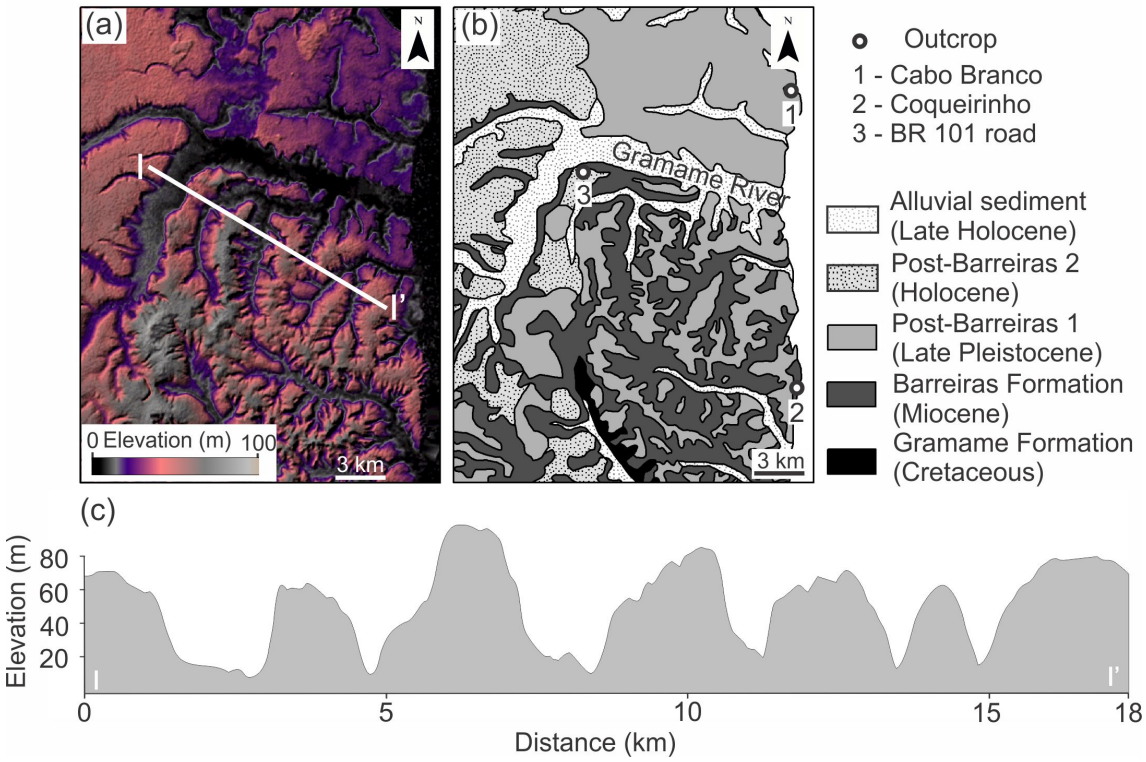

(a) SRTM-DEM illustrating the relief in the vicinity of the Gramame River (see location in Figure 4.2). (b) Corresponding geological map. (c) Transect illustrating the relief containing a succession of alternating high and low terrains (see transect I-I´ in a).

SOURCE: Author's production.

The swath profile 5 along the Miriri River showed closer elevation curves in the upper course over the Post-Barreiras Sediments, and no significant change in the base level of the tributaries (Figure 5.1). This profile showed a subtle change in elevation curves over the crystalline basement rocks at a distance of 10 km, which confirmed the ongoing river capture recorded in the profile 4. Along the middle and lower Miriri River, profile 5 showed an anomalous topographic pattern, with a marked increase in elevation over the sedimentary terrains around the dome-shaped relief. The maximum and mean elevation curves in this sector had a significant reduction in the base level of the entrenched tributaries concerning the upper Miriri River. The swath profile 6, parallel to the coast over the Post-Barreiras Sediments and Barreiras Formation, showed convex elevation curves around the dome-shaped reliefs. At a distance of 22 km in this profile, the morphology changed abruptly to closer elevation curves over the Mamanguape River valley. Furthermore, the profile 6

recorded convex elevation curves to the south, on the right margin of the Miriri River. The morphology of the relief changed abruptly along the Paraíba River valley, which records mean elevation curves closer to maximum and minimum curves. Towards the right margin of this river, the profile recorded increased elevation over the Post-Barreiras Sediments and Barreiras Formation terrains.

The interpretation of the *THi** index and relative relief data for the six 5 km wide swath profiles was hampered by frequent curves with peaks and troughs, even after the application of a mean moving window (Figure 5.3). Hence, *THi** values were higher in sedimentary areas than in terrain with crystalline basement rocks (grey curves in Figure 5.3). All swath profiles had significant changes in the relative relief curves (black curves in Figure 5.3). The relative relief values from the sedimentary areas were higher than in the crystalline basement rocks, with a significant increase in the values close to the dome-shaped reliefs. For instance, profile 5 along the Miriri River recorded an increase in the relative relief values over the Post-Barreiras Sediments, particularly around the dome-shaped relief, which suggests a high incision of the drainage network.

Figure 5.3 - *THi** index and relative relief curves derived from the 1 arc-second SRTM-DEM swath profiles (see location in Figure 5.1).

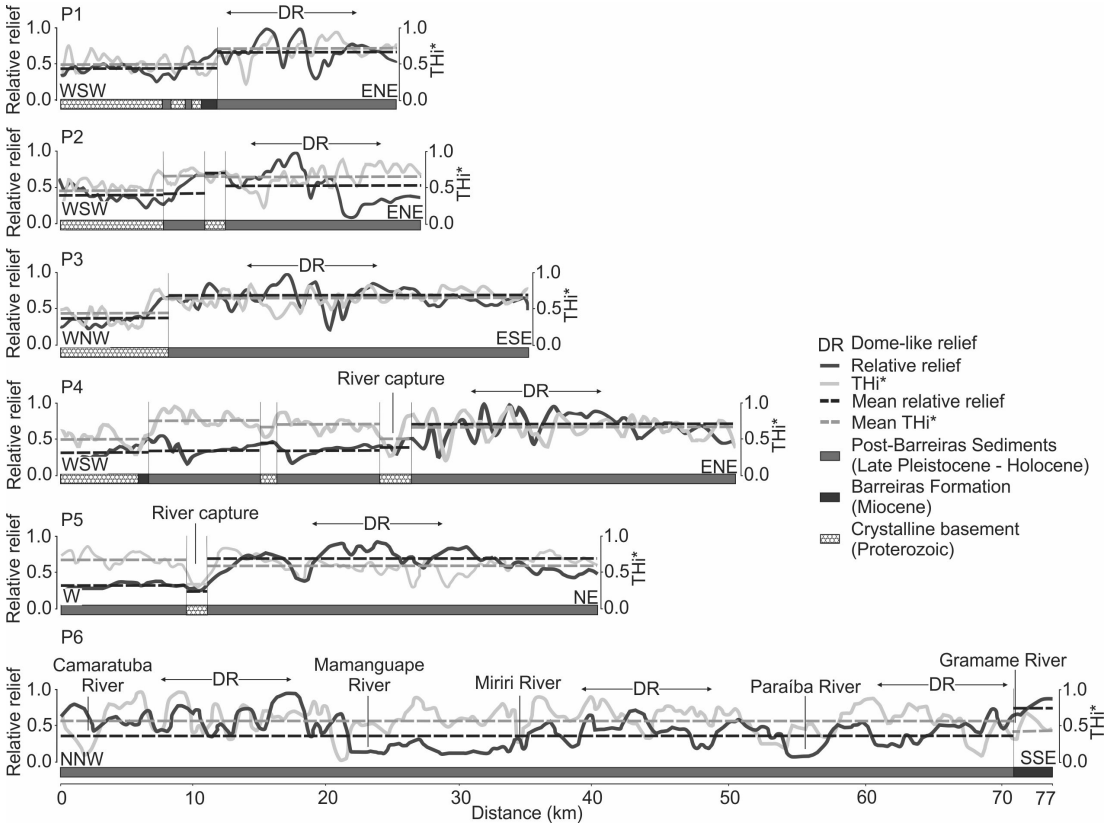

The geological units are shown below each profile. Relative relief values were normalized between 0 and 1 for comparison. The horizontal axis is the same for all profiles and is shown only below the P6 for simplification.

SOURCE: Author's production.

5.2 Morphology of the drainage network and basin asymmetry

The drainage network in the northern sector of the study area (Figure 5.4; Table 5.1) occurred over Precambrian basement rocks to the west and Post-Barreiras Sediments to the east (Figure 5.3). Alluvial sediments were verified mainly along the Camaratuba and Mamanguape river valleys (Figure 3.3). The main sub-basins in the northern sector were the Barro Branco, Jacaré, Estiva, Tinto, Caiana, Pitombeira, Seco, and upper Camaratuba rivers. Rectilinear or slightly curved rivers, such as the Barro Branco, Jacaré, Estiva, Tinto, and Caiana (Figure 5.4b), were recorded over young (Late Pleistocene-Holocene) sedimentary terrains of the Post-Barreiras Sediments. In general, small rectilinear channels are connected at right angles with

the main channels, characterizing trellis to sub-dendritic drainage patterns. In contrast, rivers that flow over the Precambrian basement rocks, such as the Pitombeira, Seco, and upper Camaratuba, have tributaries with angular connection with smaller rivers, which characterizes dendritic to sub-dendritic drainage patterns.

Figure 5.4 - Characterization of the relief and drainage network of the study area.

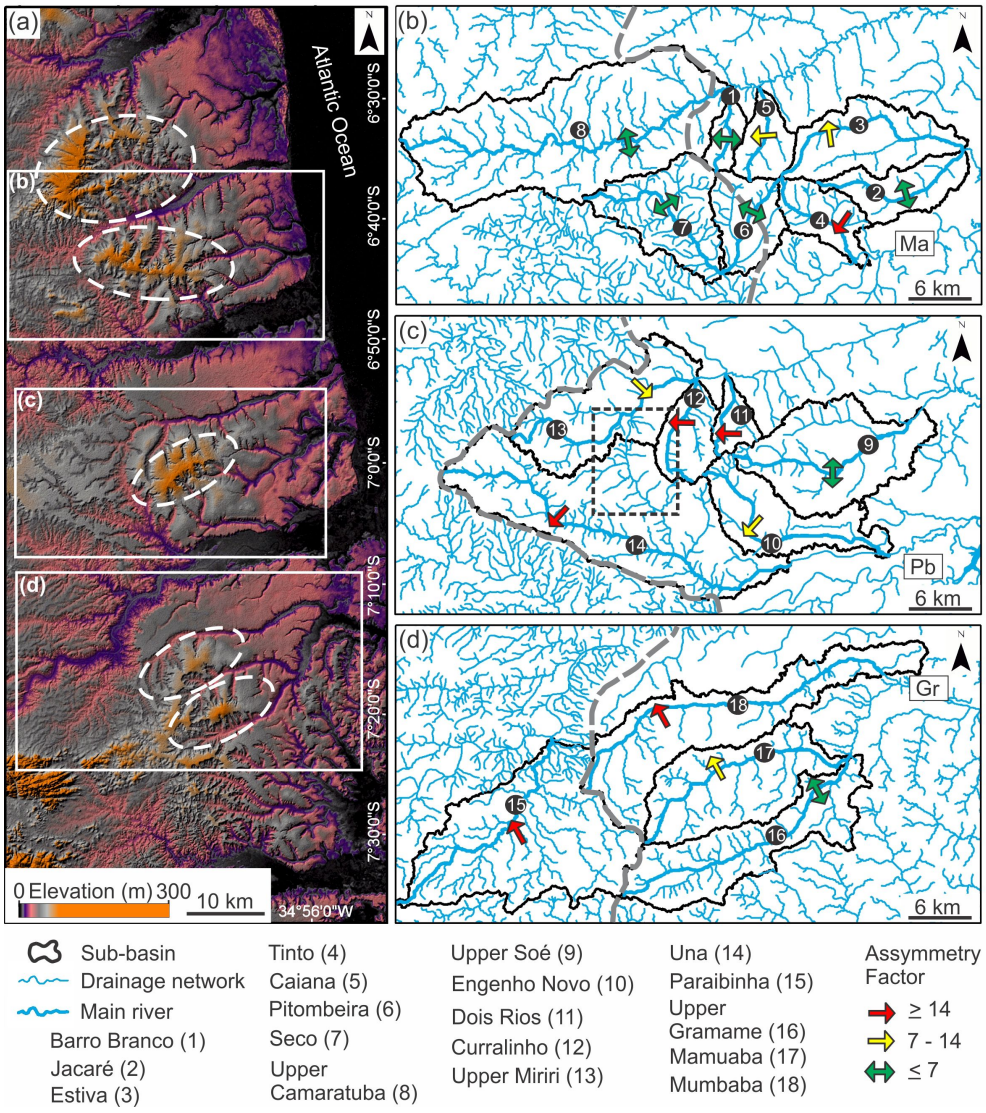

(a) Dome-shaped reliefs (dashed ellipses) viewed in a SRTM-DEM, customized using a color palette. (b-d) Detail of the drainage network and sub-basins, including the main rivers and AF index extracted from the SRTM data (dashed black box = strong curved tributaries). Trunk stream: Ma = Mamanguape; Pb = Paraíba; Gr = Gramame. Grey dashed line = geological boundaries between basement rocks (west) and sedimentary deposits (east).

SOURCE: Author's production.

Table 5.1 - Characteristics of the studied rivers and sub-basins, including geomorphic indices, dominant geology and drainage pattern.

River name / (ID)	Length (km)	Area of sub-basin (km^2)	AF	Tilting direction	H_{max}	E_q	Dominant geology	Drainage pattern
Barro Branco (1)	10	18	1	E	0.29	0.18	Sd	Trellis to sub-dendritic
Jacaré (2)	17	51	4	S	0.45	0.29	Sd	
Estiva (3)	23	87	14	N	0.39	0.36	Sd	
Tinto (4)	13	42	17	SW	0.52	0.25	Sd	
Caiana (5)	11	33	10	W	0.53	0.15	Sd	
Pitombeira (6)	12	52	6	E	0.4	0.23	Cb	Dendritic to sub-dendritic
Seco (7)	20	88	5	NE	0.18	0.31	Cb	
Upper Camaratuba (8)	43	293	4	S	0.61	0.08	Cb	
Upper Soé (9)	21	132	2	S	0.53	0.27	Sd	Radial to recurved trellis
Engenho Novo (10)	25	82	11	SW	0.54	0.14	Sd	
Dois Rios (11)	9	20	25	W	0.21	0.35	Sd	
Curralinho (12)	13	41	21	W	0.38	0.21	Sd	
Upper Miriri (13)	25	119	10	SE	0.17	0.09	Sd	
Una (14)	43	254	18	SW	0.25	0.13	Sd	Sub-dendritic to trellis
Paraibinha (15)	29	220	26	NW	0.56	0.14	Cb	Dendritic to sub-dendritic
Upper Gramame (16)	29	127	7	NW	0.4	0.28	Sd	Recurved trellis to trellis
Mamuaba (17)	26	127	12	NW	0.44	0.28	Sd	
Mumbaba (18)	38	169	17	NW	0.27	0.15	Sd	

Cb = Crystalline basement; Sd = Sedimentary deposits

SOURCE: Author's production.

The central sector of the study area (Figure 5.4c) is drained by the Miriri and Paraíba basins, which flow mainly over the Post-Barreiras Sediments (Figure 3.3). The main sub-basins were the upper Soé, Engenho Novo, Dois Rios, Curralinho, upper Miriri, and Una rivers. The upper Soé, Engenho Novo, Dois Rios, Curralinho, and upper Miriri rivers have marked curvatures, characterizing radial to recurved trellis drainage patterns around a elliptical-shaped dome morphology (see dashed white lines in Figure 5.4c). The Una River has tributaries connected either at the right or obtuse angles to form trellis to sub-dendritic drainage patterns. Sharp curves were recorded between the upper Miriri River and a tributary from the left margin of the Una River (hatched black box in Figure 5.4c).

The southern sector of the study area (Figure 5.4d) has rivers that flow over the Barreiras Formation and Post-Barreiras Sediments and, less frequently, Precambrian basement rocks (Figure 5.3). The main rivers over the Miocene and Late Pleistocene-Holocene deposits belong to the upper Gramame, Mamuaba, and Mumbaba sub-basins. These rivers have either rectilinear or curved segments and tributaries connected to small channels at right angles, forming recurved trellis to trellis patterns. In contrast, the Paraibinha River, which flows over the Precambrian basement rocks, has a drainage network with a large number of channels and varied confluence angles, typifying dendritic to sub-dendritic patterns.

The results of the AF index ranged from 1 to 26 (Table 5.1 and Figure 5.4b-d). The asymmetric sub-basins with high AF index were located in the central and southern sectors, consisting of: Paraibinha ($AF = 26$), Dois Rios ($AF = 25$), Curralinho ($AF = 21$), Una ($AF = 18$), Mumbaba ($AF = 17$), and Tinto ($AF = 17$). These sub-basins had sectors tilted to NW, SW, and W in areas dominated by the Post-Barreiras Sediments and, secondarily, Precambrian basement rocks. Moderate AF indices were from the Estiva ($AF = 14$), Mamuaba ($AF = 12$), Engenho Novo ($AF = 11$), Caiana ($AF = 10$), and upper Miriri ($AF = 10$) river sub-basins, in the northern and central sectors. Symmetric or quasi-symmetric sub-basins with low AF values were recorded in the upper Gramame ($AF = 7$), Pitombeira ($AF = 6$), Seco ($AF = 5$), upper Camaratuba ($AF = 4$), Jacaré ($AF = 4$), upper Soé ($AF = 2$), and Barro Branco ($AF = 1$) sub-basins, located mainly in the northern sector. There was no evidence that these sub-basins were affected by the regional tilting.

5.3 Description of normalized river long profiles

The eighteen normalized river profiles revealed H_{max} between 0.17 and 0.61 and E_q between 0.08 and 0.36 (Table 5.1). The cluster analysis based on H_{max} allowed the

interpretation of three groups of rivers with similar shapes, namely: (i) anomalous rivers with near linear longitudinal profiles (G1); (ii) rivers with almost concave longitudinal profiles (G2); and (iii) rivers with well-defined concave longitudinal profiles (G3) (Figure 5.5a-d).

Figure 5.5 - Normalized river profiles of the study area.

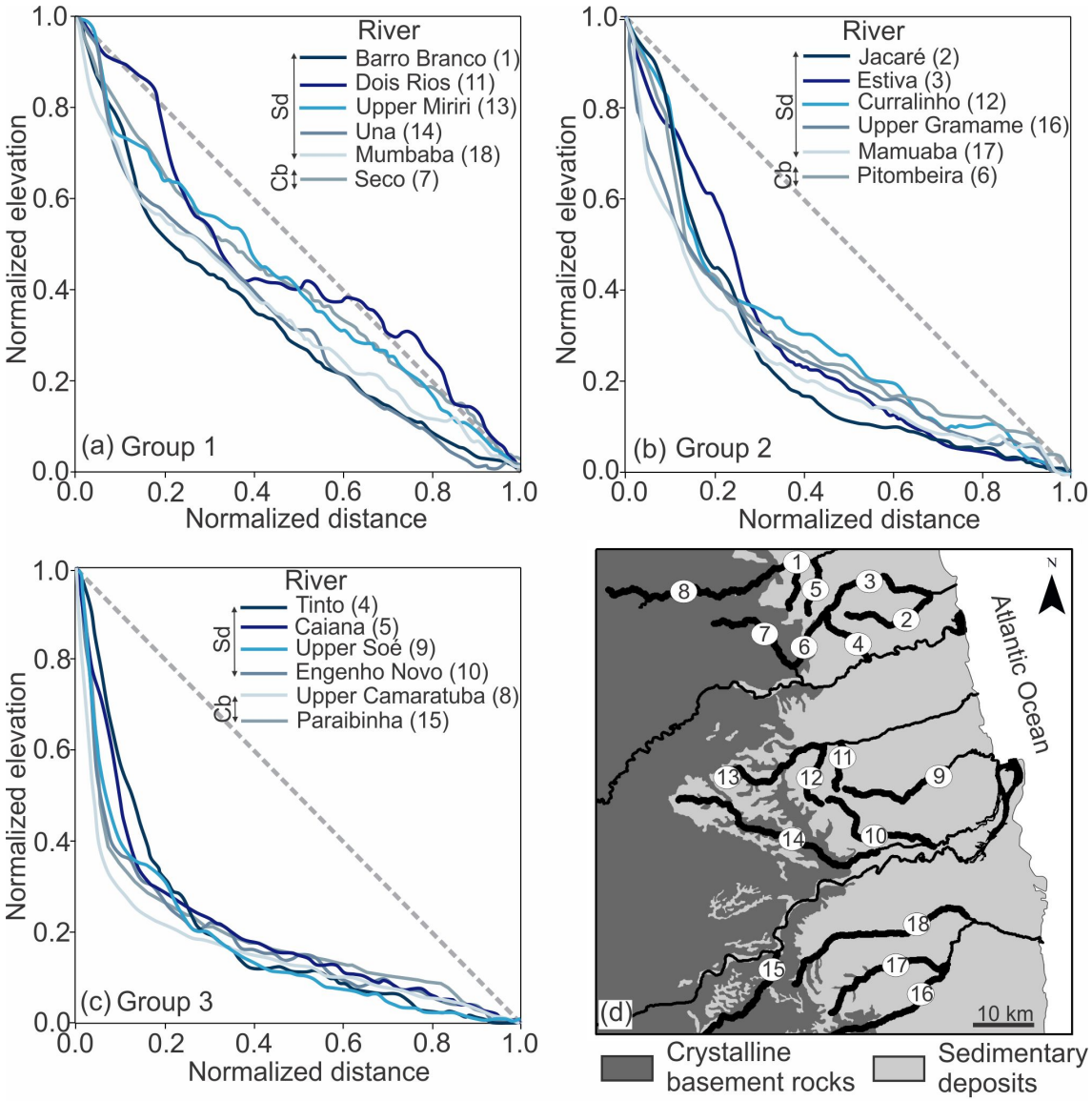

(a-c) Normalized river long profiles classified into three main groups by cluster analysis. Sd = Sedimentary deposits; Cb = Crystalline basement rocks. (d) Main rivers (1-18) of the study area (see figures a-c for river identification).

SOURCE: Geological map in d simplified from Rossetti et al. (2012).

The first group was characterized by rivers with anomalous curves (Barro Branco, Seco, Dois Rios, upper Miriri, Una, and Mumbaba rivers), suggesting linear shapes, with H_{max} between 0.17 and 0.29 and E_q between 0.09 and 0.35 (Figure 5.5a and Table 5.1). The second group was composed by the Jacaré, Estiva, Pitombeira, Curralinho, upper Gramame, and Mamuaba rivers. This group included profiles with semi-concave shapes, H_{max} between 0.38 and 0.45 and E_q between 0.21 and 0.36 (Figure 5.5b and Table 5.1). Although the Barro Branco River was included in group 1, its profile was more compatible with the rivers of group 2. Similarly, the Curralinho River in this group showed the profile more compatible with the rivers in group 1. The third group (Tinto, Caiana, upper Camaratuba, upper Soé, Engenho Novo, and Paraibinha rivers) recorded longitudinal profiles with more concave shapes, H_{max} between 0.52 and 0.61 and E_q values between 0.08 and 0.27 (Figure 5.5c and Table 5.1). The comparative analysis between the H_{max} and E_q for the three groups of rivers revealed a negative linear correlation only for group 3 (r^2 coefficient = 0.60).

A comparison between the values of H_{max} and AF index was performed in order to identify spatial patterns in rivers flowing over different geological terrains (Figure 5.6). This analysis showed that rivers with low H_{max} values and high AF index values (asymmetric river basins), predominated over sedimentary terrains (e.g., Dois Rios -11, Curralinho -12, Una -14 and Mumbaba -18).

Figure 5.6 - Scatter plot with H_{max} versus AF index for a set of eighteen rivers of northern Paraíba Basin (see river names in Table 5.1).

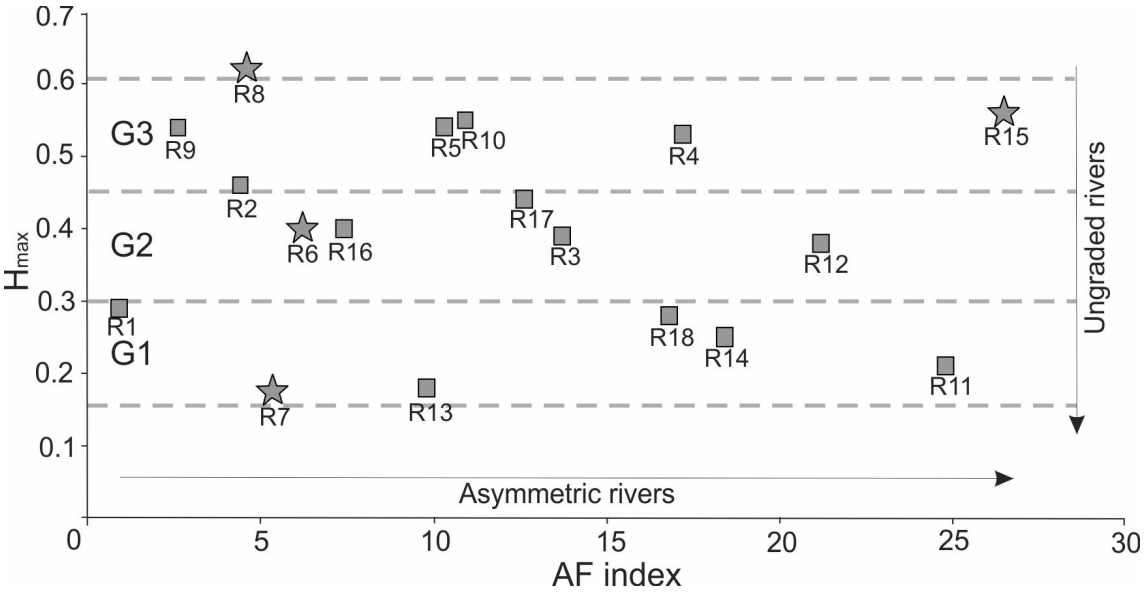

G1-G3 = groups of normalized river profiles; star = river over crystalline basement rocks; square = river over sedimentary deposits.

SOURCE: Author's production.

5.4 Geological data

The 110 km-long, N to SE-oriented geological section analyzed in this study revealed several substantial topographic and stratigraphic variations (Figure 5.7a). This section also recorded two slightly arched convex-up morphologies of the geological units between the Camaratuba and Mamanguape river valleys, as well as between the Miriri and Paraíba river valleys. Such elevated surfaces were quite compatible with the dome-shaped morphologies detected by the morphological analysis. The Proterozoic crystalline rocks were recorded at altitudes of up to 70 m in the first 5 km to the north, where these rocks were overlain by the Barreiras Formation and a thin package of the Post-Barreiras Sediments. However, the top of the Proterozoic basement rocks occurred at altitudes as low as 30 m in the Camaratuba River valley, where the Post-Barreiras Sediments increased in thickness. The top of the Post-Barreiras Sediments and the underlying rocks on the right bank of the Camaratuba River valley were recorded at higher altitudes (i.e., above the 60 m). The Barreiras Formation on the left bank of the Mamanguape River occurred at altitudes below 60 m. The

Mamanguape and Miriri valleys recorded crystalline basement rocks overlain by a thin package of the Barreiras Formation and, secondly, Post-Barreiras Sediments. At a distance of 55 km along the geological section, Proterozoic crystalline rocks occurred at altitudes up to 100 m, but lower altitudes, of 40 m, were also recorded between the Miriri and Paraíba valleys. The thicknesses of the Barreiras Formation increased considerably on both sides of the Paraíba valley, followed by an offset of several tens of meters. A thick package of carbonates from the Gramame Formation underlies the Barreiras Formation in the southern margin of the Paraíba River. The Barreiras Formation unconformably overlies Precambrian crystalline rocks on the left margin of the Paraíba River.

The interpretation of a few geological exposures along road cuts and coastal cliffs revealed that the Barreiras Formation and, secondly, the Post-Barreiras Sediments were locally folded, with the deformation expressed on the relief (Figures 5.7b-c, 5.8, and 5.9). Broad anticlines and synclines from medium to large amplitudes, with mostly E-W-striking sub-horizontal axes were present. The folded strata included fine to medium-grained sandstones and mudstones of Miocene age, belonging to the Barreiras Formation (Figures 5.7b-c and 5.8). Although in most geological exposures the overlying Late Pleistocene deposits were horizontally bedded, they were also folded in parts of the Paraíba coast (Figures 5.8b-c and 5.9).

Figure 5.7 - Regional stratigraphic correlation and fold in a road-cut outcrop (BR 101 road).

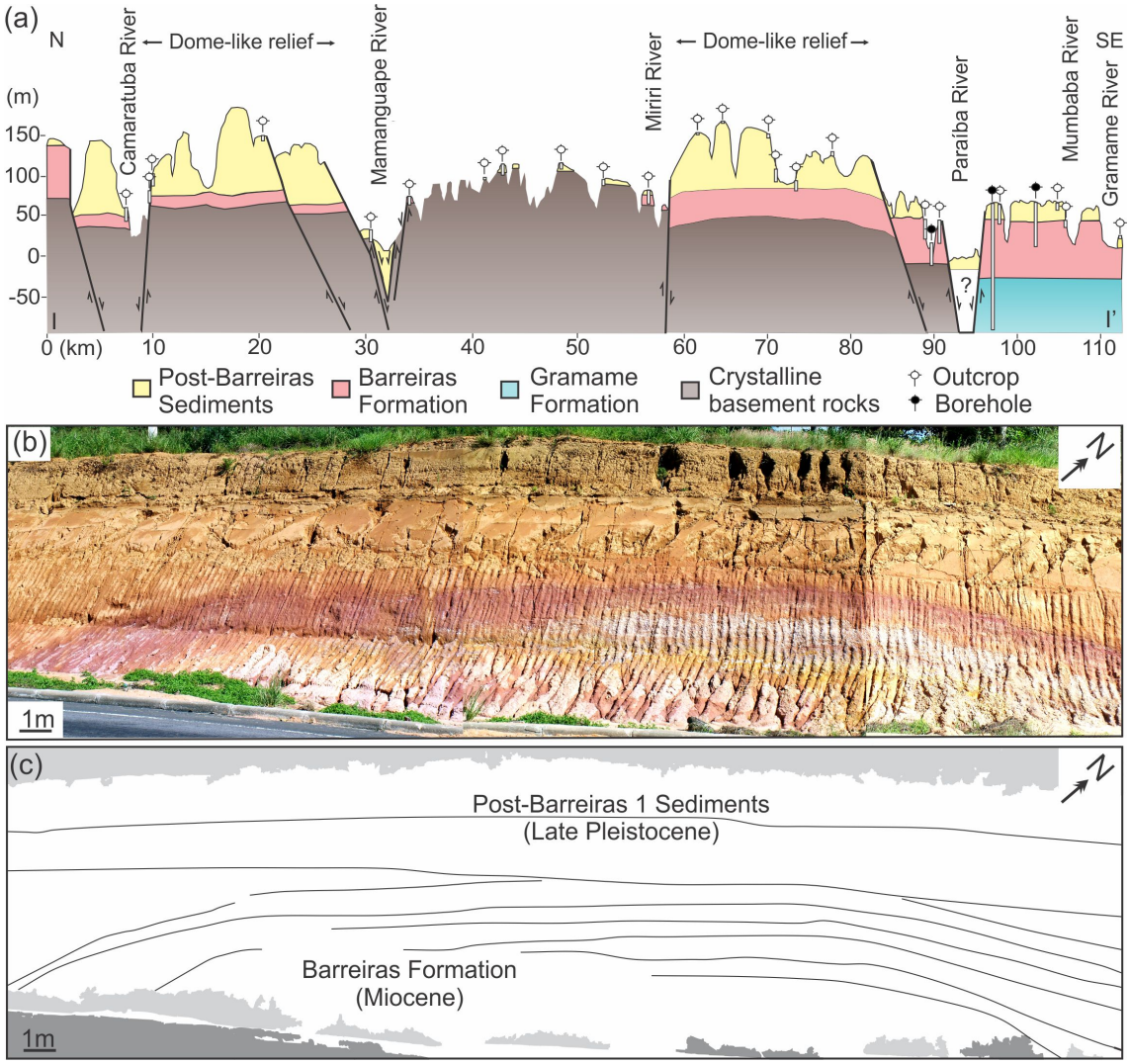

(a) The geological section was built by integrating surface and subsurface data (see location in Figure 4.2). (b-c) Folds of the Barreiras Formation (b) with corresponding line drawing (c) (see location of outcrop 3 in Figure 5.2b). Note that the overlying Post-Barreiras 1 Sediments were unfolded in this location.

SOURCE: Geological section modified from Rossetti et al. (2012).

Figure 5.8 - Folds in outcrops of the Barreiras Formation and Post-Barreiras Sediments in the Coqueirinho coastal cliff.

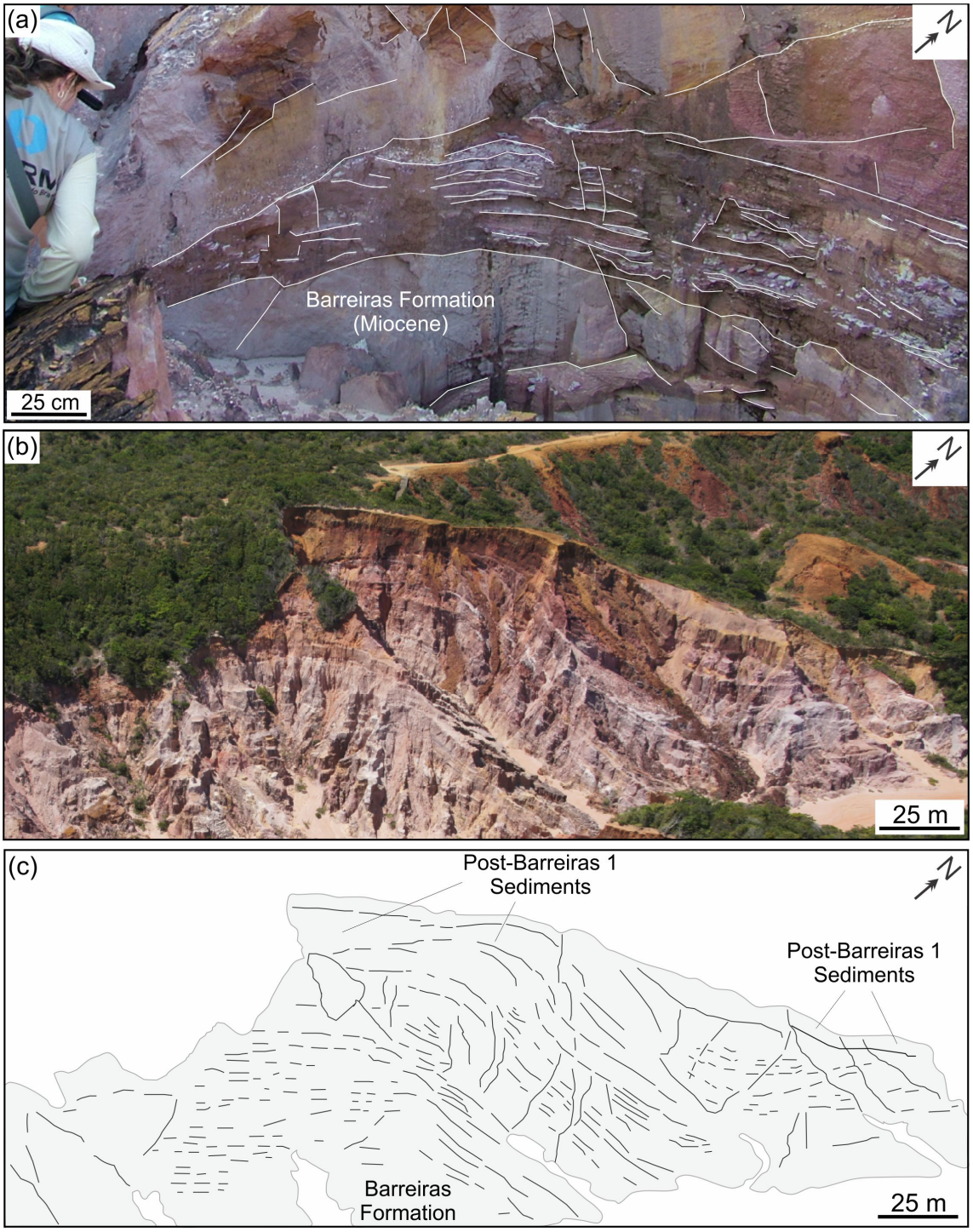

(a) Folded strata (see location of outcrop 2 in Figure 5.2b). (b-c) Aerial photograph illustrating the folded relief shown in (b), with the corresponding line drawing (c).

SOURCE: Author's production.

Figure 5.9 - Folds in outcrops of the Barreiras Formation and Post-Barreiras Sediments in the Cabo Branco coastal cliff.

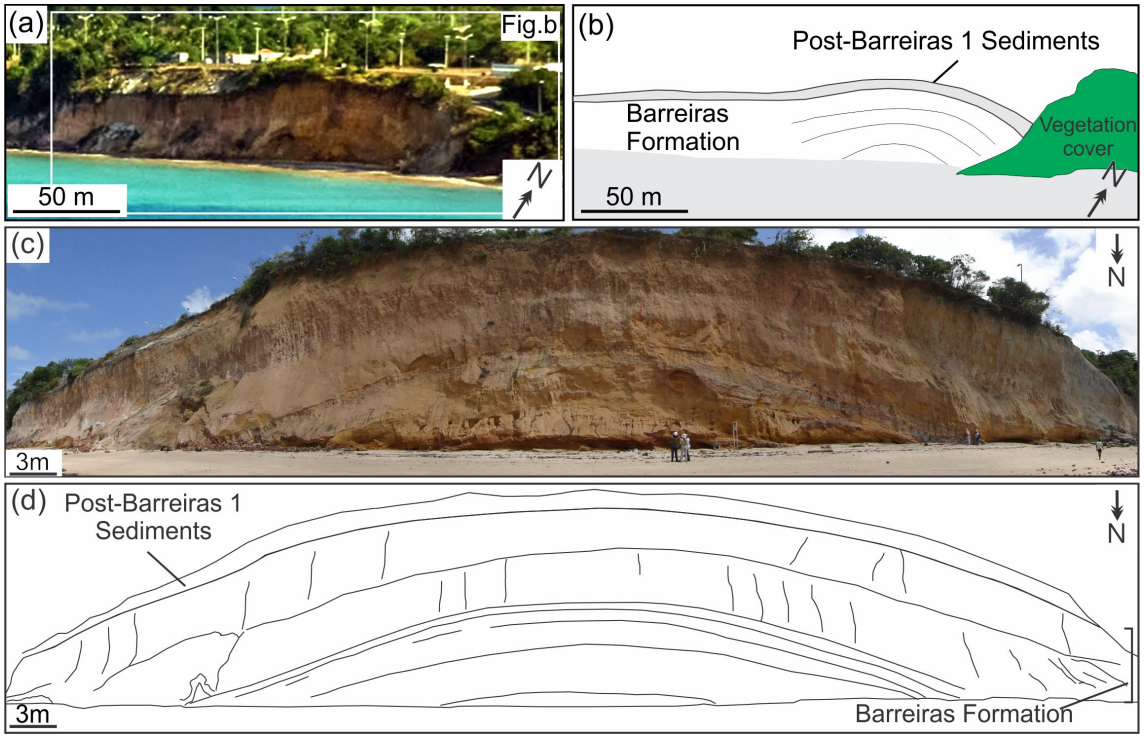

(a-b) The folded relief of the Cabo Branco coastal cliff (a), with the corresponding line drawing (b) (see location of outcrop 1 in Figure 5.2b). (c-d) Close-up view of the cliff exposure, illustrating the folded Barreiras and Post-Barreiras 1 Sediments (c), with the corresponding line drawing (d).

SOURCE: Author's production.

5.5 Morphostructural lineaments, river long profiles, knickpoints, and normalized channel steepness index (k_{sn})

The study area showed a significant amount of morphostructural lineaments (Figure 5.10), mainly on areas dominated by Precambrian basement rocks to the west, and secondarily, on sedimentary deposits of the Paraíba Basin to the east. NE-SW and E-W striking structures are the two major trends verified in this area and are compatible with the main set of structures over the northeastern Brazil (BRITO-NEVES et al., 2004; BEZERRA et al., 2008; BEZERRA et al., 2014; LIMA et al., 2017).

Figure 5.10 - Morphostructural lineaments of the study area, including the limits of the sedimentary basin and Precambrian basement, trunk streams and tributaries, the latter numbered to facilitate the descriptions presented in the text.

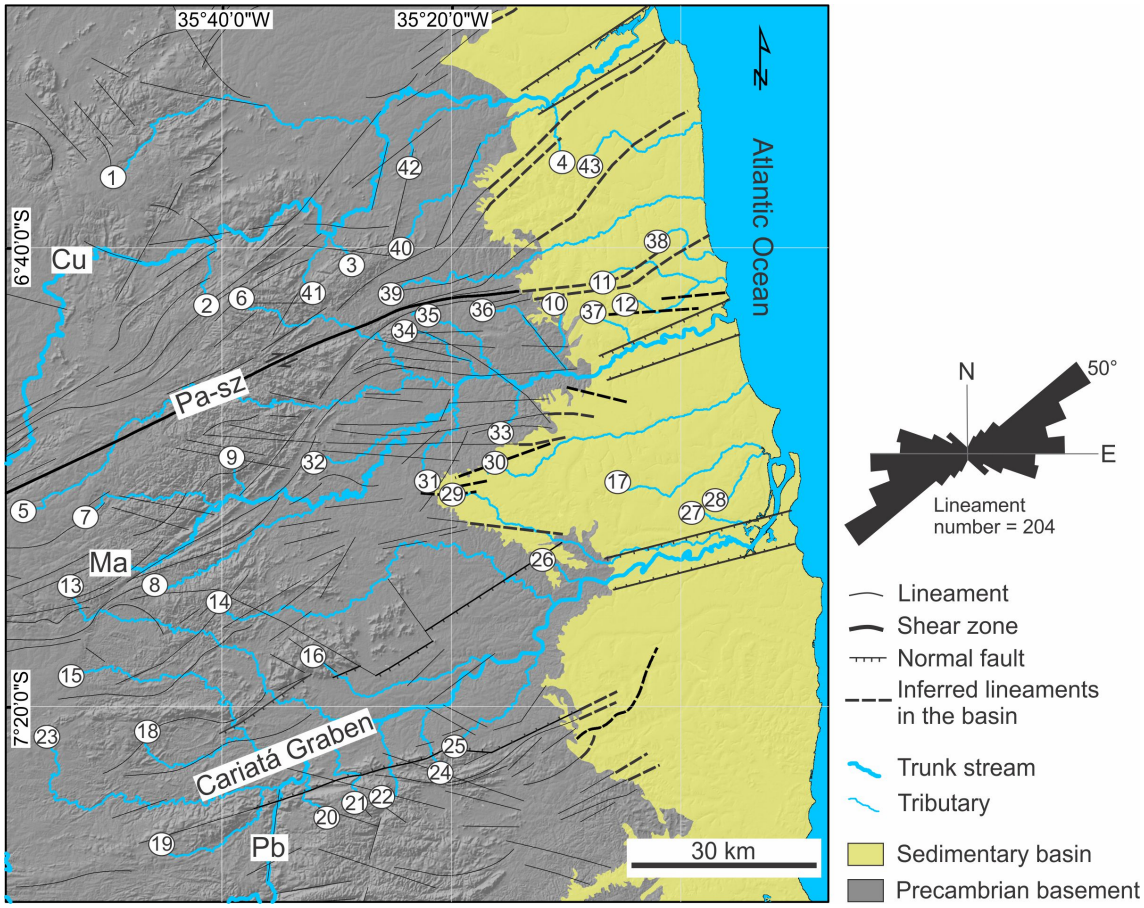

Pa-sz = Patos shear zone. Trunk streams: Cu = Curimataú; Ma = Mamanguape; Pb = Paraíba River. Geological compartments simplified from the geological map at 1:1000000 scale from CPRM (http://geosgb.cprm.gov.br/geosgb). Shear zone and graben-related normal faults simplified from Brito-Neves et al. (2004), Bezerra et al. (2008), Bezerra et al. (2014), and Lima et al. (2017).

SOURCE: Brito-Neves et al. (2004), Bezerra et al. (2008), Bezerra et al. (2014), and Lima et al. (2017).

Many tributaries with elevation values up to 450 m did not show knickpoints, as they recorded slightly concave-up and linear river profiles in distance-elevation and χ-elevation plots, respectively (Figure 5.11). Some small tributaries located over flatter terrains, capped by Miocene deposits in the southern sector of the study site,

showed convex river profiles suggestive of knickpoints (rivers 26, 27, 28, and 29 in Figure 5.11f). However, as these tributaries did not show clear breaks or spikes in log-log slope-area plots, they were included in the group of rivers without knickpoints.

Figure 5.11 - River profiles from tributaries without knickpoints.

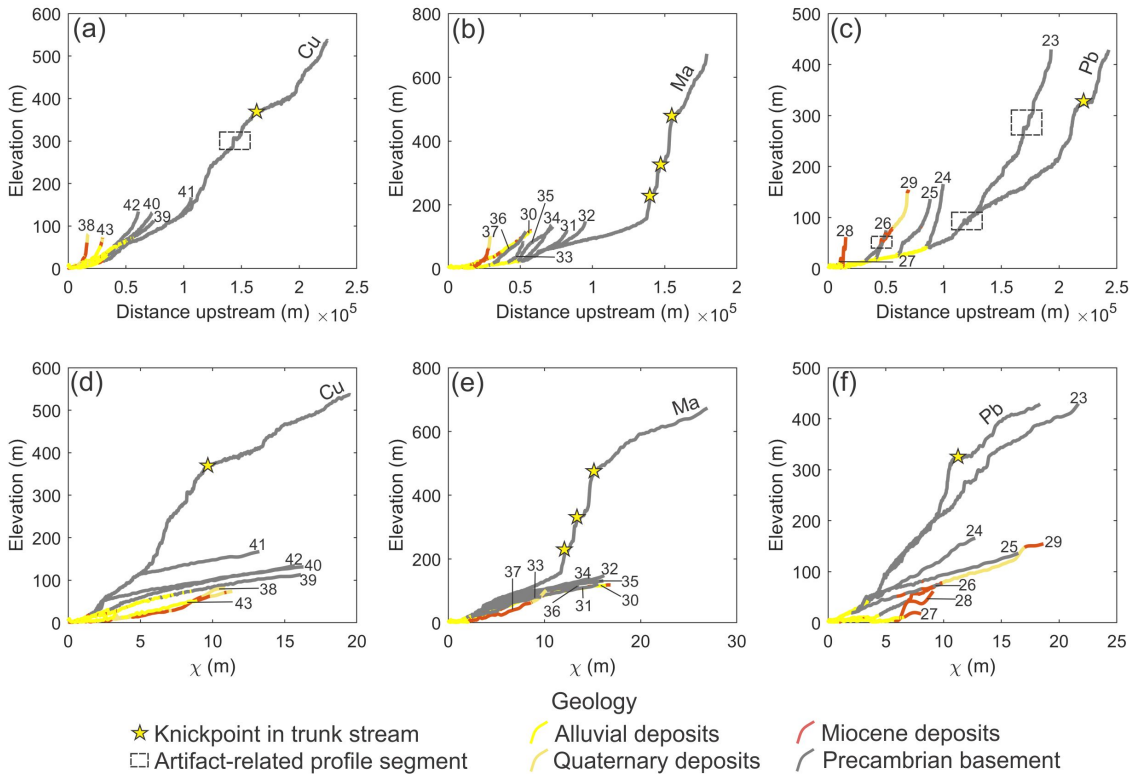

Distance-elevation (a-c) and χ-elevation (d-f) plots for the tributaries with river profiles without apparent knickpoints (see the location of the numbered rivers in Figure 5.10). Trunk streams with knickpoints are also indicated for comparison. Trunk streams: Cu = Curimataú; Ma = Mamanguape; Pb = Paraiba. River profiles were colored by their corresponding geology. River profile segments related to artifacts (lakes/reservoirs) are shown only in the distance-elevation graphs for the sake of simplification.

SOURCE: Author's production.

A considerable number of tributaries were classified here as having knickpoints (Figure 5.12). The major trunk streams also showed some segments bounded by major knickpoints, but they were not investigated here, as the focus was to analyze the river response to base level changes in the tributaries. From a total of forty-three tributaries, twelve showed knickpoints classified as having a vertical-step end-member

morphology (green dots in Figure 5.12a-f), represented by spikes in the slope values of the log-log slope-area plots (Figure 5.12g-i). Most of these tributaries are located over Precambrian basement rocks, followed by Miocene-Quaternary deposits, with elevation values ranging between 73 and 507 m asl (Table 5.2). Some vertical-step knickpoints were identified: at or close to geological boundaries (see, for instance, the location of knickpoints from rivers 1 and 2 in Figure 5.13a); downstream of slope-break knickpoints; and in overstepped channel segments (e.g., profiles 1, 5, 6, 9, and 20 in Figure 5.12d-f) with maximum k_{sn} values at knickpoint almost twice as high as the slope-break knickpoints (Table 5.2). For instance, vertical-step knickpoints showed an average k_{sn} at knickpoint of 38.5 and a maximum k_{sn} value of 85.3, while slope-break knickpoints displayed an average k_{sn} at knickpoint of 27.4 and a maximum k_{sn} value of 49.3 (Table 5.2). In addition, some of the vertical-step knickpoints may be related with local variations in rock properties or landslides, such as the knickpoints located at higher topographic levels around the dome-like reliefs (e.g., knickpoints from rivers 17 and 12 in Figure 5.13a). Many river profile segments with vertical-step knickpoints showed a more significant increase in k_{sn} downstream than upstream in the river profiles. These knickpoints, which could be confused with the slope-break end-member morphology, are probably related to lithological contrasts.

Figure 5.12 - River profiles from tributaries with knickpoints.

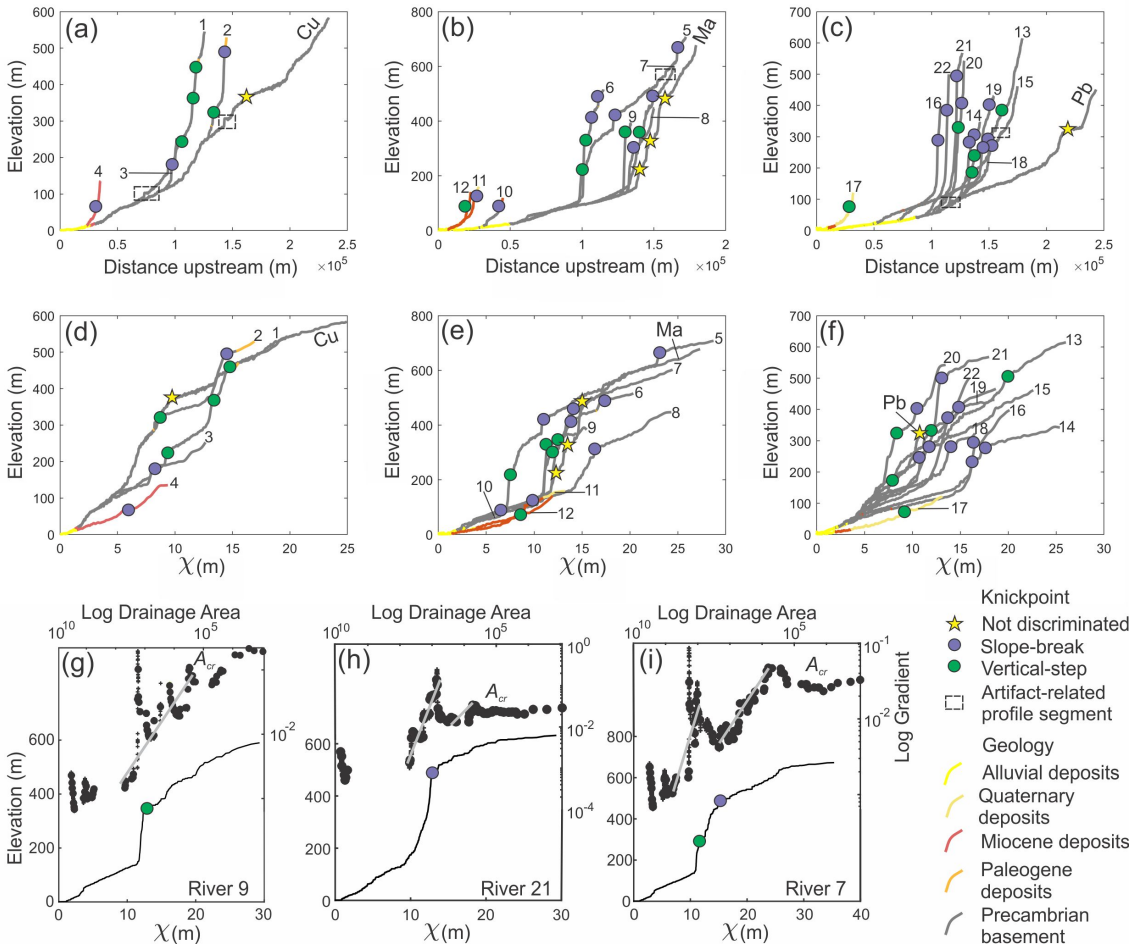

River profiles in distance-elevation (a-c) and χ-elevation (d-f) plots, with the location of slope-break and vertical-step knickpoints (see the location of the numbered rivers in Figure 5.10). Trunk streams: Cu = Curimataú; Ma = Mamanguape; Pb = Paraíba. River profile segments related to artifacts (lakes/reservoirs) are shown only in distance-elevation plots for simplification. River profiles were colored by their corresponding geology. (g-h-i) Log-log slope-area and χ-plots showing examples of stretches separated by vertical-step (g), slope-break (h), and both (i). Black dots in g-h-i = log-log slope-area data; A_{cr} = critical drainage area.

SOURCE: Author's production.

A total of eighteen rivers showed profiles with slope-break knickpoints (purple dots in Figure 5.12a-f). Most rivers recorded one knickpoint each, but three of them (rivers 5, 6, and 14) recorded 2 slope-break knickpoints. Knickpoints from the river 14 seem to be part of a single knickpoint, as they have similar morphology and are

located close to each other. These knickpoints occurred mostly over Precambrian basement rocks to the west, and secondarily, Miocene deposits to the east (Figures 3.2 and 5.13a). They showed a range of elevation values (65-676 m asl) and channels with downstream segments steeper than upstream channels especially those located in both margins of the Cariatá Graben over the Precambrian basement (see, for instance, k_{sn} ratio in Table 5.2 and Figure 5.10 for graben location). Most slope-break knickpoints are not clearly related to significant lithological contrasts, but some of them occurred closer to geological boundaries (e.g., knickpoints from rivers 2 and 10 in Figure 5.13a). However, it is important to note that only the present-day position of knickpoints is recorded and slope-break knickpoints are commonly interpreted to be mobile over time (WHIPPLE et al., 2013; BOULTON et al., 2014).

Table 5.2 - Summary of the main characteristics of the tributaries with knickpoints (slope-break and vertical-step), including vertical and horizontal components of knickpoint retreat, normalized channel steepness index (K_{sn}) and incision.

River number	River length (km)	Drainage area (km²)	Elev (m)	Dfm (km)	Dfd (km)	Area up (km²)	Area down (km²)	K_{sn} up ($m^{0.9}$)	±	K_{sn} down ($m^{0.9}$)	±	K_{sn} at kp ($m^{0.9}$)	K_{sn} ratio	Incision (m)
Slope-break knickpoint														
2	16.0	70.6	490	14.2	3.4	4.2	66.4	13.7	0.5	92.3	2.7	12.3	6.7	135
3	9.9	30.7	183	5.0	5.7	7.3	23.4	13.2	0.8	80.2	4.1	13.8	6.1	45
4	13.7	46.5	65	10.0	5.4	9.4	37.1	4.8	1.7	24.6	1.2	12.6	5.1	20
5	117.4	950.6	676	112.0	7.5	9.5	941.1	6.7	0.1	18.2	0.1	24.7	2.7	100
5	117.4	950.6	423	68.6	51.0	238.3	712.3	18.2	0.1	163.6	16.3	28.3	9.0	60
6	48.8	319.4	483	45.7	5.7	7.4	312.0	7.8	0.3	17.0	0.9	19.2	2.2	370
6	48.8	319.4	419	40.8	10.5	17.3	302.1	17.0	0.9	36.5	1.7	41.2	2.1	270
7	33.9	198.9	484	20.6	16.5	51.6	147.3	12.2	0.1	61.9	1.5	31.4	5.1	180
8	43.2	200.1	291	32.2	13.4	34.8	165.3	17.6	0.3	58.6	0.7	49.2	3.3	110
10	16.0	53.3	91	8.2	4.7	8.8	44.5	7.1	0.4	58.9	4.1	9.9	8.3	50
11	28.8	92.0	125	25.6	5.2	5.2	86.8	12.4	0.7	27.7	2.3	10.4	2.2	60
13	77.9	422.3	250	42.6	37.4	125.3	297.0	24.6	0.2	174.3	7.5	35.3	7.1	75
14	94.0	993.8	281	86.8	9.7	14.7	979.1	7.6	0.1	45.4	1.4	28.7	5.9	112
14	94.0	993.8	239	84.8	11.7	18.7	975.1	7.6	0.1	45.4	1.4	22.6	5.9	90
15	64.9	349.3	265	42.7	25.4	120.8	228.5	17.1	0.2	67.2	2.9	19.2	3.9	80
16	38.0	126.4	289	35.6	4.2	3.6	122.8	35.4	0.8	106.7	10.3	23.6	3.0	150
18	29.3	162.9	300	25.3	6.2	7.7	155.2	15.1	0.7	55.9	3.2	38.1	3.7	115
19	33.7	123.4	401	29.9	6.1	8.6	114.9	6.3	0.3	81.5	4.0	20.8	13.0	240
20	13.4	46.5	404	11.2	4.0	4.8	41.7	59.0	4.7	88.1	8.8	46.5	1.5	280
21	22.0	51.2	499	17.9	6.4	6.9	44.3	16.1	0.6	220.8	10.9	49.3	13.7	290
22	20.4	89.3	384	19.1	3.2	2.4	86.9	63.3	2.0	94.1	3.1	39.4	1.5	120
Vertical-step knickpoint														
1	64.7	666.4	442	56.7	9.7	32.6	633.8	17.3	0.2	70.8	3.6	38.3	4.1	
1	64.7	666.4	371	54.0	12.4	39.5	626.9	70.8	3.6	137.8	6.0	42	1.9	
1	64.7	666.4	231	40.7	25.7	121.7	544.7	20.7	0.2	81.5	7.7	37.9	3.9	
2	16.0	70.6	324	4.5	13.2	63.8	6.7	10.5	0.3	40.4	2.4	34.5	3.8	
5	117.4	950.6	209	44.5	75.0	408.9	541.7	48.5	1.3	498.2	15.8	85.3	10.3	
6	48.8	319.4	317	35.5	15.8	38.8	280.6	36.5	1.7	494.5	16.6	46.9	13.5	
7	33.9	198.9	304	7.6	29.6	173.4	25.5	61.9	1.5	155.2	6.8	60.4	2.5	
9	10.2	46.8	342	5.9	7.2	16.2	30.6	14.3	1.0	263.6	7.1	54.3	18.4	
12	16.7	51.6	75	14.3	4.5	3.1	48.5	6.9	0.9	19.2	0.7	7.2	2.8	
13	77.9	422.3	507	70.8	9.2	15.3	407.0	19.0	0.2	78.2	2.5	20.4	4.1	
15	64.9	512.1	174	25.6	42.5	261.5	250.6	21.0	0.3	101.0	5.2	27.1	4.8	
17	31.7	190.4	73	28.6	4.7	5.8	184.6	11.4	0.5	19.3	0.4	13.2	1.7	
19	33.7	123.4	311	24.3	11.7	36.9	86.6	18.0	0.5	93.1	9.6	24.3	5.2	
20	13.4	46.5	246	6.7	8.6	25.6	20.9	41.3	3.2	171.9	6.4	48.5	4.2	

Elev = Knickpoint elevation; Dfm = knickpoint distance from mouth; Dfd = Knickpoint distance from divide; Area up = drainage area upstream of the knickpoint; Area down = drainage area downstream of the knickpoint; K_{sn} up = K_{sn} upstream of the knickpoint; K_{sn} down = K_{sn} downstream of the knickpoint; K_{sn} at kp = K_{sn} at knickpoint.

SOURCE: Author's production.

Figure 5.13 - Distribution of k_{sn} and knickpoints, with the location of the studied fluvial systems and rock groups.

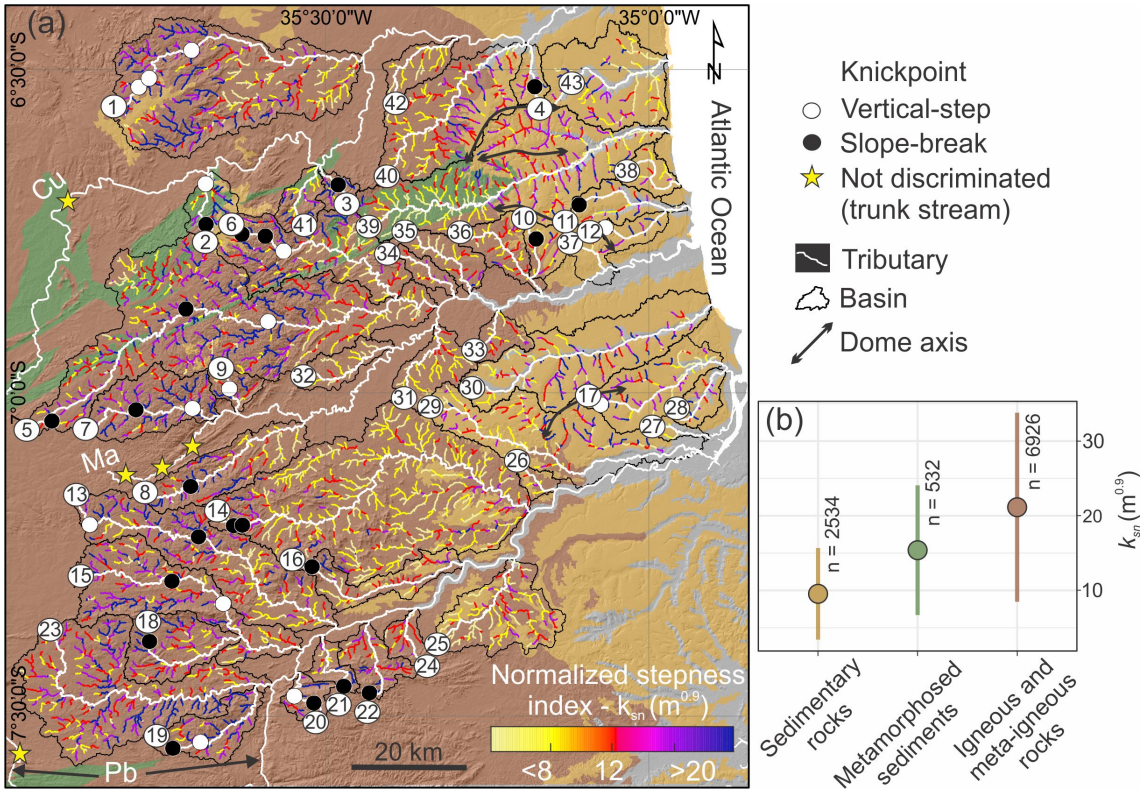

(a) Tributaries coloured by k_{sn} values, with the location of knickpoints, basins, and spatial boundaries of rock groups of similar relative resistance to erosion (yellow color in a = sedimentary rocks; green = metamorphosed sediments; and brown = igneous and meta-igneous rocks; see Table 4.1 for the definition of rock groups). Grey color = masked alluvial/marine/aeolian areas. k_{sn} values were classified by quantiles. Trunk streams: Cu = Curimataú; Ma = Mamanguape; Pb = Paraíba. (b) Average k_{sn} values for the studied rock groups. Uncertainties in b refer to standard deviation. The number of samples analyzed is displayed besides each error bar.

SOURCE: Author's production.

The spatial distribution of the drainage network showed at least three major zones with a relatively similar range of k_{sn}: (i) high values to the west; (ii) low values in the centre; and (iii) intermediate values around the plateau and dome morphologies (Figure 5.13a). The analysis of average k_{sn} values of rock types showed an increased slope of channels flowing over more resistant rock units (i.e., igneous and meta-igneous rocks of the Precambrian basement), in contrast to low steepness channels, which drain over less resistant rock units (i.e., sedimentary rocks; Figure 5.13b).

Abrupt changes in k_{sn} values due to transitions among the main rock types are evident in the northwest portion of the study area, as well as in the northeast sector, where the Precambrian basement rocks are in direct contact with Miocene-Quaternary deposits of the Paraíba Basin (Figure 5.13a). In a broad scale, k_{sn} may be related to differences in bedrock erodibility. However, it is important to note that we also recorded changes in k_{sn} within regions with rock types with relatively similar resistance to erosion (Figure 5.13a), which cannot be explained only by lithological control. Most importantly, this analysis showed a low variability of k_{sn} values among different rock groups, ranging from 10 to 20 on average only, with high uncertainties.

A comparison between the k_{sn} at slope-break and vertical-step knickpoints showed that the former is positively scaled with the relative relief ($r^2 = 0.61$), in contrast to the latter, which had a weak ($r^2 = 0.36$) positive linear relationship with the relative relief (Figure 5.14a). The high scatter and the absence of a clear spatial correspondence with the tectonic structures of the study area suggest that the vertical-step knickpoints may have some lithological influence. Therefore, the following analyses were carried out based only on the slope-break knickpoints, given their higher tectonic significance (KIRBY; WHIPPLE, 2012; WHIPPLE et al., 2013).

Figure 5.14 - Statistical analysis of knickpoints and distributions of k_{sn} and elevation along the coast.

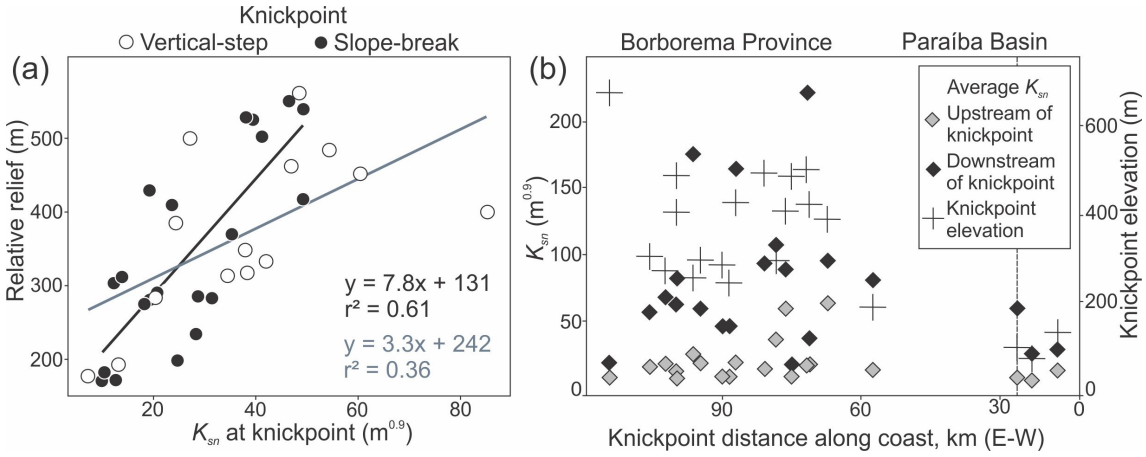

(a) Linear regression between k_{sn} at knickpoint and relative relief. (b) Distribution of k_{sn} values (upstream and downstream of slope-break knickpoints) and knickpoint elevations along the coast (E-W).

SOURCE: Author's production.

The distribution of average k_{sn} (i.e., upstream and downstream of knickpoint) along the coast (E-W) showed that the k_{sn} downstream of knickpoint is higher than upstream (Figure 5.14b). In addition, relatively higher k_{sn} ratios were found for rivers flowing inland over the Precambrian basement rocks (Table 5.2), with a few exceptions (e.g., dome-like reliefs). A comparison between the knickpoint distance along the coast and the k_{sn} upstream of knickpoint did not reveal any correlation ($r^2 = 0.0006$), but a weak correlation ($r^2 = 0.02$) was found for the k_{sn} downstream of knickpoint. Knickpoint elevations were also higher toward the Precambrian basement (Figure 5.14b), which are compatible with the regional morphology of the study area (Figure 3.1b). Similarly, the incision estimated based on the reconstruction of paleo-profiles suggests that the rivers located inland over the Precambrian basement have higher incision than those located over sedimentary units of the Paraíba Basin (Table 5.2). The average incision calculated for the study area was of $\sim$ 140 m. This value was of $\sim$ 156 m and 43 m for the Precambrian basement and sedimentary basin, respectively.

In order to investigate the formation and behaviour of the slope-break knickpoints recorded herein, we also analyzed some of their horizontal and vertical components (Figure 5.15). The analysis of the drainage area versus knickpoint elevation and knickpoint elevation against knickpoint distance from mouth showed weak relationships when the slope-break knickpoints are analyzed together (Figure 5.15a-b). In contrast, these relationships were strengthened when the knickpoints of the north and south of the study area were analyzed individually. The southern knickpoints are located entirely over high-elevation Precambrian basement rocks, around the Cariatá Graben margins, with significant topographic heights; while northern knickpoints are located in the Patos shear zone region, over both, Precambrian basement rocks and moderate-elevation sedimentary deposits of the Paraíba Basin (Figure 5.16). The knickpoints from the northern and southern sectors showed positive ($r^2 = 0.43$ and 0.51) and negative ($r^2 = 0.42$ and 0.46) linear relationships, respectively. The drainage area versus knickpoint elevation showed that higher elevation knickpoints occurred in larger basins of the northern sector, with higher elevation knickpoints in smaller basins of the southern sector (Figure 5.15a). Furthermore, higher elevation knickpoints had higher retreat distances in the northern sector, whereas the higher elevation knickpoints showed relatively lower knickpoint retreat distances in the southern sector (Figure 5.15b).

Figure 5.15 - Statistical analysis of the slope-break knickpoints.

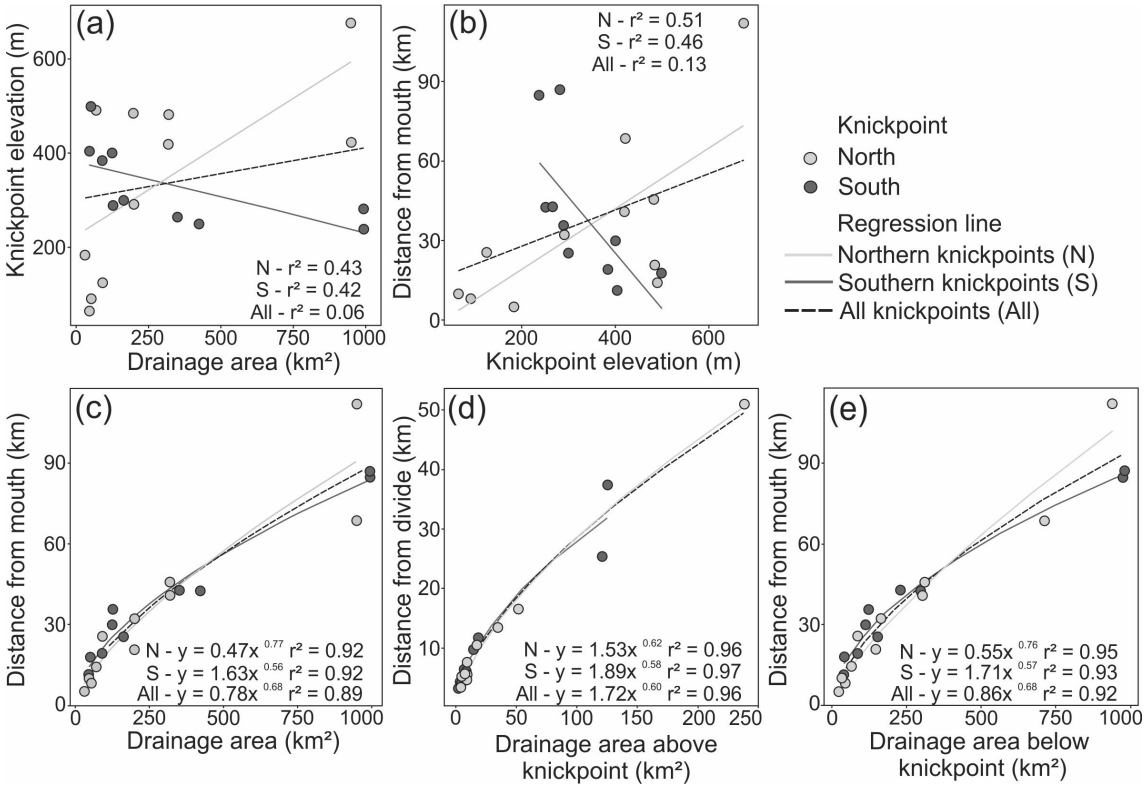

Linear regressions: (a) drainage area versus knickpoint elevation; (b) knickpoint elevation versus knickpoint distance from the mouth; (c) total drainage area versus knickpoint distance from the mouth; (d) drainage area above knickpoint versus knickpoint distance from the divide; and (e) drainage area below knickpoint versus knickpoint distance from the mouth. The last three regressions were fitted by a power-law function in the general form of Hack's law ($L = kA^h$) (HACK, 1957).

SOURCE: Author's production.

The discrepancies in the knickpoint relationships led us to test two different clusters in the study area, using some knickpoint attributes (Table 5.3). The T-test showed that the means of the relative relief (moving window sizes of 3000 and 5000 m) of the southern knickpoints are statistically different from the means of the northern ones (p-value <0.05; Table 5.3), assuming an α of 0.05. The Mann Whitney U test did not show any statistically differences in the knickpoint attributes from both sectors. However, it is important to note that the results found herein were based on a limited set of knickpoints that may not represent their true population.

Figure 5.16 - A 3D-view of the relief of the study area based on SRTM-DEM (vertical exaggeration of 30×), with the location of tributaries, slope-break knickpoints and main tectonic structures.

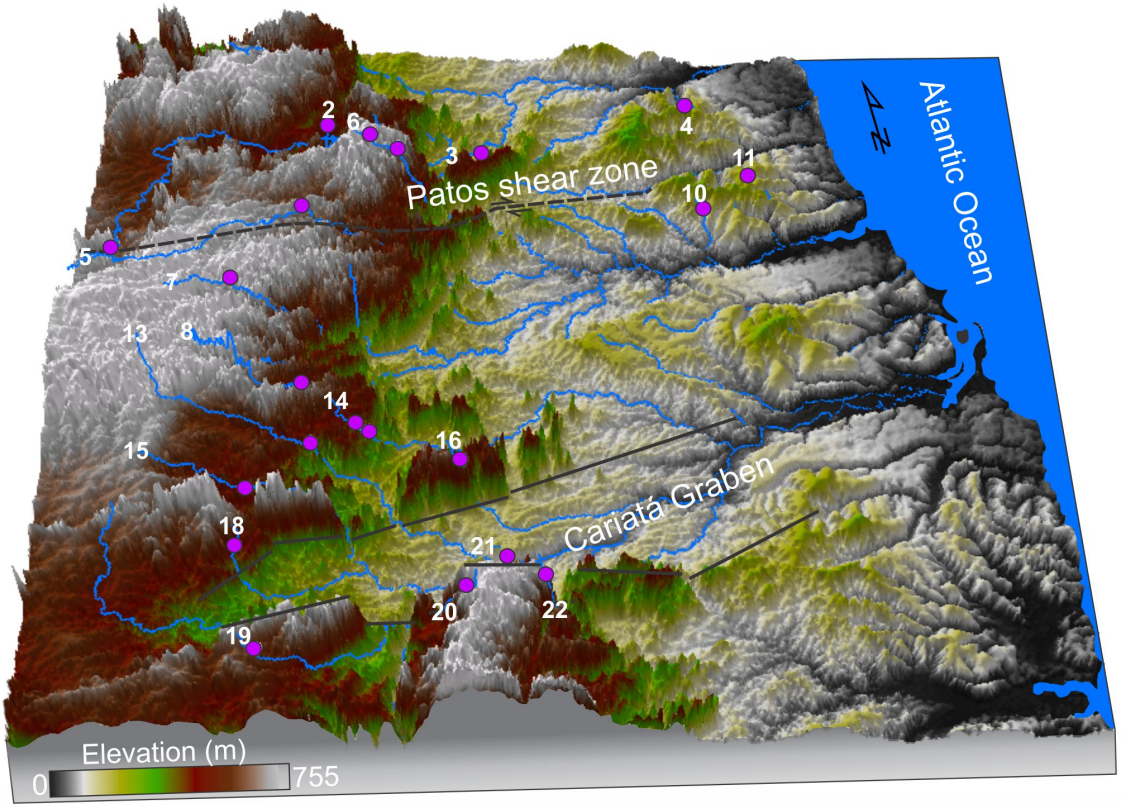

Purple dot = slope-break knickpoint; blue line = numbered tributary with knickpoint. Solid black line = normal fault; dashed black line = dextral strike-slip fault. The location of the Patos shear zone and faults bounding the Cariatá Graben was based on Bezerra et al. (2008), Bezerra et al. (2014) and Lima et al. (2017).

SOURCE: Bezerra et al. (2008), Bezerra et al. (2014) and Lima et al. (2017).

The horizontal distances of the knickpoint retreat positively scaled with the total drainage area, and the drainage area below and above the slope-break knickpoints, with strong r^2 coefficients (i.e., $r^2 > 0.89$; Figure 5.15c-e). Knickpoints from larger basins (e.g., rivers 5 and 14, see Table 5.2) travelled further upstream than knickpoints from smaller basins (e.g., rivers 3, 4 and 20). The drainage area upstream of knickpoints ranged from 4.2 to 238.3 km^2 for the northern knickpoints and from 2.4 to 125.3 km^2 for the southern knickpoints. Hack's exponents varied from 0.60-68 for all knickpoints; 0.62-0.77 for the northern knickpoints; and 0.56-0.58 for the southern knickpoints (Figure 5.15c-e).

Table 5.3 - Results with the unpaired two-samples T and Mann-Whitney U statistical tests comparing attributes derived from the northern and southern knickpoints of the study area.

Unpaired two-samples T-test							
Knickpoint attribute	Sector	Average	Standard deviation	Shapiro-Wilk test: p-value	Levene test: p-value	Two sample t-test: t-statistic	Two sample t-test: p-value
Elevation	N	339.1	200.0	0.337	0.004	0.119	0.907
	S	331.2	85.5	0.168			
* Relative relief	N	139.1	41.9	0.471	0.003	-1.640	0.124
	S	186.7	82.5	0.098			
** Relative relief	N	208.5	66.8	0.575	0.013	-2.610	0.021
	S	326.3	128.0	0.223			
*** Relative relief	N	277.6	106.0	0.122	0.591	-3.060	0.006
	S	421.7	109.0	0.074			
$*k_{sn}$	N	28.7	18.1	0.099	0.036	-1.630	0.124
	S	46.1	29.1	0.362			
$**k_{sn}$	N	24.5	14.8	0.090	0.383	-2.010	0.059
	S	38.7	17.7	0.506			
$***k_{sn}$	N	23.0	13.3	0.113	0.570	-1.747	0.097
	S	32.3	10.9	0.348			
Mann-Whitney U test							
Knickpoint attribute	Sector	Median	Interquartile range			Mann Whitney test: W-statistic	Mann Whitney test: p-value
Slope	N	2.71	1.9	-	-	47	0.5965
	S	2.74	0.9	-	-		
Incision	N	100	102	-	-	37	0.218
	S	118	122	-	-		
Drainage basin area	N	199	257	-	-	48	0.6468
	S	145	306	-	-		

Relative relief and k_{sn} tested using three different sizes of moving windows: 1000(*), 3000(**) and 5000 m (***).

SOURCE: Author's production.

5.6 Analysis of divide stability

The χ-map for the complete drainage networks with outlet elevations $\geq$ 1 m asl showed that most divide segments investigated in the study area are stable (D1 and D4-D7), as they did not show significant differences in χ values (χ-anomalies) on both sides of the divide (Figure 5.17a). Moreover, these divides did not display cross-divide differences in the Gilbert metrics (Figure 5.18a-d). D1, D4, D6, and D7, located mostly over Precambrian basement rocks, showed relatively equal mean channel elevation values of about 100 m asl. These divides also showed similar hillslope gradient values of $\sim$ 0.1 and relative relief values ranging between 40 and 75 m. D5, located over Precambrian basement rocks and Paleogene deposits, showed the highest mean elevation value of up to 500 m asl (Figure 5.18a). Similarly, D5 also showed the highest mean hillslope gradient and relative relief values of approximately 0.15 and 75 m, respectively (Figure 5.18b-c).

Significant variations in χ and Gilbert metrics on both sides of the divide suggesting divide migration were recorded for three divide segments (D2, D3, and D8 in Figures 5.17a and 5.18). D8, located in a dome with high elevation constituted by Miocene-Quaternary deposits, showed differences only in the Gilbert metrics of hillslope gradient and relative relief. This divide segment showed the highest mean hillslope gradient and relative relief values (0.15 and 75 m, respectively), with northward divide motion (Figure 5.18b-c-d). Divide segments 2 and 3, located in the southeast portion of the study area, showed differences in both χ and Gilbert metrics, with relatively similar topographic metrics (average channel elevation $\sim$ 100 m; hillslope gradient $\sim$ 0.05; relative relief $\sim$ 75 m; Figure 5.18a-d). χ and Gilbert metrics suggest divide movement to the southeast for D2 and northeast for D3 (white arrows in Figure 5.17a). Divide movements follow the inland position of a high-elevation, chevron-shaped plateau covered by eroded overlying Miocene and Quaternary deposits of the Paraíba Basin and underlying Precambrian basement rocks (compare divide location in Figure 5.17a with the geological map in Figure 3.2). The presence of an ongoing river capture eastward the plateau, between a tributary from the Una River and the upper Miriri River, as discussed previously (see sections 5.1 and 5.2), is a further evidence supporting divide migration in this region (Figure 5.17b).

Figure 5.17 - χ- map represented by a continuous grid for the drainage network of the study area and the 3D view of a river capture.

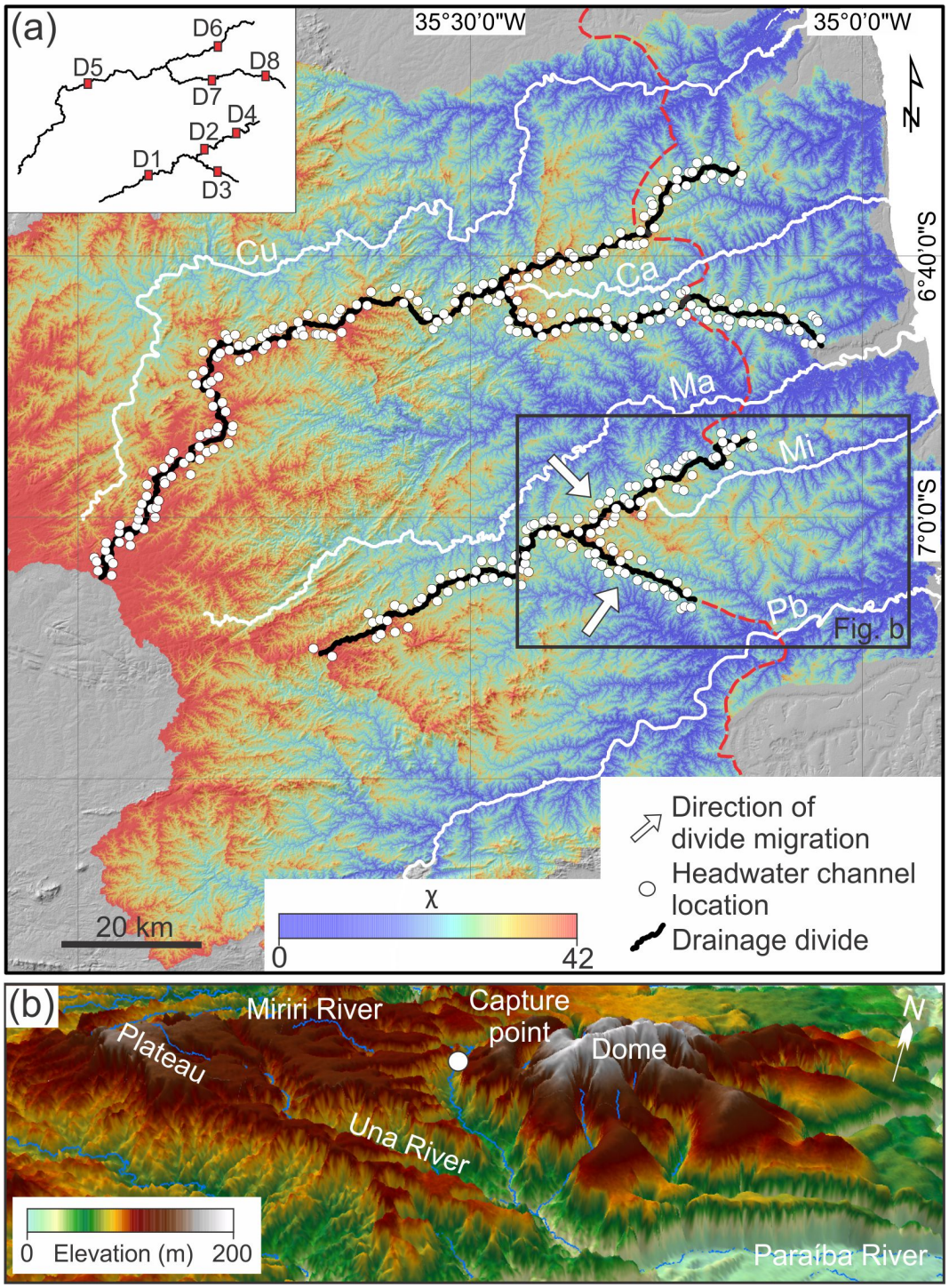

(a) χ-map was based on outlets $\geq$ 1m asl. Trunk streams in a: Cu = Curimataú; Ca = Camaratuba; Ma = Mamanguape; Mi = Miriri; Pb = Paraíba. White arrow = χ-anomaly. Dashed red line = geological boundaries between basement rocks (west) and sedimentary deposits (east). Shaded relief based on SRTM-DEM. (b) SRTM-DEM 3D view showing an ongoing river capture between the Miriri River and a tributary of the Una River (vertical exaggeration = 30×). White circle in b = possible capture point.

SOURCE: Author's production.

Figure 5.18 - Cross-divide statistics (average and standard deviation) and delta values based on Gilbert metrics and χ, including the estimated direction of the divide migration (see the location of divide segments in Figure 5.17a).

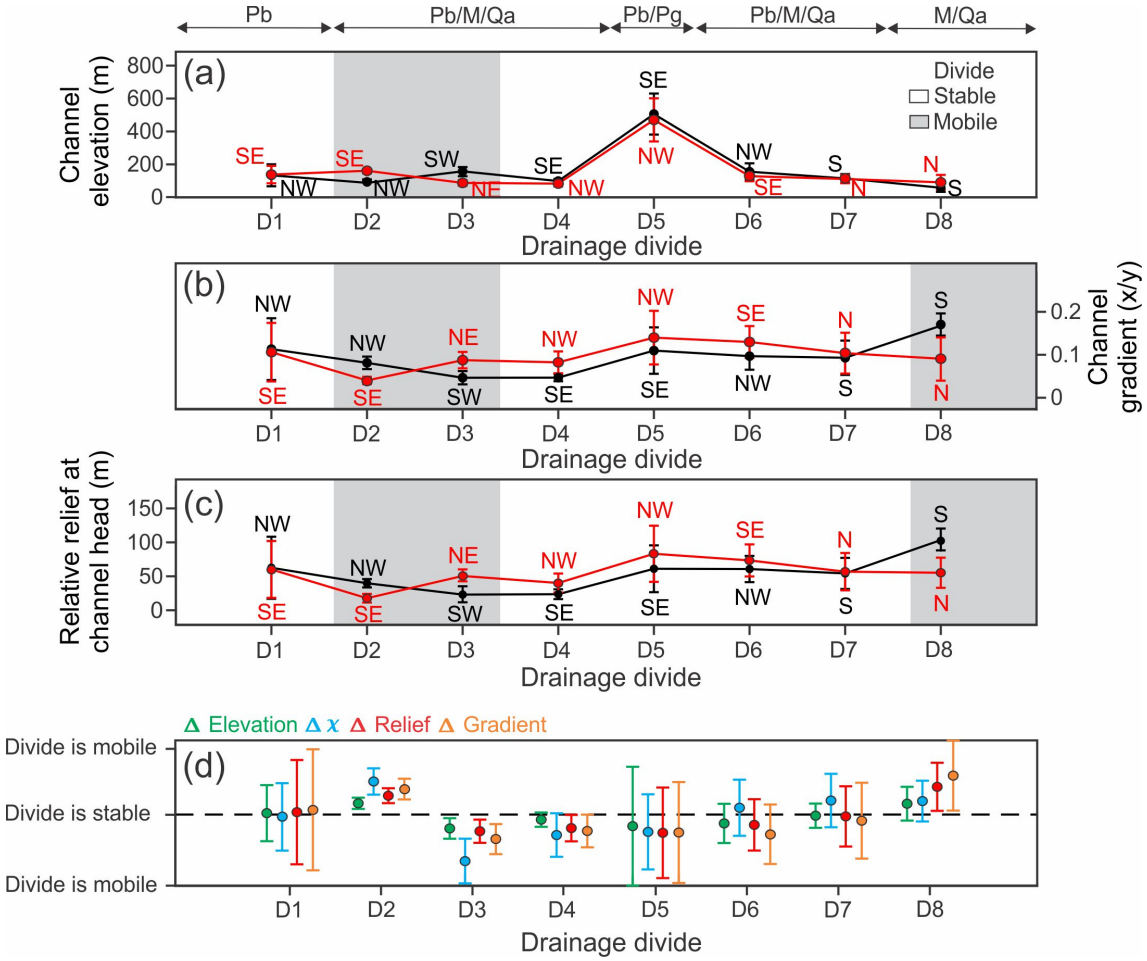

(a) Channel elevation; (b) channel gradient; (c) relative relief at channel head. Red and black lines represent the sides of the drainage divide. The main geological units of each divide segment are presented on the top of the graph in a. Pb = Precambrian basement rocks; Pg = Paleogene unit; M = Miocene unit; Qa = Quaternary unit. (d) Normalized cross-divide delta values (c.f., Forte and Whipple (2018)) and uncertainties (standard deviation) for each of the four metrics derived from headwater channels, illustrating the stable and mobile divide segments in the study area.

SOURCE: Author's production.

5.7 Pre-processing of regional and local geomorphometric variables

The geomorphometric variables showed a positive skewed frequency distribution for the slope (skewness = 1.63, Figure 5.19a). This variable was more normalized, with a

quasi-normal distribution (skewness = -0.006), after its transformation by the Box-Cox method (log method; $\lambda = 0.0$), relative to other λ exponents (Figure 5.19b-f). Therefore, this exponent was also selected to normalize the regional geomorphometric variables (Figure 5.19g-l). The original profile curvature revealed a leptokurtic distribution, characterized by a tall peak and short tails (kurtosis = 7.25; Figure 5.19m). This variable revealed a quasi-mesokurtic (normal) distribution (kurtosis = 2.88; Figure 5.19n) after its transformation by the arctangent method. The manipulation of the profile curvature to absolute values also revealed a less skewed distribution after normalization (skewness = 0.82) than the non-normalized original profile curvature (skewness = 2.26; compare Figure 5.19o-p).

Figure 5.19 - Histograms of the frequency distribution for the geomorphometric variables before and after the normalization by the Box-Cox and arctangent methods.

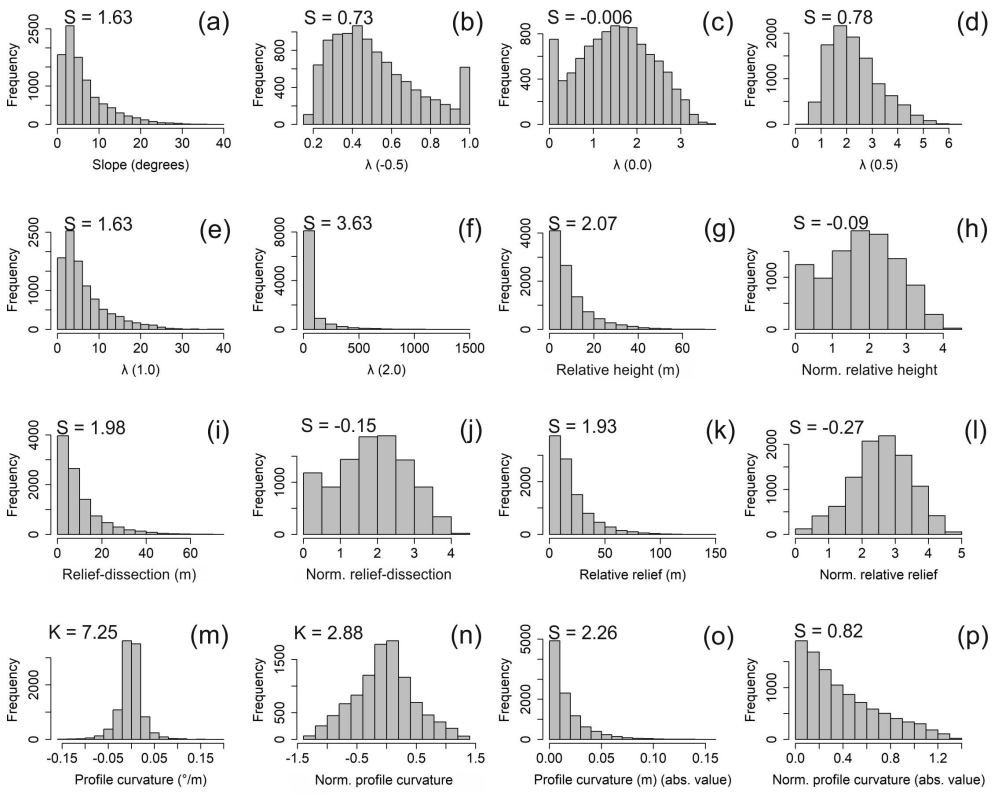

(a-f) Slope; (g-h) relative height; (i-j) relief-dissection; (k-l) relative relief; and (m-p) profile curvature. S= skewness; K = kurtosis; prefix Norm = Normalized variable.

SOURCE: Author's production.

The matrix of determination coefficients (r^2) of the fifteen geomorphometric variables tested for geological discrimination in the present work is shown in Table 5.4. This analysis suggests that the highest frequency of relationships, with high determination coefficients (i.e., $r^2 > 0.75$), occurred using variables of relative relief or normalized relative relief (Table 5.4). Thus, since the influence of the relative relief and normalized relative relief seems to be identical to the other geomorphometric variables, they were not considered in the following analysis.

Table 5.4 - Matrix of determination coefficients (r^2) for the fifteen geomorphometric variables tested in this work.

Variables	Elev	H	NH	Rr	NRr	D	ND	C7	C21	Pc	NPc	S	NS	Hi	Vd
Elev	**1.00**														
H	0.18	**1.00**													
NH	0.20	0.75	**1.00**												
Rr	0.19	0.81	0.62	**1.00**											
NRr	0.22	0.60	0.77	0.75	**1.00**										
D	0.12	0.39	0.31	0.81	0.62	**1.00**									
ND	0.14	0.30	0.34	0.62	0.77	0.75	**1.00**								
C7	0.00	0.12	0.23	0.13	0.21	0.10	0.16	**1.00**							
C21	0.00	0.04	0.09	0.05	0.07	0.04	0.05	0.27	**1.00**						
Pc	0.09	0.13	0.10	0.19	0.22	0.17	0.16	0.07	0.01	**1.00**					
NPc	0.10	0.15	0.13	0.21	0.27	0.19	0.19	0.06	0.01	0.88	**1.00**				
S	0.19	0.67	0.54	0.83	0.67	0.67	0.54	0.12	0.01	0.18	0.20	**1.00**			
NS	0.20	0.53	0.62	0.67	0.81	0.54	0.64	0.16	0.02	0.20	0.24	0.82	**1.00**		
Hi	0.00	0.10	0.19	0.00	0.01	0.10	0.19	0.00	0.00	0.00	0.00	0.00	0.00	**1.00**	
Vd	0.01	0.02	0.01	0.12	0.12	0.24	0.21	0.00	0.00	0.08	0.09	0.12	0.12	0.12	**1.00**

Elev = elevation; H = relative height; Rr = relative relief; D = relief-dissection; C7 = 7x7 topographic coherence; C21 = 21x21 topographic coherence; Pc = profile curvature; S = slope; Hi = hypsometric integral; Vd = valley depth; prefix N = normalized variable.

SOURCE: Author's production.

Boxplot statistical distributions for the main geological domains of the study area (i.e., pre-Miocene basement rocks and Miocene-Quaternary deposits; see geological map in Figure 3.3), based on a number of 1000 random samples showed that the pixel-based geological discrimination is difficult. This is due to the high overlapping of the distribution of the geomorphometric variables, although some of them showed a certain degree of discrimination (e.g., valley depth, hypsometric integral, and topographic coherence; Figure 5.20). Alternatively, the experiments in this work suggest that, after applying the regionalization of the geomorphometric variables, the degree of geological discrimination may increase, together with the relationships between the geomorphometric variables, as reported by Valeriano and Rossetti (2017). For instance, the linear regression analysis after the regionalization of geomorphometric

variables (size of the mapping unit = 1000), with the slope as independent variable, resulted in r^2 values of 0.28 for the elevation; 0.86 for the relief-dissection; 0.72 for the normalized relief-dissection; 0.82 for the profile curvature; 0.79 for the normalized profile curvature; and 0.82 for the relative height. These r^2 values are significantly higher than those calculated for the geomorphometric variables in a pixel-based approach (compare the values in Table 5.4).

Figure 5.20 - Boxplots of the pixel-based geomorphometric variables grouped by geological domains.

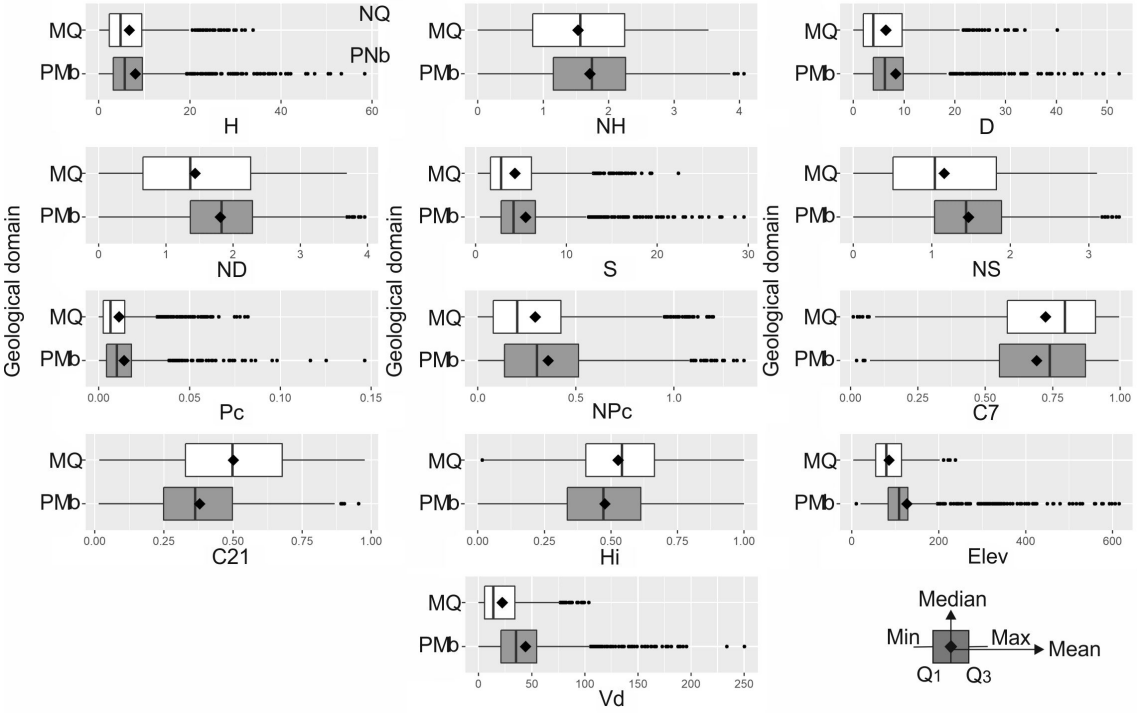

Pre-Miocene basement rocks (PMb); Miocene-Quaternary deposits (MQ). H = relative height; D = relief-dissection; S = slope; Pc = profile curvature; C7 = 7x7 topographic coherence; C21 = 21x21 topographic coherence; Hi = hypsometric integral; Elev = elevation; prefix N = normalized variable.

SOURCE: Author's production.

5.8 Geological discrimination of the northern Paraíba Basin by geomorphometry

Regionalization techniques applied to a set of thirteen geomorphometric variables were the most suitable for the geological discrimination of surface units in the north-

ern Paraíba Basin. The results with the discriminations for the 3 sectors analyzed here (Figure 5.21) are described in the following.

Figure 5.21 - Location of the sectors analyzed for the geological discrimination in the study area.

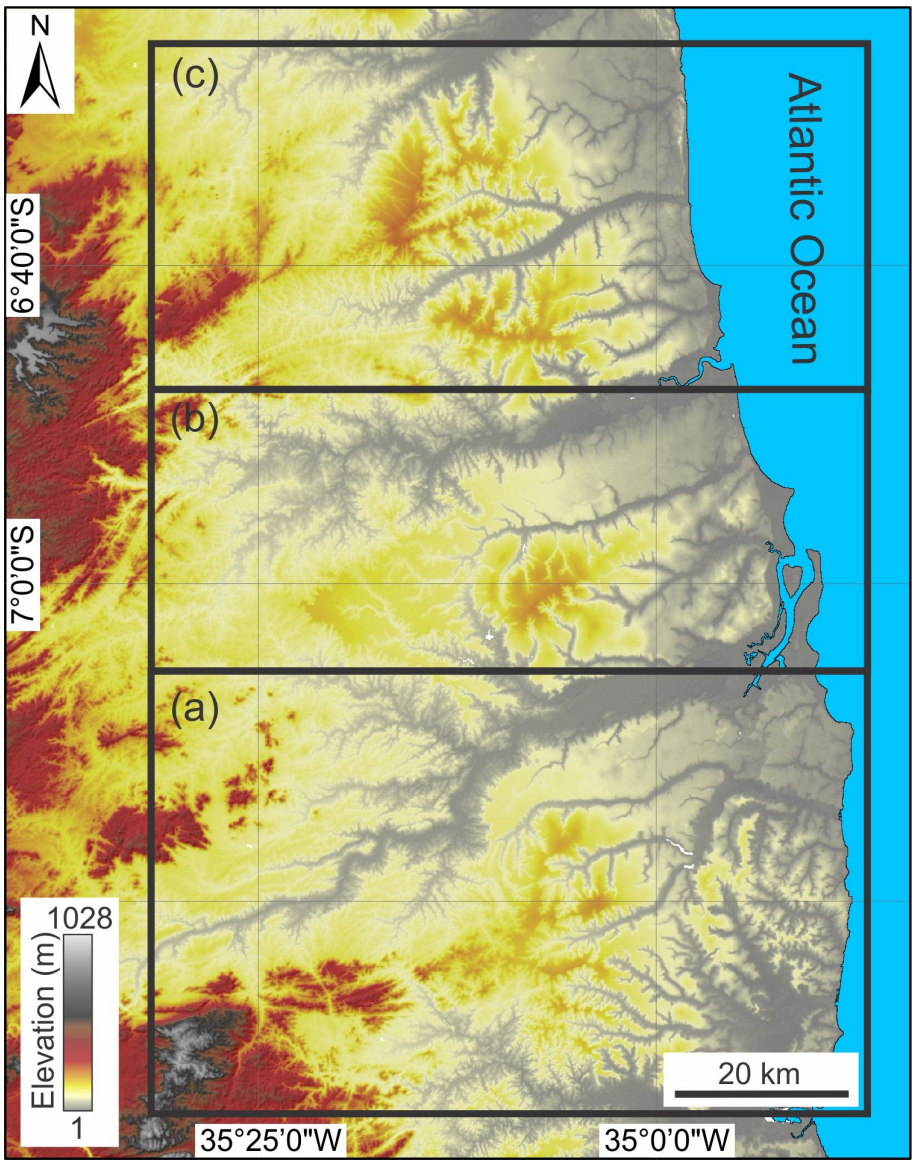

(a) Southern, central (b) and northern (c) sectors.
SOURCE: Author's production.

5.8.1 General level

A summary of the variables, mapping units, statistics for geomorphometric regionalization, and critical thresholds used to discriminate the geological terrains of the study area at general level is shown in Table 5.5. After several tests, we found that the valley depth showed the most reliable results for establishing the mapping units for the first sets of regionalizations (Figures 5.22a, 5.23a, and 5.24a). High vertical differences between ridges and valleys (i.e., valley depth) are expected to occur: i) in terrains characterized by high topography, as those over Precambrian basement rocks; ii) in sectors with sudden changes in topography, for instance, along uplifted and subsided blocks; and iii) on the borders between paleocliffs and coastal plains (Figure 5.25b-c-d). High to moderate values of valley depth were found chiefly in the southwest and northwest regions of the southern sector, as well as along the main river valleys (dark grey to black areas in Figure 5.22a). A critical threshold of valley depth ($\geq$ 23 m) was used to eliminate segments of pre-Miocene basement rocks from Miocene-Quaternary deposits. However, this first attempt to discriminate geological terrains based on the valley depth was not successfully achieved because some pre-Miocene basement segments (for instance, those with high values of elevation and slope) were also classified as having low values of valley depth. Therefore, contiguous extensions of shallower valleys (less than 23m deep) were taken as mapping units (Figure 5.22b) for the regionalization of elevation and slope values. The remaining segments of the pre-Miocene basement were eliminated by selecting critical thresholds of elevation ($>$ 57 m) and slope ($>$ 0.03 degrees; see black lines in Figure 5.22c-d).

Table 5.5 - Summary of parameters and criteria used for the regionalization of geomorphometric variables in the general level (see text for further explanation).

Regionalization						Hierarchy
First set of mapping units	Cut-off threshold	Criteria for grouping pre-existing mapping units	Variable	Statistics	Critical threshold/ interval for geomorphometric characterization	
Southern sector						
Valley depth	23	Spatial contiguous regions	Elevation	Min	57	1
-	-		Slope		0.36	2
Central sector						
Valley depth	27	-	Slope	Mode	2	1
-	-	Geomorphometric similarity (slope mode)	Hypsometric integral		5	2
-	-	Geomorphometric similarity (hypsometric integral mode)	*Topographic coherence	Average	0.64-0.69	3
-	-		Elevation	Mode	86-95	4
Northern sector						
Valley depth	22	-	Slope	Mode	10	1
-	-	Geomorphometric similarity (slope mode)	**Topographic coherence	Average	0.46	2
-	-		Elevation	Max	246	3

Max = Maximum value; Min = Minimum value; * 7x7 Topographic coherence; ** 21x21 Topographic coherence.

SOURCE: Author's production.

Figure 5.22 - Results with the regionalization for the southern sector of the study area.

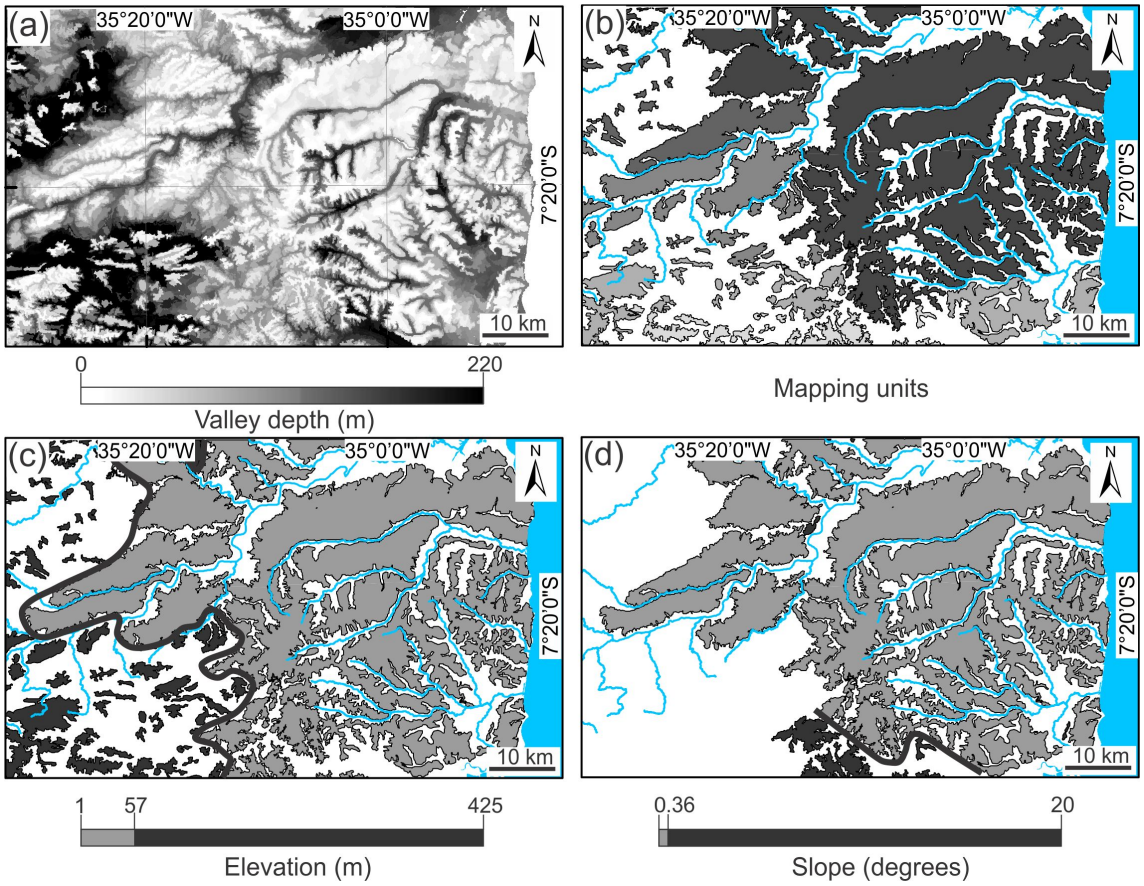

(a) Details of the regionalized valley depth (size of the scale parameter = 1000). (b) Mapping units derived from the valley depth. (c-d) Regionalized elevation (c) and slope (d). Blue line = main drainage system. Black line = geological boundary of pre-Miocene basement rocks to the northwest and southwest.

SOURCE: Author's production.

The central sector of the study area showed lower values of valley depth than the southern sector (Figure 5.23a). It was suggested that the selection of terrains with values of valley depth $\geq$ 27 m was suitable to eliminate segments of pre-Miocene basement rocks located mostly in the northwest sector, as well as a significant number of segments of marine/fluvial deposits along the main valleys to the east. However, a significant number of segments related to eroded terrains over pre-Miocene basement rocks (see, for instance Figure 5.25a) was still present after this first analysis. Some of these segments were eliminated with the slope regionalization (critical threshold $>$ 2 degrees), as they had higher slope values, especially those located

in the central part of the study area (Figure 5.23b). Also, there was a high spatial correspondence between the values of the hypsometric integral and the geological compartments. Therefore, the regionalization of the hypsometric integral using mapping units from segments with similar slopes (Figure 5.23c-d) was efficient to eliminate highly dissected pre-Miocene basement rocks to the west since they were characterized by lower hypsometric values (critical threshold $\leq$5). However, the similarities between geomorphometric responses of both geological compartments still occurred, probably due to the local influence of the dome-shaped relief to the east (Figure 5.1). This dome, located over sedimentary deposits, has higher elevation values and can be confused with Precambrian rocks located at higher topographic levels. Exploratory analysis, based on topographic coherence and elevation, revealed specific intervals with the potential to discriminate the remaining segments. Thus, these variables were regionalized using segments with similar values of the hypsometric integral as mapping units (Figure 5.23e). The definition of critical intervals (topographic coherence = 0.64 and 0.69 and elevation = 86 and 95 m) allowed to eliminate segments of pre-Miocene basement rocks typified by terrains with various aspects and moderate to high elevations (Figure 5.23f-g).

Figure 5.23 - Results with the regionalization for the central sector of the study area.

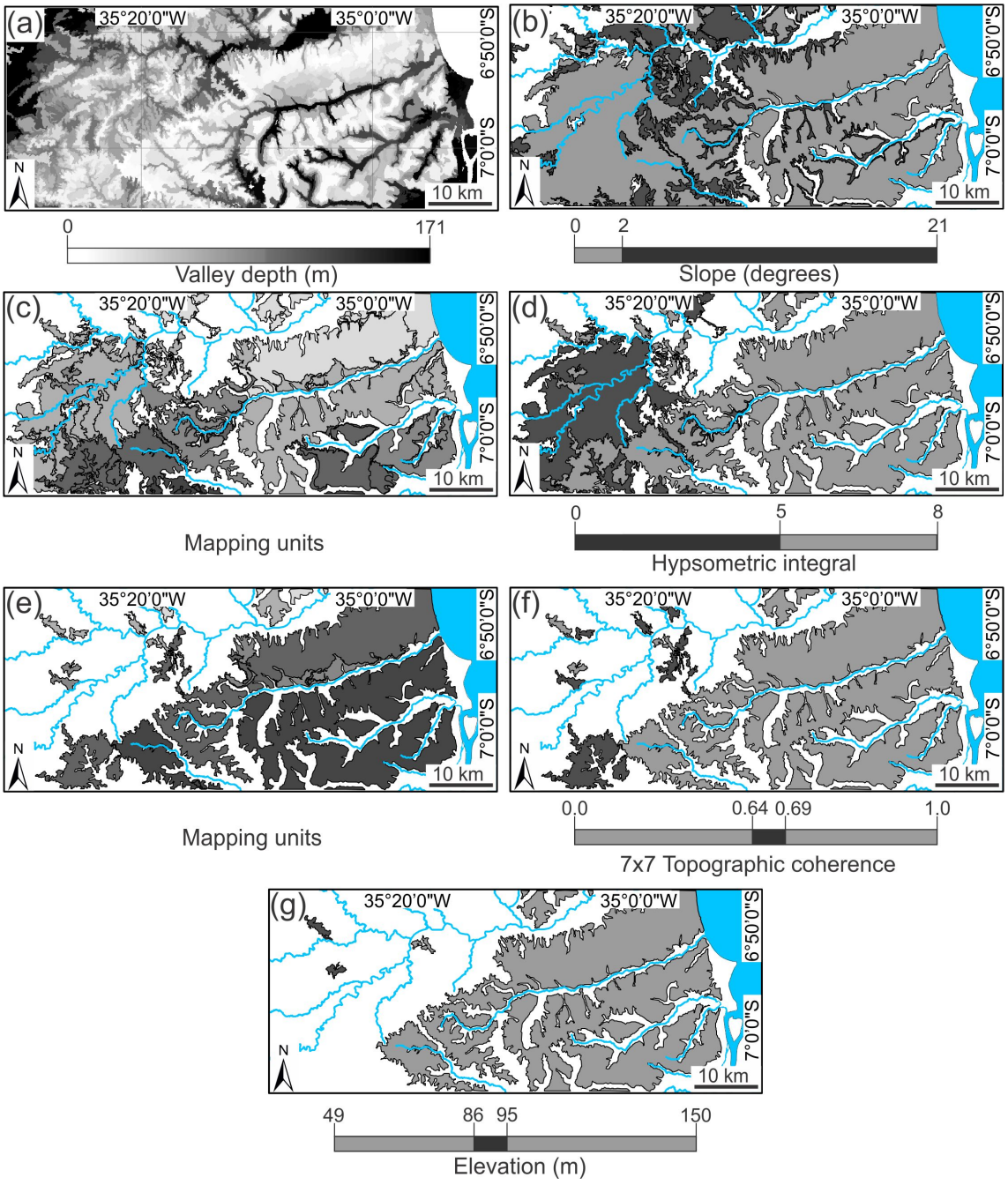

(a) Details of the regionalized valley depth (size of scale parameter = 3000). (b) Regionalized slope based on mapping units derived from the valley depth. (c) Mapping units derived from the slope. (d) Regionalized hypsometric integral generated from the mapping units shown in c. (e) Mapping units generated by the hypsometric integral. (f-g) Regionalized 7x7 topographic coherence (f) and elevation (g) from the mapping units shown in e. Blue lines = main drainage system.

SOURCE: Author's production.

There were segments with high values of valley depth in the northern sector of the study area, as well as along the main valleys to the east (Figure 5.24a). These segments, located on pre-Miocene basement rocks and marine/alluvial deposits, respectively, were eliminated with the valley depth (critical threshold > 22 m; Figure 5.24b). In addition, segments on terrains with pre-Miocene basement rocks in the southwest portion of the study area showed high slopes, so they were eliminated with the slope regionalization (critical threshold ≥ 10 degrees; Figure 5.24c). The exploratory analysis also revealed remaining segments of the pre-Miocene basement with diffuse aspects and high elevation values. Additional regionalizations using the topographic coherence and elevation based on the mapping units generated from the slope (Figure 5.24d) were performed. The establishment of critical thresholds for the topographic coherence and elevation (critical threshold $= \leq 0.46$ and ≥ 246 m, respectively) allowed the elimination of a considerable number of segments (see black lines in Figure 5.24e-f).

The geological boundaries of Miocene-Quaternary deposits (i.e., eluvial/colluvial deposits and Barreiras Formation) comparing the available geological maps and the geological discrimination, at the general level, resulting from this work is shown in Figure 5.26. The Miocene-Quaternary sedimentary terrain boundaries derived from our methodology (area = 3459 km^2) generally matched with those from official geological maps at the scales of 1:1000000 (area = 3346 km^2) and 1:500000 (area = 3036 km^2). Other agreements included several patches of Miocene-Quaternary deposits within the area dominated by Precambrian basement rocks to the southwest and areas presumably of alluvial sediments along river valleys. However, it is important to note that the high degree of detailing of the river valleys may have reduced significantly the extension of sedimentary areas in our results, especially along the major rivers (Figure 5.26c).

Figure 5.24 - Results with the regionalization for the northern sector of the study area.

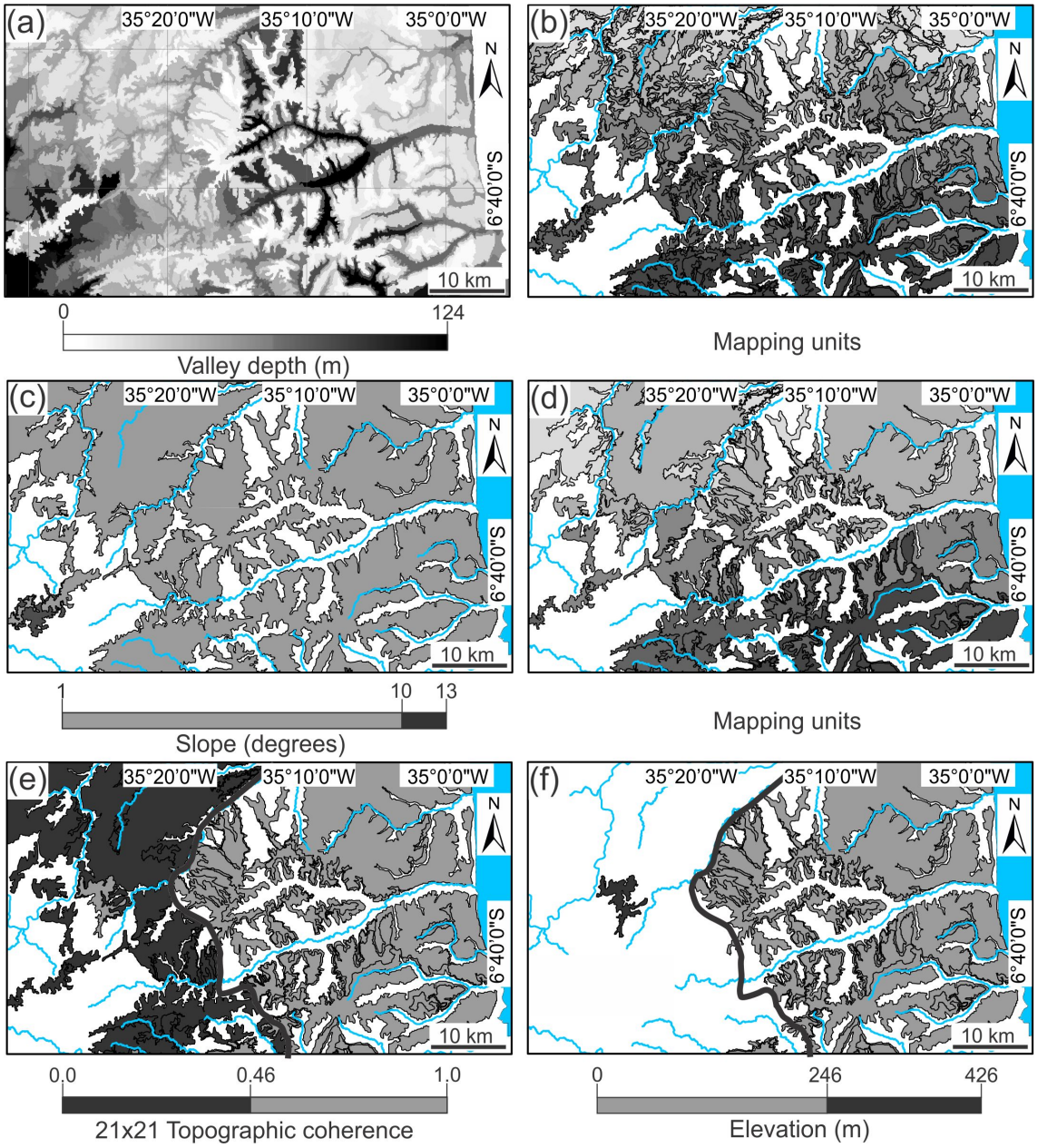

(a) Details of the regionalized valley depth (size of the parameter scale = 5000). (b) Mapping units derived from the valley depth. (c) Regionalized slope from the mapping units shown in b. (d) Mapping units generated from slope. (e-f) Regionalized 21x21 topographic coherence (e) and elevation (f) using the mapping units shown in d. Blue line = main drainage system. Black line = limit of the pre-Miocene basement, which is characterized by a diffuse aspect and high elevation values to the west.

SOURCE: Author's production.

Figure 5.25 - Relief morphologies developed on crystalline basement rocks, Barreiras Formation and Post-Barreiras Sediments.

(a-b) Eroded relief on crystalline basement rocks (a), with high slopes and high topography (white lines in b). (c) Break in the relief at the boundary between the paleocliff and the coastal plain. (d) The Paraíba River valley and its left bank. (e) Smoothed to sinuous sedimentary relief on the Barreiras Formation, with tablelands of higher slopes (white lines). (f-g) Sedimentary relief on the Post-Barreiras Sediments, with flat to smooth hillsides (white lines in g). See the location of field photographs (numbers shown in the upper right side of each photograph) in the map shown in the bottom right corner of the figure. Observe the great vertical distances between ridges and valleys (valley depth, Vd) in the Precambrian relief (b), Paraíba River valley (d) and towards the coastal plain (c).

SOURCE: Author's production.

Figure 5.26 - Geological boundaries of the Miocene-Quaternary deposits comparing official geological maps and the geological discrimination, at the general level, obtained from this work.

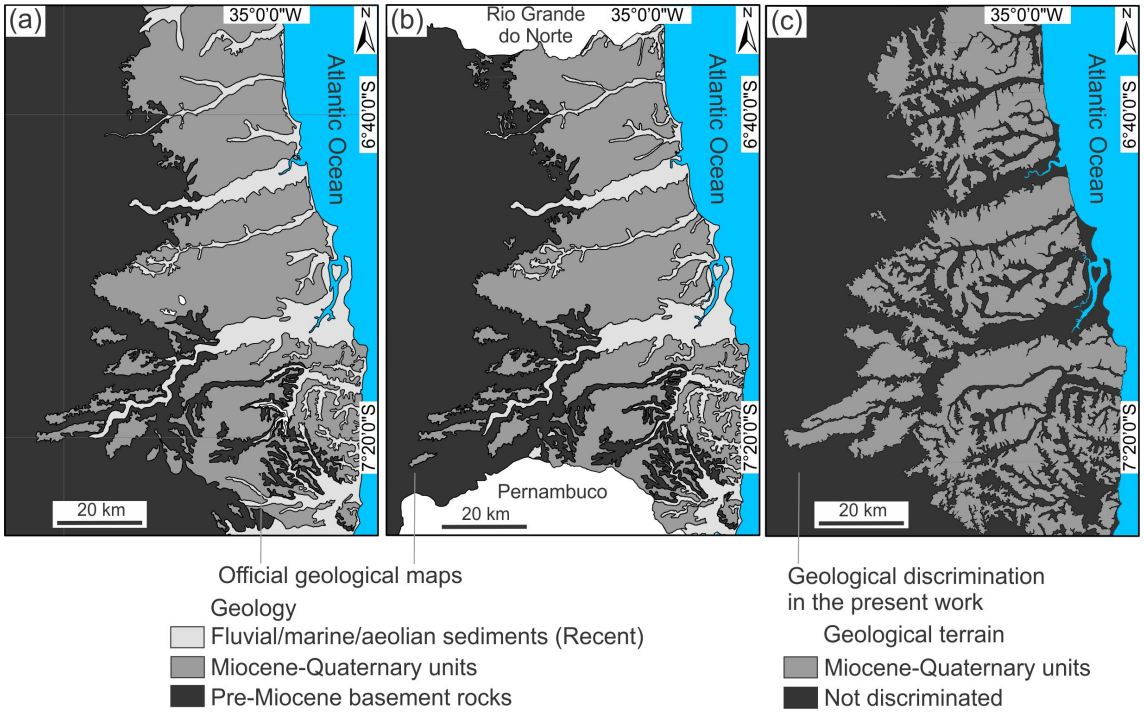

(a-b) Geological maps from the CPRM at the scales of 1:1000000 (a) and 1:500000 (b). (c) Geological discrimination resulting from this work. Geological maps modified from CPRM and Santos et al. (2002).

SOURCE: Santos et al. (2002).

5.8.2 Detail level

A summary of the terrain parameterization used to discriminate the geological terrains (at the detail level) is shown in Table 5.6. Among the geomorphometric variables, only regionalized average and modal slope values showed some geomorphometric significance to discriminate the Barreiras Formation and the Post-Barreiras Sediments in the southern sector of the study area (Figure 5.27a-c). Segments related to the Barreiras Formation displayed higher slopes, especially downstream, than the segments of the Post-Barreiras Sediments (Figure 5.25e-f-g). The visual comparison between the regionalized variables and the detailed geological map of this sector suggested good results for the slope regionalized through modal interval (Figure 5.27a-d). For instance, this variable showed a good agreement in the detec-

tion of contiguous segments, as well as in the record of the Barreiras Formation near river valleys.

Table 5.6 - Summary of the terrain parameterization used for the regionalization of the geomorphometric variables in the detail level (see text for further explanation).

Regionalization					Hierarchy
First set of mapping units	Criteria for grouping of pre-existing mapping units	Variable	Statistics	Critical threshold for geomorphometric characterization	
Southern sector					
Valley depth	-	Slope	Mode	3	1
		Normalized relief-dissection	Average	1.2	2
Central sector					
Valley depth	-	Normalized slope	Average	1.6	1
-	Spatial contiguous regions	21x21 Topographic coherence		0.34	2
Northern sector					
Valley depth	-	Normalized profile curvature	Average	0.33	1

The discriminations are based on the Miocene-Quaternary polygonal boundaries established in the general level (Figure 5.26c).

SOURCE: Author's production.

The visual comparison of different sizes (500, 1000, 2000, and 5000) of mapping units for the regionalization of the slope through the segmentation parameter scale showed some differences concerning to the organization of the terrain patches in the southern sector of the study area (Figure 5.28). This analysis showed that low segmentation thresholds (e.g., 500) produced small and noisier segments, some of them related to artifacts (black arrow in Figure 5.28a). High segmentation thresholds (i.e., > 2000) only promoted higher generalization of segments, for instance, reducing the occurrences of the segments related to the Barreiras Formation (black squares in Figure 5.28; compare with the geological map in Figure 5.27d). Based on these visual inspections, the mapping units of 1000 (Figure 5.28b) were selected as an optimum size for regionalizing the slope (mode).

Figure 5.27 - Comparison of the results obtained with the regionalization of the slope for the southern sector of the study area.

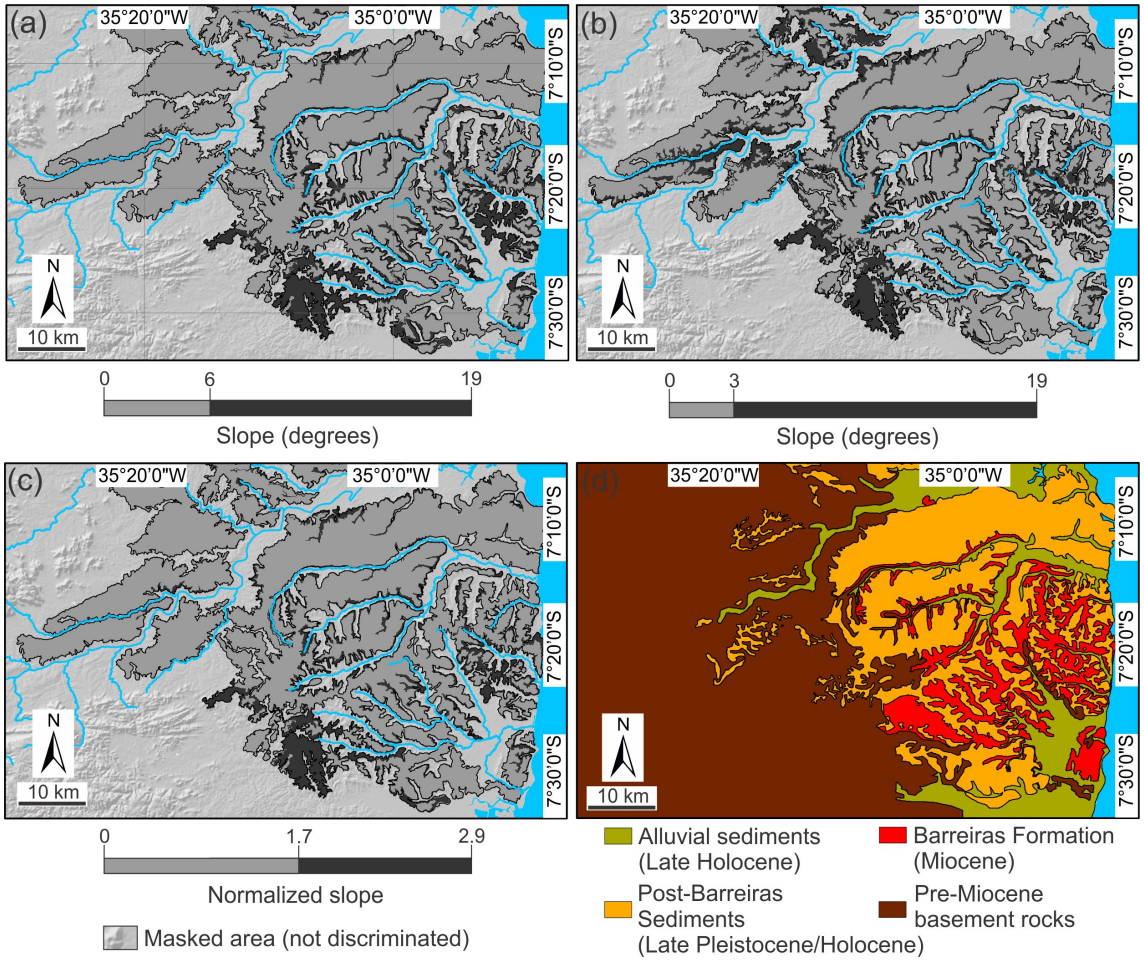

(a-b) Regionalized slope using the average (a) and mode (b) as statistics. (c) Regionalization of the normalized slope by average. Blue lines = main drainage system. (d) Detailed geological map.

SOURCE: Geological map was modified from Rossetti et al. (2012).

Figure 5.28 - Comparison of the regionalized slope using different sizes of mapping units according to the parameter scale considering the levels of 500 (a), 1000 (b), 2000 (c), and 5000 (d).

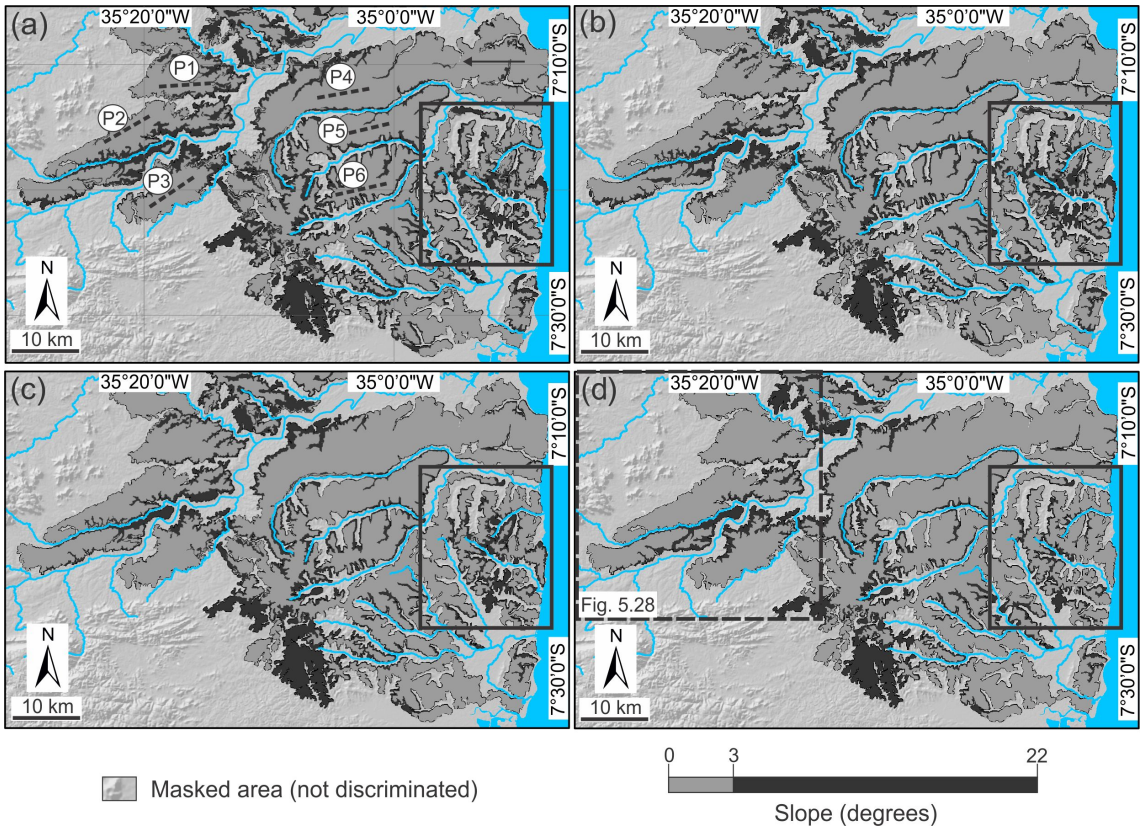

Topographic profiles (dashed black lines) are shown in Figure 5.29a. Black arrow = artifact; insert box = reduction of the segments related to the Barreiras Formation as the size of mapping units increases. The range of slope was standardized for comparison. Blue line = main drainage system.

SOURCE: Author's production.

Most sedimentary patches located in the southwest sector were discriminated as the Post-Barreiras Sediments (see, for instance, grey areas in Figure 5.27a). These patches were mapped in the geological maps at coarser scales, either as the Barreiras Formation or eluvial and colluvial deposits. Alternatively, some residual patches were mapped as the Post-Barreiras Sediments in the geological map of Rossetti et al. (2012) (Figure 5.29e). To better explore these discrepancies, the geomorphometric signatures of the patches were compared with the signatures of the terrain represented by the Post-Barreiras Sediments through topographic profiles (P1-P6, Figure 5.29a). The results showed that the patches are characterized by deeper valleys and

rougher hillsides, with a higher degree of relief-dissection, in contrast to the terrains related to the Post-Barreiras Sediments. However, the inner part of the patches seems to have small occurrences of these deposits, as previously recognized by Rossetti et al. (2012) and also detected with the regionalization of relief-dissection and normalized relief-dissection (Figure 5.29b-e). A good spatial agreement between the geological map and the regionalization was found for the normalized relief-dissection, revealing more contiguous segments.

Figure 5.29 - Topographic profiles derived from the sedimentary patches and the typical terrain of the Post-Barreiras Sediments, including results with regionalizations and geology.

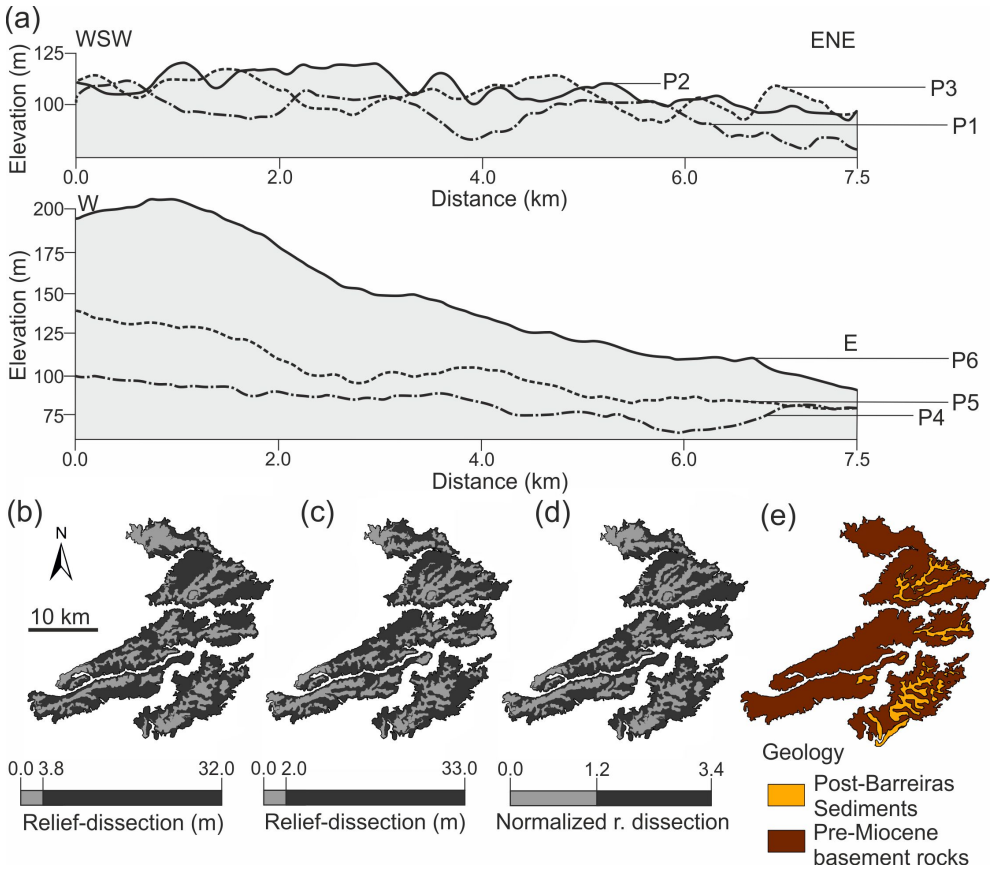

(a) The profiles were generated using a vertical exaggeration of 20 (see the location of topographic profiles (P1-P6) in Figure 5.28a). (b-d) Regionalized relief-dissection using the statistics of average (b), mode (c) and normalized relief-dissection regionalized by average (d). (e) Residuals of Post-Barreiras Sediments from the geological map of Rossetti et al. (2012), probably related to the patches (see the location of the islands in Figure 5.28d).

SOURCE: Rossetti et al. (2012).

The regionalization of the normalized relief-dissection, slope, profile curvature and relative height was suggested as the highest potential for the geological discrimination in the central sector of the study area (Figure 5.30). The regionalization of all these variables detected a higher predominance of segments related to the Post-Barreiras Sediments (grey areas), and secondarily, Barreiras Formation (dark grey areas). Visual inspections suggested that, among all the analyzed variables, the normalized slope was the most suitable for discriminating between these units. For instance, some contiguous segments related to the Barreiras Formation were identified as having high slopes along river channels and around the dome (Figure 5.30b).

Figure 5.30 - Comparison of the results obtained with the regionalization (detail level) for the central sector of the study area.

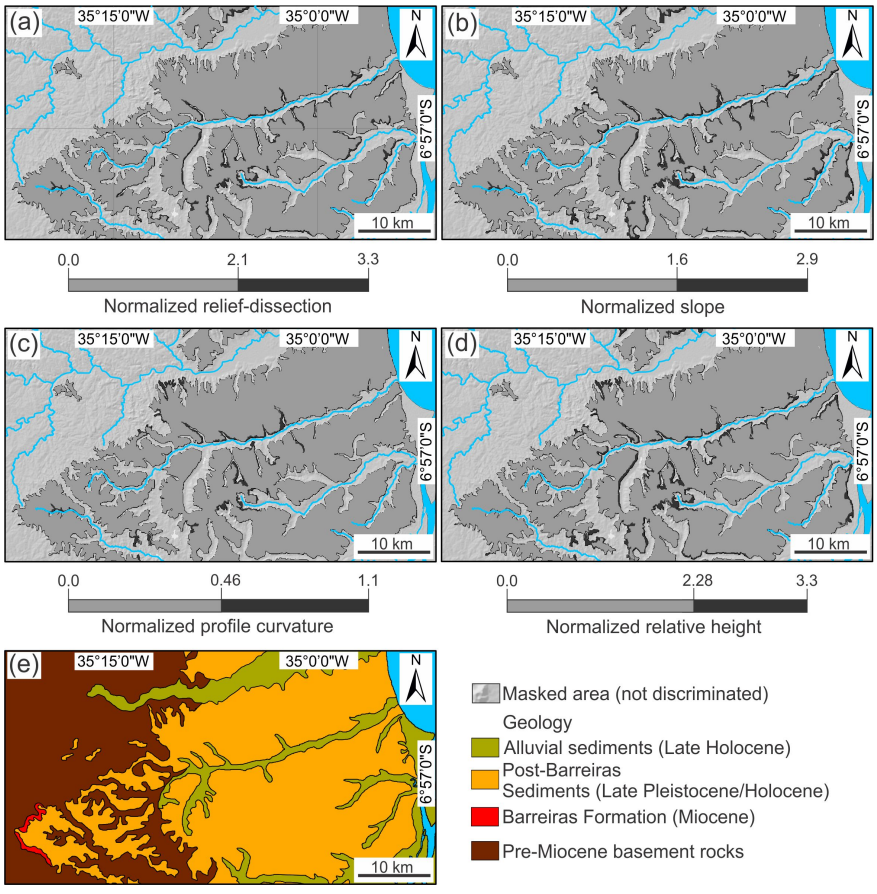

(a) Regionalization of the normalized relief-dissection, (b) slope, (c) profile curvature (absolute values), and (d) relative height. Blue lines = main drainage system. (e) Details of the geological map for this sector.

SOURCE: Geological map modified from Rossetti et al. (2012).

By testing different sizes of mapping units (e.g., from 500 to 3000 through the scale parameter) the threshold of 500 appeared as the most appropriate for generating mapping units without including artifact-related segments (see black squares in Figure 5.31). Therefore, mapping units generated with a size of 500 were used to regionalize the normalized slope. Interestingly, a small patch located in the northwest sector was identified in our results (5.31a), although it was not mapped in most previous geological maps (Figures 5.26a-b and 5.30e). This patch was classified as the Post-Barreiras Sediments in the present work. However, the morphological analysis using simple topographic profiles suggested that this patch is configured by dissected terrains compared to a typical terrain constituted by the Post-Barreiras Sediments (Figure 5.31e). In order to investigate this patch in detail, a new regionalization was carried out, but now using the topographic coherence and the mapping units derived from the grouping of spatial contiguous regions of the normalized slope. The results showed low values of topographic coherence for this patch, which are compatible with older terrains configured by a pattern of diffuse aspect. Therefore, this sedimentary patch was interpreted here as belonging to the Barreiras Formation.

The best results of the regionalization of geomorphometric variables to discriminate the sedimentary units of the northern sector of the study area were found for the relief-dissection, slope, normalized profile curvature, and relative height variables (Figure 5.32). Based on visual inspections, the normalized profile curvature showed a certain degree of spatial correspondence with the geological boundaries of the official geological maps (Figure 5.32e-f). For instance, some sectors classified as the Barreiras Formation in the geological maps were well discriminated in this product (insert boxes in Figure 5.32). In addition, the occurrence of the Barreiras Formation in the northeast portion of this sector, as recorded in both geological maps, was detected only in the normalized profile curvature product. Hence, based on the normalized profile curvature, segments related to the Barreiras Formation were characterized by higher values of profile curvature, compatible with concave and convex terrains; segments related to younger terrains (i.e., Post-Barreiras Sediments, as discriminated herein) displayed profile curvature values tending to zero, compatible with flatter terrains.

Figure 5.31 - Comparison of the regionalization of the normalized slope using different sizes of mapping units and topographic profiles derived for the patch and terrain typically classified as Post-Barreiras Sediments (see the location of the profiles P1 and P2 in a).

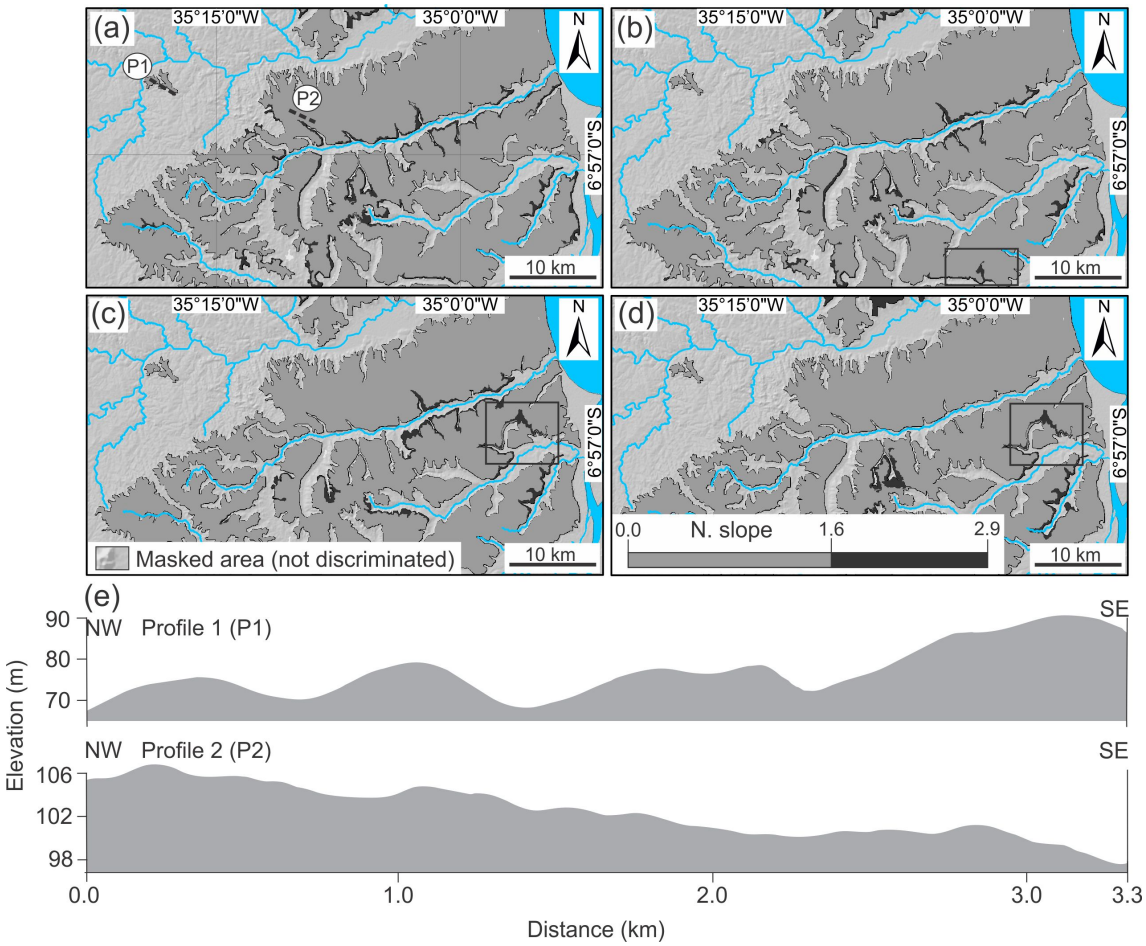

Scale parameter at the levels of 500 (a), 1000 (b), 2000 (c), and 3000 (d). The range of normalized slope was standardized for comparison. Insert box = examples of segments related to artifacts. Blue line = main drainage system.

SOURCE: Author's production.

Figure 5.32 - Comparison of the results obtained with the regionalization (detail level) for the northern sector of the study area.

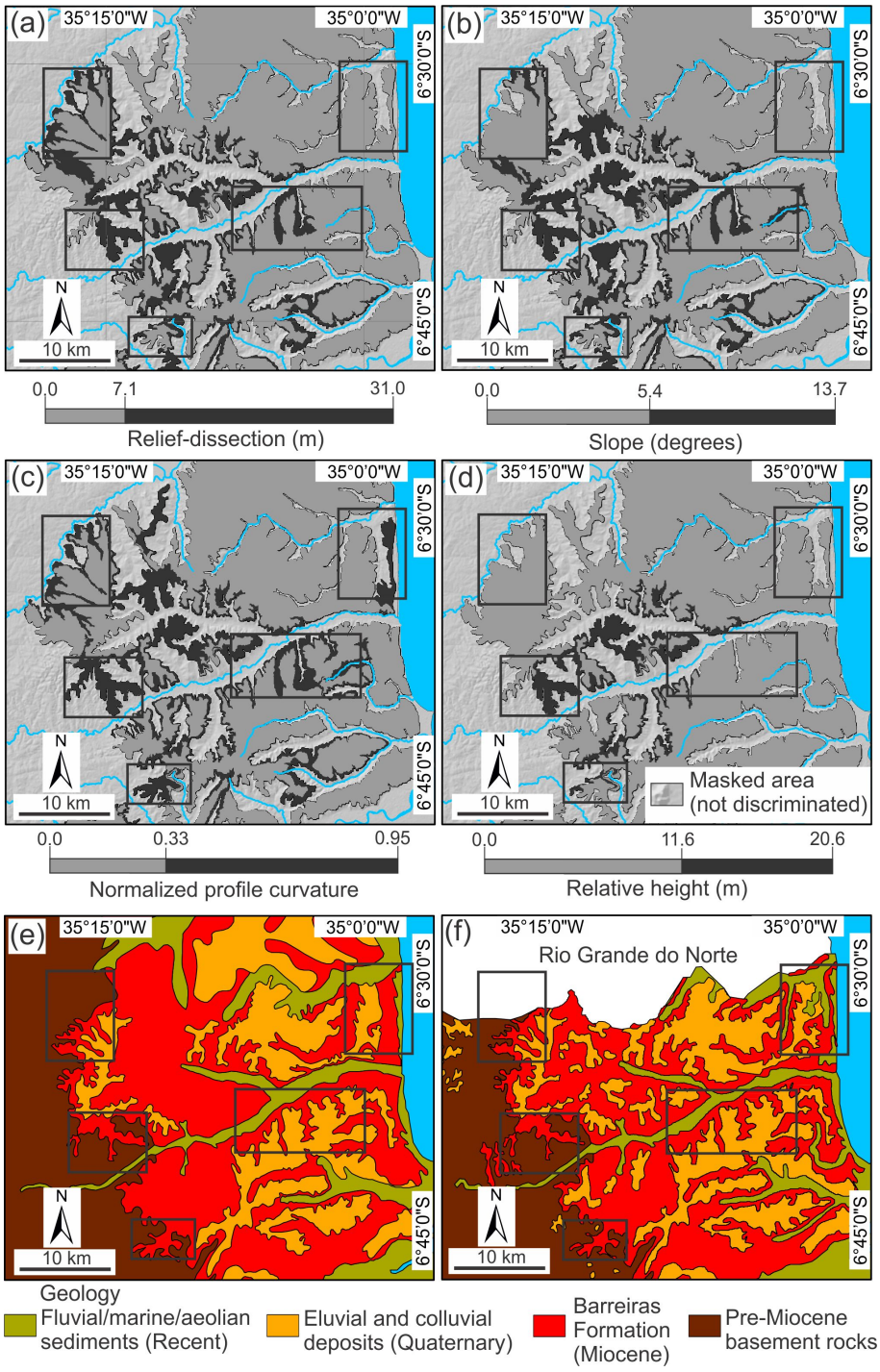

(a) Relief-dissection, (b) slope, (c) normalized profile curvature (absolute values), and (d) relative height (d). Blue line = main drainage system. (e-f) Geological maps simplified from the CPRM map at the scales of 1:1000000 (e) and 1:500000 (f). Insert box = comparative analysis between segments applying the methodology indicated in the present work and the geological boundaries of the official geological maps.

SOURCE: Geological maps modified from CPRM and Santos et al. (2002).

In order to identify the best size of the mapping units to regionalize the normalized profile curvature, a comparison was made by testing different segment sizes (Figure 5.33). This analysis showed a higher number of artifacts, including disconnected segments for mapping units with sizes smaller than 3000 (compare black squares in Figure 5.33). A good agreement in terms of spatial contiguous segments was found using mapping units with a size of 5000.

Figure 5.33 - Comparison of the regionalization of the normalized profile curvature (absolute values) using different sizes of mapping units.

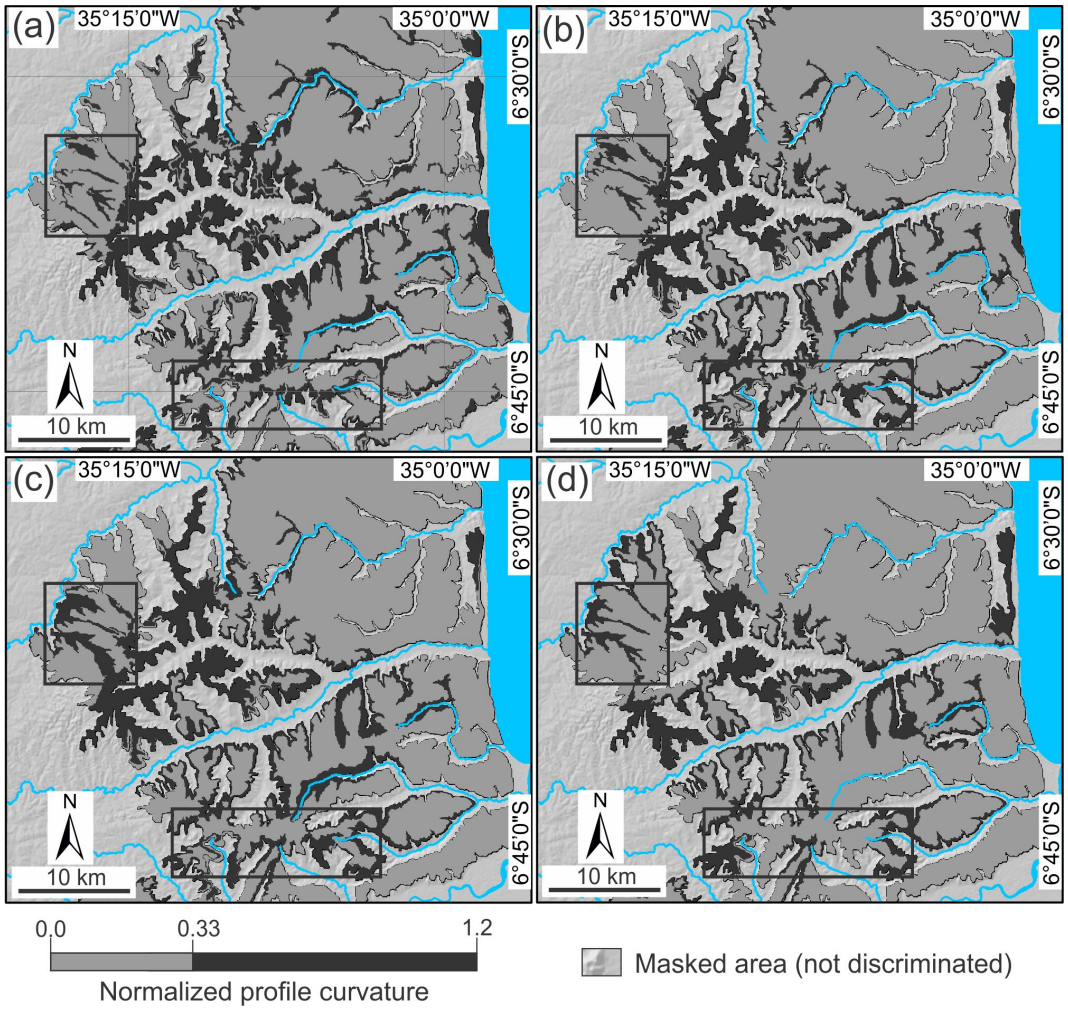

Scale parameter at levels of 500 (a), 2000 (b), 3000 (c), and 5000 (d). The range of normalized profile curvature was standardized for comparison. Insert boxes = details of artifacts and disconnected segments. Blue lines = main drainage system.

SOURCE: Author's production.

The results obtained with the geological discrimination of the study area at a detailed level is shown in Figure 5.34. In general, the results indicated: a higher degree of detail of the sedimentary units compared to the geological map in coarser scale (see, for instance, the geological map in Figure 3.2); and a good spatial agreement with the distribution of the sedimentary units mapped by Rossetti et al. (2012) (Figure 3.3). The mapped areas resulting from the geological map by Rossetti et al. (2012) and the discrimination herein were: $\sim$ 383 and 817 km^2 for the Barreiras Formation and $\sim$ 1891 and 2642 km^2 for the Post-Barreiras Sediments, respectively. Contrasting results in terms of mapped areas were expected, given different scales, methodologies, and extension of the mapped area. For example, Rossetti et al. (2012) produced a map only for the southern and central sectors of the study area. However, it is interesting to note that there is a tendency to increase the areas of Post-Barreiras Sediments towards the northern sector of the study site.

The resulting product of the geological discrimination of the southern sector of the study area was also compared with some ground truth points (see location in Figure 5.34). The overall accuracy was 80.6%, followed by the producer's accuracies of 73.4 % (omission error = 26.6 %) and 83 % (omission error = 17.0 %) for the Barreiras Formation and Post-Barreiras Sediments, respectively. The user's accuracies of 57.9 % (commission error = 42.1 %) and 90.7% (commission error = 9.3 %) were found for the Barreiras Formation and Post-Barreiras Sediments, respectively. It is important to note that the poorly classified segments occurred chiefly along the geological boundaries (compare Figures 3.2 and 5.34). In addition, there are some uncertainties in the segments classified mainly as the Barreiras Formation (question marks in Figure 5.34), compared to their distribution in the available geological maps. These areas are likely related to eroded underlying Precambrian basement rocks due to their similar geomorphometric signatures on the surface with the Barreiras Formation (see, for instance, eroded Precambrian terrain in Figure 5.25a). The record of some ground truth points of Precambrian basement rocks close to these segments supports this interpretation (Figure 4.2).

Figure 5.34 - Geological discrimination (detail level) of sedimentary units in the study area.

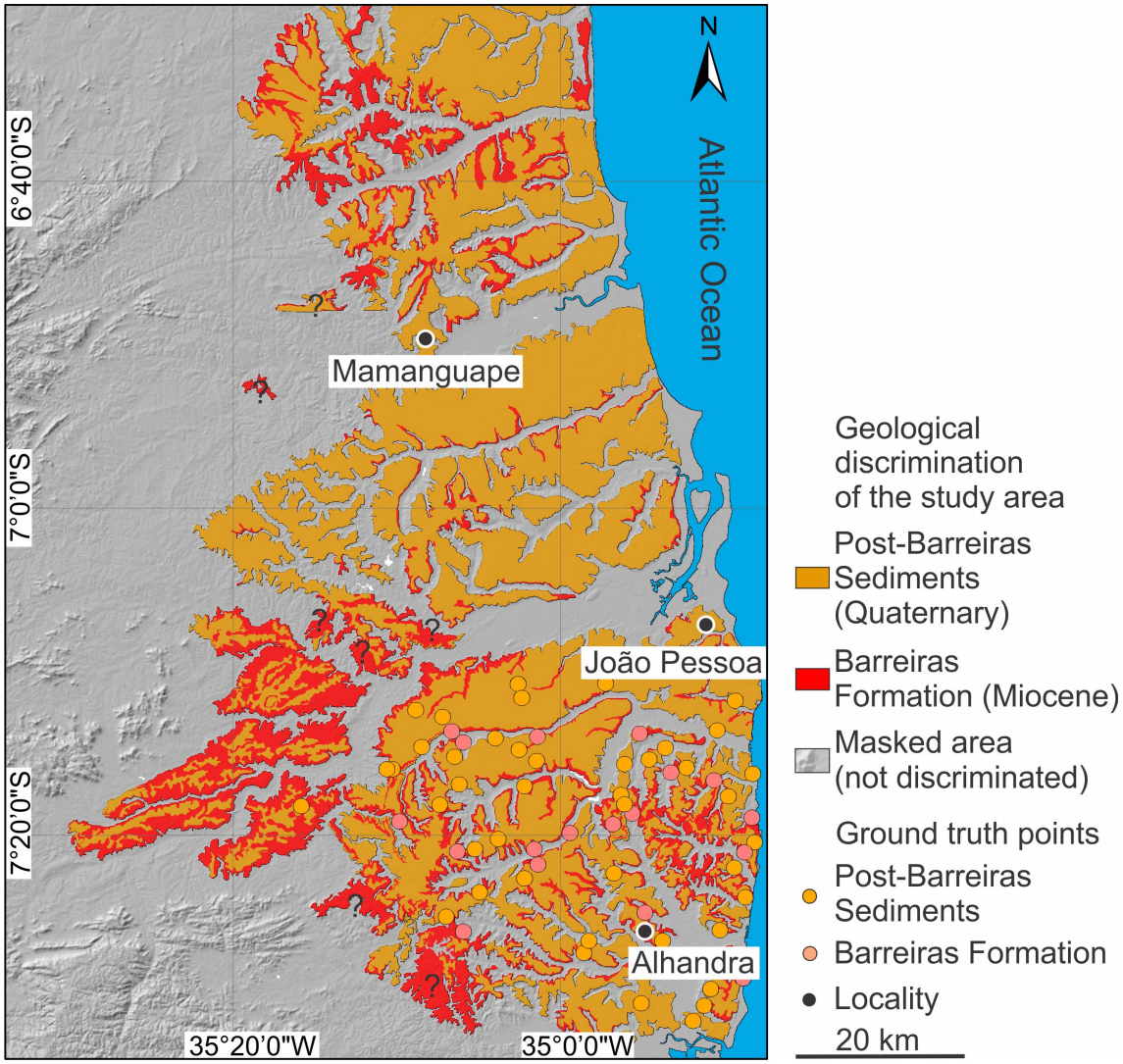

Question mark = possible classification error between geological segments. Shaded relief was derived from the SRTM-DEM.

SOURCE: Author's production.

6 DISCUSSION

The integration of all data presented in this work led to suggest that the post-rift phase of the northern Paraíba Basin resulted from faulting and folding due to basin inversion from the Miocene to the Late Pleistocene. Several evidences based on geological and geomorphological characteristics support this interpretation, as discussed in the following.

6.1 Geological evidence of neotectonics and relief inversion

The geological sections described here allow interpret that the northern sector of the Paraíba Basin was shaped by tectonic reactivation during a geological time as young as the late Pleistocene. Stratigraphic characteristics consistent with faults include the abrupt changes in the thicknesses of the geological units within short distances around the Camaratuba, Mamanguape, and Paraíba river valleys, which reveal grabens formed by the displacement of normal faults of Late Quaternary age (Figure 5.7a).

The tectonically-controlled relief model suggested for the study area is consistent with geological data available from the central and southern sectors of the Paraíba Basin, which showed an abundance of faults and folds (BRITO-NEVES et al., 2004; BEZERRA et al., 2008; BRITO-NEVES et al., 2009; ROSSETTI et al., 2011a; ROSSETTI et al., 2011b; BEZERRA et al., 2014). These areas record fault and fold-related structures, for instance, with broad anticlines and synclines in Miocene and even late Pleistocene deposits especially around the Gramame River basin (Figures 5.7b-c, 5.8, and 5.9). Taking this structural context into account, and also considering the morphological and geological evidence of tectonic control in the study area, it seems reasonable to suggest that the dome-like relief described resulted from folding.

The relief controlled by faults and folds in the northern Paraíba Basin is compatible with tectonic deformation, including extension and compression. These deformation styles are consistent with the strike-slip regime proposed for the region (BRITO-NEVES et al., 2004; BEZERRA et al., 2008; BEZERRA et al., 2014; LIMA et al., 2017). The orientation of the structures according to regional structural trends of northeastern Brazil indicates deformation resulting from the reactivation of pre-existing weakness zones from the Precambrian shear zones. There has been an increasing number of publications demonstrating tectonic reactivation, including folding, in several other areas of northeastern Brazil (ROSSETTI et al., 2011a; ROSSETTI et al., 2011b; GURGEL et al., 2013; BEZERRA et al., 2014; MAIA; BEZERRA, 2014; MARQUES et al., 2014;

NOGUEIRA et al., 2015; LIMA et al., 2017; VASCONCELOS et al., 2019b; VASCONCELOS et al., 2020). The position of Miocene and Quaternary sedimentary deposits associated with faults and folds at a higher position than the basement rocks might indicate that the northern Paraíba Basin was also inverted through time from an original depression to the present-day domic relief.

Additional morphological characteristics consistent with the tectonic origin of the dome-like relief in the northern Paraíba Basin include: the Quaternary relief with arched, convex-up shape having altimetry higher than the adjacent Precambrian basement terrains (Figure 5.4a); the recurved channels featured in the radial to recurved trellis patterns; and the higher topographic location of the Barreiras Formation relative to the basement rocks, particularly in the Gramame River basin. Similar features were also observed in other important sedimentary basins of NE Brazil (MAIA; BEZERRA, 2014; MARQUES et al., 2014; NOGUEIRA et al., 2015; VASCONCELOS et al., 2019b; BEZERRA et al., 2020; VASCONCELOS et al., 2020). Taking this structural context into account, we attribute the succession of alternating low and high terrains, also recorded in the Gramame basin (Figure 5.2a-c), as a product of combined episodes of post-rift normal faulting, and tectonic inversions, including foldings, an interpretation supported by the geological evidence.

Independent works using a variety of methods to infer rock uplift rates suggest that several passive margins worldwide record increased rock uplifting rates long after the rifting phase, such as the passive margins of West Greenland, SW Africa, SE Australia, and NE Brazil (PEDOJA et al., 2011; JAPSEN et al., 2012b; GANDINI et al., 2014; TRIBALDOS et al., 2017). These studies contrast with geomorphological models of elevated, passive continental margins, as they are based on assumptions of passive margins as permanent highlands; c.f., Japsen et al. (2012b) and references therein. For instance, Tribaldos et al. (2017) found increased uplift rates during the last ∼30 Ma in the Borborema Province, westward sector of the study area (Figure 6.1), based on inverse modelling of river profiles. These authors found a peak of rock uplift for the middle Miocene, followed by a drop in the curve and then an increase in rock uplift rates from the Pliocene onwards. In addition, Pedoja et al. (2011) using a compilation of paleoshoreline data worldwide, also suggested that most coastal segments have risen relative to sea level since the last interglacial stage (∼122 ka), with an average global uplift rate of ∼0.2 mm/yr, and of ∼0.1 mm/yr for the Brazil's northeast coast. Further evidence of rock uplift in NE Brazil after the Early Cretaceous include: the occurrence of shallow marine limestones of the Santana Formation (Albian) at present-day elevations of 700-800 m asl higher than

the surrounding Precambrian basement in the Araripe Plateau in the centre of the Borborema Province; the Serra dos Martins Formation, with elevations up to 920 m asl higher than the Precambrian basement in the eastern Borborema Province (MORAIS NETO et al., 2009; JAPSEN et al., 2012b). In the Paraíba Basin, the record of shallow marine deposits of the Post-Barreiras Sediments $\sim$ 38 m asl is also coherent with basin uplifting (GANDINI et al., 2014).

Figure 6.1 - Average predicted uplift rates for the Borborema Province in northeastern Brazil and palaeoelevation estimates for the central Andean plateau.

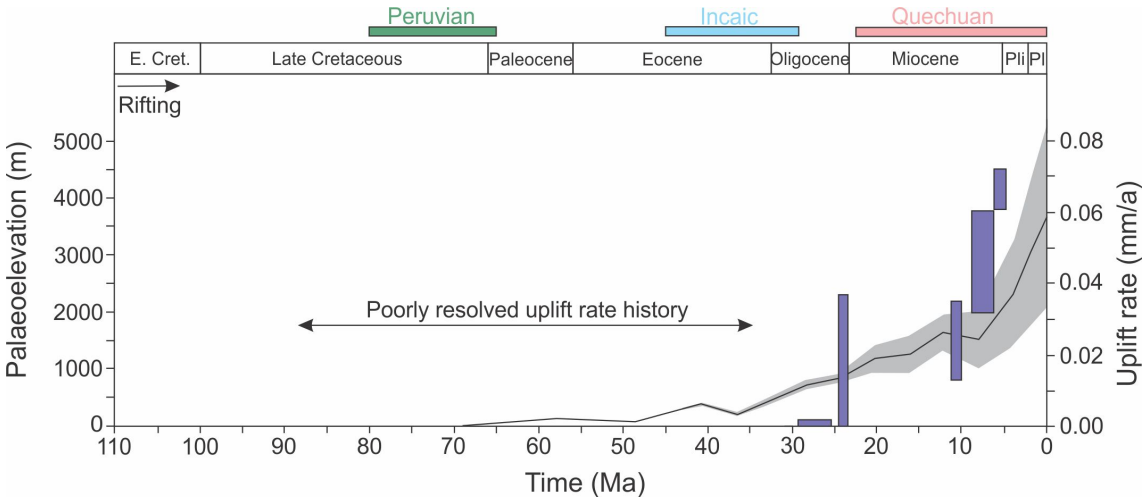

Black line and grey area with ± 1 error band = average predicted uplift rates over the last $\sim$ 70 Ma based on inverse river profile modelling (TRIBALDOS et al., 2017). Purple bar = palaeoelevation estimates (vertical axis to the left) over the past 30 Ma based on carbonate oxygen isotopes (GARZIONE et al., 2008). The main phases of Andean orogeny are also indicated above the diagram (i.e., Peruvian: 80-65 Ma, Incaic: 45-28 Ma and Quechuan: 22-0 Ma)(COUTAND et al., 2001).

SOURCE: Coutand et al. (2001), Garzione et al. (2008) and Tribaldos et al. (2017).

There is no general agreement concerning the mechanisms that led to the regional uplifting of passive margins worldwide. Some hypotheses have been presented, such as mantle forcing (COX, 1989; GALLEN et al., 2013; KLÖCKING et al., 2020) or increased lithosphere compression. Lithosphere compression induces widespread deformation and may favour the uplifting of passive margins (LEROY et al., 2004; PEDOJA et al., 2011). Several recent works have interpreted tectonic deformation related to intraplate compression due to the combined pushes of the Mid-Atlantic Ridge (towards

the W) and the Andes (towards the E) during the post-rift stage in northeastern Brazil (MARQUES et al., 2014; NOGUEIRA et al., 2015; VASCONCELOS et al., 2019b; BEZERRA et al., 2020; VASCONCELOS et al., 2020). Far-field compressive stresses are suggested to be the main mechanism (see Vasconcelos et al. (2020) for a discussion) which led to the tectonic inversion of the sedimentary basins in this region, such as the Potiguar (MAIA; BEZERRA, 2014; BEZERRA et al., 2020), Sergipe-Alagoas (VASCONCELOS et al., 2019b), Rio do Peixe (NOGUEIRA et al., 2015; VASCONCELOS et al., 2020) and Araripe basins (MARQUES et al., 2014)(Figure 3.1).This interpretation agrees with the main present-day ~ E-W-oriented maximum compressive stress field documented in NE Brazil and also in the Andes (BEZERRA et al., 2014; ASSUMPÇÃO et al., 2016). There are other areas worldwide with similar reliefs related to basin inversion (ALEXANDER, 1988; AMIT et al., 1999; TURNER; WILLIAMS, 2004).

The age of the tectonic inversion in northeastern Brazil is an issue open to debate. However, the folding of the Post-Barreiras deposits attests to the young age of this event in the study area, i.e., during or after the deposition of this unit in the late Pleistocene. If there was an event of uplifting between this time and the deposition of the Barreiras Formation in the Miocene is an issue that remains to be investigated. Events of tectonic inversion by intraplate compression in South America have been linked with the three main phases of Andean tectonism (GARZIONE et al., 2008): Peruvian (80-65 Ma), Incaic (45-28 Ma) and Quechuan (22-0 Ma) (COUTAND et al., 2001). Therefore, independent if Miocene or late Pleistocene in age, the uplifting recorded in the study area matches with the Quechuan event, which is marked by a particularly high Andean topographic growth (GARZIONE et al., 2008) (see palaeoelevations in Figure 6.1).

6.2 Morphology and geomorphic indices

The morphological characteristics of the study area are compatible with a tectonically-controlled relief. For instance, the drainage network dominated by trellis pattern and subtypes, developed on Miocene and late Pleistocene-Holocene deposits, is compatible with this interpretation. Similar patterns were documented in various geological terrains controlled by faults and/or folds (HOWARD, 1967; DEFFONTAINES; CHOROWICZ, 1991; PÉREZ-PEÑA et al., 2010). In the absence of any significant lithological variation, the drainage network with radial to recurved trellis patterns around the dome-like reliefs, as recorded in the Mumbaba, Mamuaba, Dois Rios, Curralinho, Una, and upper Miriri rivers (Figure 5.4c-d), reinforces the proposed tectonic influence on the shaping of the modern relief of the northern Paraíba

Basin.

The asymmetric sub-basins of the dome-like relief (Table 5.1 and Figure 5.4) also suggest tectonically-molded landforms (HARE; GARDNER, 1985). The asymmetrical sub-basins, characterized by rivers with high to moderate AF index values in the central and southern sectors of the study area, are attributed to greater tectonic influence than the symmetric or nearly-symmetric sub-basins from the northern sector. DEM-based analyses of the drainage asymmetry helped to recognize tectonic activity in many other river systems (El HAMDOUNI et al., 2008; SCOTTI et al., 2014; OWONO et al., 2016). The anomalous sub-basins marked by a NW, and secondly SE, tilting pattern in terrains dominated by late Pleistocene-Holocene deposits may be related to the reactivation of ENE-WSW tectonic structures in northeastern Brazil (BRITO-NEVES et al., 2004; BRITO-NEVES et al., 2009; BEZERRA et al., 2014) (Figures 3.1 and 5.10). The reactivation of faults with similar orientations was also proposed for the region around the Paraibinha, Mamuaba, and Mumbaba rivers, where late Pleistocene tectonic deformation affected the Cariatá Graben (BEZERRA et al., 2008). The SW tilting of sub-basins located in terrains of young sedimentary deposits is related to NW-striking faults. Such structures were previously recognized by subsurface and field data south of the study area (BRITO-NEVES et al., 2004; BEZERRA et al., 2008; BRITO-NEVES et al., 2009).

The analysis of elevation curves provided by the swath topographic profiles recorded an asymmetric relief over late Pleistocene-Holocene deposits containing the dome-like structures (Figure 5.1). The differences in elevation curves between the crystalline basement and the sedimentary terrains could be explained by differential erosion. For instance, the low-lying terrains developed over more eroded basement rocks could be explained if one considers their longer exposure time to a larger number of tectonic events compared to the relatively more preserved sedimentary deposits of the Paraíba Basin (see also section 6.4 for a discussion). However, contrasting elevation curves in a homogenous sandy unit (e.g., PB1; compare Figures 3.3 and 5.1) conforms to the proposed tectonic control. That is the case of the marked differences in elevation curves along the Miriri River, located entirely over the Post-Barreiras Sediments. The base level lowering of the entrenched tributaries near the dome-like relief in this sector (see profile 5 in Figure 5.1) is also consistent with a tectonic control, an interpretation that agrees with the high THi^* index values around this structure (grey curves in Figure 5.3). High hypsometric index values were also related to tectonically-influenced terrains elsewhere (El HAMDOUNI et al., 2008; MAHMOOD; GLOAGUEN, 2012; ANDREANI et al., 2014; SCOTTI et al., 2014;

PÉREZ-PEÑA et al., 2017). In addition, high relative relief values closer to these domes (black curves in Figure 5.3) indicate higher fluvial incision rates, which is compatible with the establishment of drainage networks as a response to tectonics. Similar variations in relative relief have generally been attributed to fluvial incision (TELBISZ et al., 2013; ANDREANI et al., 2014; SCOTTI et al., 2014; PÉREZ-PEÑA et al., 2017) or river erosion under the tectonic influence, considering almost constant climatic conditions (BURBANK, 1992).

The divergence in longitudinal profile shapes detected in the cluster analysis based on H_{max} (Figure 5.5) is attributed to local changes in lithology because rivers with anomalous curves and ungraded longitudinal profiles (i.e., group 1) were located in areas with contrasting lithologies (i.e., sedimentary deposits in contact with Precambrian rocks). However, low H_{max} values recorded for the most asymmetric rivers (e.g., Dois Rios -11, Curralinho -12, Una -14, and Mumbaba -18 rivers in Figure 5.6) located over sedimentary deposits are consistent with transitional or adjusting rivers (according to criteria presented by Demoulin (1998)). Such interpretation is consistent with the proposed tectonic control for the studied fluvial systems.

6.3 Interpretation of knickpoints

6.3.1 Behaviour and formation

Vertical-step knickpoints may have resulted from local differences in bedrock erodibility, as the majority occurred at or close to lithological boundaries. However, some of these knickpoints showed an increase in k_{sn} downstream river profiles, which may suggest combined lithological and base level effects, as observed elsewhere (BOULTON et al., 2014). In addition, most vertical-step knickpoints (e.g., from rivers 6, 7, 15, 19, and 20; Figures 5.12 and 5.13a) occurred below the slope-break knickpoints at a certain distance from the steepened stretches. Such characteristics may be recording feedbacks in the river incision process (BERLIN; ANDERSON, 2007).

A lithological control may have influenced the prevalence of slope-break knickpoints in steep and elevated terrains of Precambrian basement rocks (Borborema Province) of high-resistance to erosion (Figure 5.14b). However, with a few exceptions, the changes in k_{sn} values do not appear to be related with a lithological control, neither with climate, as precipitation rates do not vary significantly in this sector of northeastern Brazil (CARVALHO et al., 2020). The highest k_{sn} values did not occur locally, as they were observed over a large area of the Precambrian basement. Higher k_{sn} values were also present around the domic reliefs in the sedimentary terrains, where

slope-break knickpoints were recorded. In addition, higher k_{sn} values downstream than upstream of the knickpoints in relatively uniform lithologies (see the distribution of rock groups in Figure 5.13a) is typical of slope-break knickpoints, which are related to base level changes. In contrast, vertical-step knickpoints are commonly related to bedrock resistance (KIRBY; WHIPPLE, 2012). The high scaling behaviour between k_{sn} and relative relief of the slope-break knickpoints also suggests transient fluvial incision (Figure 5.14a).

When the horizontal components of knickpoint retreat were analyzed, the distance from the mouth and distance from the divide scaled with the drainage area, showing high correlations ($r^2 > 0.89$). This suggests that the slope-break knickpoints of the study area are mobile and not anchored in place, a finding in agreement with several other studies that showed knickpoint retreat as primarily a function of drainage area (CROSBY; WHIPPLE, 2006; BERLIN; ANDERSON, 2007; BOULTON et al., 2014; KENT et al., 2017). The fact that the slope-break knickpoints of the study area show a wide range of upstream drainage areas (i.e., from 2.4 to 238 km^2) confirms that they are not pinned to a specific drainage area threshold. The most likely is that the studied knickpoints are actively migrating upstream (Figure 5.16). Similar migratory slope-break knickpoints were identified in the southern Appalachians, passive margin of Eastern North America (GALLEN et al., 2013).

The exponents derived from the power-law scaling between drainage area and horizontal components of knickpoint retreat were also compared with the Hack's law ($L = 1.4A^{0.6}$) (HACK, 1957). Theoretically, when the hack exponent is larger than 0.5, the basin tends to become narrower and more elongate as its size increases (HACK, 1957). After Hack's work, several studies were performed to test the validity of his law, and exponents varied from area to area, but in general were found at the range of 0.4-0.8 (SMART; SURKAN, 1967; MUELLER, 1972; RIGON et al., 1996; WILLEMIN, 2000). In the case of the study area, the Hack's law is only applicable for the southern knickpoints (h exponents = 0.56-0.58), although statistical differences in the medians of drainage basin areas of the two sets of knickpoints were not found (Table 5.3). The higher Hack's exponents in the northern knickpoints (0.62-0.77) may be related to the high sinuosity downstream of some large tributaries (e.g., rivers 5 and 6 in Figure 5.10), which could have inflated part of the deviation of Hack's exponent (SMART; SURKAN, 1967; WILLEMIN, 2000). However, given that the Hack's exponent may vary due to a combination of several factors (SMART; SURKAN, 1967; MUELLER, 1972; RIGON et al., 1996; WILLEMIN, 2000), its interpretation aiming to help understanding the behaviour of the knickpoints in the study area is not

conclusive at this time.

Slope-break knickpoints are also interpreted to propagate upstream at constant vertical rates, so they should occur at similar elevations (NIEMANN et al., 2001). The wide range of elevations of the mobile slope-break knickpoints found on Precambrian basement rocks and sedimentary deposits (i.e., from 65 to 676 m asl) shows that this is not the case in the study area. Knickpoint elevations showed weak correlations with the horizontal component of knickpoint retreat and total drainage area when analyzed together (Figure 5.15a-b). The weak correlation of knickpoint elevation with the horizontal component of knickpoint retreat and the total drainage area, as well as the discrepancies in the statistical analyses (i.e., positive and negative linear relationships of the northern and southern sectors, respectively), may suggest: (i) two clusters of knickpoints with distinct formation; or (ii) a natural variability as a result of a single knickpoint formation, as often observed in several other landscapes (CROSBY; WHIPPLE, 2006; BERLIN; ANDERSON, 2007; BOULTON et al., 2014; KENT et al., 2017).

Knickpoints standing at similar elevations are generally rare due to several factors that can disperse the elevations during the knickpoint retreat (e.g., spatial variations in rock uplift rates and absence of an earlier steady-state (KIRBY; WHIPPLE, 2012; WHIPPLE et al., 2013; BOULTON et al., 2014). The differences between the means of relative relief (radius = 3000 and 5000 m) of the two sets of knickpoints indicated by the T-test (Table 5.3) were expected, given the topographic particularities between the two sectors analyzed here (Figure 5.16). In addition, the increase in the size of the moving window may have somehow affected these results. Therefore, based on the topographic particularities of the study site and the results with the statistical tests using several knickpoint attributes, we interpret that the lowest knickpoints in each river came from a single event of knickpoint formation. Some uppermost knickpoints, as recorded in the rivers 5 and 6, may be related to an earlier transient response of the relief, as they almost migrated through the fluvial system.

Based on the foregoing discussion, the most likely is that the relief of the study area is in a transient state of adjustment, with incisive channels being still adjusting to the new boundary conditions.

6.3.2 Control on knickpoint development

Under relatively uniform climatic conditions, the development of knickpoints may record changes in bedrock erodibility, river capture events, sea level fall and/or

increase in rock uplift rates (KIRBY; WHIPPLE, 2012). As discussed above, lithological control may have influenced the development of the knickpoints of the study area, but it is unlike that the base level lowering of the studied rivers and the mobile knickpoints were triggered by contrasts in bedrock erodibility. Concerning the river capture, only one ongoing river capture was observed in the study area based on the morphological investigation (Figure 5.17b). Significant changes in river dynamics will be expected in this region once this river capture is completed, for instance, with the abandonment of the uppermost tributaries of the Miriri River and the transfer of flow from the Miriri to the Paraíba river basins. However, it is important to note that this river capture is an isolated event, with no correspondence with the slope-break knickpoints. Therefore, this river capture cannot justify the changes in the base level of the tributaries throughout the study area.

The potential influence of eustatic sea level falls is viable, particularly during the last glaciation maximum, when a drop of several tens of meters is advocated (SHACKLETON, 1987). Despite this possibility, which remains to be investigated in future works, the lowering of the base level of the studied rivers seems to have had a tectonic contribution. This proposal conforms to the record of shallow marine deposits of the Post-Barreiras Sediments $\sim$ 38 m asl, as discussed in section 6.1. The uplifting of these deposits is coherent with the average incision of $\sim$43 m recorded for rivers flowing over Miocene and Late Quaternary deposits (Table 5.2). Although the statistical relationships, i.e., between k_{sn} and uplift/incision is not always linear; e.g., Kirby and Whipple (2012), and references therein, we found a trend of stepper channels, with higher incision and elevation values toward the Borborema Province edges (Table 5.2 and Figure 5.14b), suggesting increased rock uplift rates in this sector. This was an unexpected result, considering that the rocks in this province have a higher resistance to erosion than the sedimentary basin. This inconsistency can be resolved if one considers a tectonic control on the development of these channels. Considering the geological context proposed for the study area, which includes uplifting, then a pulse of rock upwarping could have triggered the lowering of river base levels, the propagation of knickpoints upstream along the river profiles and the topography rejuvenation. The onset of knickpoint formation is related to the Miocene because slope-break knickpoints were also found over Miocene deposits (Figures 3.2 and 5.13a), although a younger event of knickpoint formation is not ruled out (see discussion in section 6.4). In fact, the response to fluvial perturbations generally has a delay in the order of 1–5 Ma (WHITTAKER; BOULTON, 2012).

Considering the geological discussion presented in topic 6.1, the uplift responsible

for the decrease in the river base levels and knickpoint propagation is related to far-field compressive stresses, although some form of mantle-related dynamic processes may have also played a role. The brittle reactivation of some known tectonic structures in the study area, such as the major normal faults bounding the Cariatá Graben margins and the Patos shear zone, could have formed the slope-break knickpoints recorded in this work (Figure 5.16). This is suggested by the proximity of the knickpoints to these faults and the knowledge that these structures were reactivated several times long after the rifting phase, including a youngest event in the Quaternary (BEZERRA et al., 2008; MARQUES et al., 2014; NOGUEIRA et al., 2015). The invoked correspondence between the slope-break knickpoints and the faults/shear zones of the study area needs to be better investigated in the future.

6.4 Significance and implications of divide migration

Most drainage network and river basins in the study area did not show many topological and geometric changes in the χ-map and Gilbert metrics, despite that the tributaries are increasing the incision rates. The mobile divide segment recorded on Miocene and Quaternary deposits in the northeast sector of the study area (D8 in Figures 5.17a and 5.18) can reflect either local differences in bedrock erodibility or topographic contrasts due to the influence of the domic relief. A definitive interpretation is difficult because the cross-divide differences were detected only on two of the three Gilbert metrics. In contrast, the mobile divide segments recorded in the southeast sector (i.e., D2 and D3) showed cross-divide differences in both metrics (Gilbert metrics and χ-map). Thus, they were used to analyze the dynamic evolution of the studied relief. These divides migrated to the southeast (D2) and northeast (D3), following a high-elevation, chevron-shaped plateau on Precambrian basement rocks that is capped by less resistant Miocene-Quaternary deposits (Figures 3.2 and 5.17). Therefore, lithological control by differences in bedrock erodibility may have driven the divide migration in this region.

In addition to the geological configuration, the topographic expression of the chevron-shaped plateau characterized by a high elevation and tilted surface of a dissected thin sedimentary cover is comparable with those in the Shillong Plateau, NE India (STRONG et al., 2019). This plateau was related to lithological control due to a re-exposed paleosurface, an interpretation based on numerical modelling of erosion (soft rocks over hard rocks) presented by Forte et al. (2016). Therefore, one hypothesis to explain the origin of this plateau may be the exhumation of a basement paleosurface.

Alternatively, there are topographic and geological evidences suggesting that the plateau may not have formed primarily by lithological control, which include: Miocene-Quaternary deposits capping the plateau at higher elevations (i.e., up to 200 m asl) than the adjacent low-lying Precambrian rocks (Figure 5.16); and the dome morphology to the east located at the same altitude as the plateau, but occurring in homogeneous Quaternary deposits. These characteristics suggest a young (i.e., Quaternary) regional event of uplifting, which would have raised the basement rocks and the overlying sedimentary deposits. This event was followed by fluvial incision, which dissected part of the plateau and the domic morphologies. Previous works in the Borborema Province had already suggested an increase in uplifting rates during the Quaternary (PEDOJA et al., 2011; TRIBALDOS et al., 2017) (Figure 6.1). A point of interest here is that topography rejuvenation, driven by uplifting, could have set the formation of the knickpoints in the study area. However, uplift alone could not explain the differential erosion among the studied geological sectors, such as the eroded, low-lying Precambrian basement rocks west of the plateau and the relatively preserved sedimentary units to the east. This geological context might have resulted from the long exposure of the Precambrian rocks of the Borborema Province to tectonic events, some pre-dating the establishment of the Paraíba Basin (e.g., Brasiliano/Pan-African orogeny). The intensive fracturing caused by these events would have facilitated erosion. In addition, the Precambrian basement is drained by large fluvial systems, presumably with a higher potential of erosion than the smaller and thus less erosive rivers that flow on the sedimentary terrain.

6.5 Efficiency of geomorphometry and regionalization for geological discrimination

The 30 m spatial resolution SRTM-DEM succeeded in quantifying the studied relief based on the derivation of a set of regional and local geomorphometric variables. The manipulation of these variables based on regionalization techniques was useful to discriminate the geological terrains at general and detailed levels. The results lead to recommend the combination of various geomorphometric variables to describe relief features aiming to discriminate geological terrains. The central sector of the study area was the most challenging region in terms of geological discrimination, which required a higher number of regionalizations (Figure 5.23). For instance, the domic morphology of the Paraíba Basin at high elevations had a relatively similar geomorphometric response compared to the high elevation Precambrian basement to the west. The geomorphometric similarity in terrains with different rock types

may have produced the misclassification of segments in this and other areas studied in the Paraíba Basin (see question marks in Figure 5.34).

Apart from the topographic and lithological particularities of the study area, the regionalization also varied according to: the selection of geomorphometric variables; the definition of mapping units; and the selection of proper thresholds to individualize terrains with different geomorphometric signatures. Several works have tested a variety of geomorphometric variables for geomorphological and geological discrimination of various reliefs (DRĂGUŢ; BLASCHKE, 2006; MILIARESIS et al., 2009; VALERIANO; ROSSETTI, 2011; ANDRADES-FILHO et al., 2014; VALERIANO; ROSSETTI, 2017; GERENTE et al., 2018; MOREIRA, 2018). However, only a few variables showed potential to perform this type of analysis. For instance, from a total of 74 geomorphometric variables, Moreira (2018) found that only 12 were suitable to perform the geomorphometric characterization of basins in southeastern Brazil, including slope, elevation and hypsometric integral. These three variables, together with topographic coherence and valley depth (Tables 5.5 and 5.6), were also the most valuable for the regionalization in the study area. In addition, the variable valley depth helped to define the first set of mapping units, producing homogeneous and meaningful terrain patches after several segmentation tests. However, a considerable number of sedimentary areas along river valleys were not preserved using this variable. Therefore, this variable must be used carefully, especially when the geological discrimination includes sedimentary terrains.

The Box-Cox and arctangent normalization techniques tested here were useful to minimize outliers and reduce the skewed distribution shapes of the original variables (Figure 5.19). The visual quality (not shown here) of the normalized variables showed an apparent improvement in terms of brightness and contrast, as the frequency distribution and statistics of the original variables changed after normalization, with a quasi-normal distribution. The original range of profile curvature, for instance, was expanded after normalization by the arctangent method, with a substantial enhancement of terrain features. This procedure helped to better define cut thresholds for the geological discrimination at the detail level (Figure 5.32). In addition, the application of normalization techniques for statistical purposes (e.g., parametric statistical analysis) is desirable. However, a word of caution must be made when using normalization techniques in topographic analyses because the geomorphometric significance of a given variable may change when its original distribution is modified.

The results with the regionalization techniques are also strongly dependent on the

size of the mapping units. The size of a mapping unit is not universal, but it varies from area to area, from method to method, and from data to data (scale-dependent parameter). Segmentation technique is the most used method to generate mapping units (VALERIANO; ROSSETTI, 2017; GERENTE et al., 2018), but other approaches, such as those using watersheds (MOREIRA, 2018), or regions defined under some geomorphometric criteria, have also been used for this purpose. Therefore, experiments to define mapping units are still required. Here, the mapping units derived from segmentation using valley depth had size units varying from 1000 to 5000 and from 500 to 5000 at the general and detail levels, respectively. It is important to note that we observed a south to north increase of the size of mapping units in the study area. The increased size of mapping units to the north may be related to the relatively more homogeneous geomorphometric signals of this sector, which allowed to generate larger terrain patches through segmentation techniques.

The partition of the study area in three sectors, attempting to have a better control of data manipulation, was efficient. This included the establishment of specific thresholds to define mapping units and regionalizations. However, the selection of thresholds to discriminate geological terrains was subjective, being based on the visual interpretation of variables and histograms. Future works based on data mining-related techniques and machine learning algorithms may help to better define thresholds and to automate the geomorphometric characterization, respectively.

The methodology established here for the geological discrimination of the northern Paraíba Basin by geomorphometry has the potential to generate cartographic products in scales up to 1:250.000. This conclusion was obtained comparing the results obtained in this work with information from pre-existing geological maps (SANTOS et al., 2002; ROSSETTI et al., 2012) (figures 3.2, 3.3, 5.26, and 5.34). In addition, quantitative analysis based on the calculation of accuracy measures also showed that the results with the detailed geological discrimination are reasonable (overall accuracy = 80.6%), although a limited set of ground truth points was used. This is especially the case of the sedimentary terrains developed over the Post-Barreiras Sediments (producer's accuracies = 83 % and user's accuracies = 90.7%).

Previous work had already proposed the generation of a geological map for the central Paraíba Basin by the combination of geomorphometry and geophysics (ANDRADES-FILHO et al., 2014). However, the application of geomorphometry for the detailed geological discrimination of the northern sector of this basin is presented here for the first time. The higher occurrence of the Barreiras Formation to

the south in the resulting geological discrimination product (Figure 5.34), and the increased thickness of this unit in this sector (see thicknesses of geological units in Figure 5.7a) may suggest its location in the Paraíba Basin depocenter.

7 CONCLUSION

a) The morphological analysis of the drainage network and the application of geomorphic indices derived from the SRTM-DEM data succeeded in unraveling the tectonic control of the northern Paraíba Basin. This approach has the potential to help the investigation of tectonics in other reliefs where the scarcity of geological exposures makes a direct investigation of structures troublesome, as in the case of the study site.

b) In this work, geomorphic indices and swath profiles helped to characterize arched, convex-up dome-like reliefs in the northern Paraíba Basin. These morphologies were related to folds formed during the uplifting that followed the deposition of the Post-Barreiras Sediments in the late Pleistocene.

c) The rivers investigated in this work are not in a steady-state condition. On the contrary, they were characterized by transient profiles bounded by slope-break and/or vertical-step knickpoints. Slope-break knickpoints are mobile, because they recorded a range of drainage area thresholds upstream of the knickpoints. This knickpoint behavior confirmed that the knickpoints are still adjusting to the new boundary conditions. A single event of knickpoint formation of Miocene is interpreted here by the record of slope-break knickpoints on Miocene deposits, although a younger event of knickpoint formation is not ruled out.

d) Mobile slope-break knickpoints and river segments with increased normalized steepness index (k_{sn}) were recorded mainly toward the Precambrian basement of the Borborema Province. This region also recorded the highest knickpoint elevation and incision values, in agreement with recent studies suggesting that the Borborema Province and the adjacent Paraíba Basin have documented increased uplift rates since the Miocene (Quechuan phase). The slope-break knickpoints formed as a result of base level lowering of rivers were interpreted here due to far-field compressive stresses-induced tectonic uplifting, as verified in other areas of the northeastern Brazil. The evidences interpreted from the resulting data is a strong indication that this sector of the South American passive margin continued experiencing tectonic deformation long after the main rifting in the late Jurassic-early Cretaceous.

e) The analysis of the drainage divides of the study area showed some divide segments classified as mobile and following a high-elevation, chevron-shaped plateau developed over Precambrian rocks and sedimentary deposits. The divide migration was related to lithological control, recording differences in bedrock erodibility. How-

ever, there is also geological evidence that this plateau was not primarily formed only by lithological control. In contrast, a younger event of uplifting is interpreted here as a forcing factor which raised the basement rocks and the overlying sedimentary deposits to form the plateau, a hypothesis that remains to be further investigated.

f) The combination of local and regional geomorphometric variables with regionalization techniques succeeded to perform the geological discrimination of the northern Paraíba Basin. In this work, the slope, elevation, hypsometric integral, topographic coherence and valley depth were the variables with good potential to be used as inputs in this type of analysis. These variables helped differentiating Miocene and Quaternary units in this basin, and, particularly, in its northern sector. This work confirmed the expressive occurrence of the Post-Barreiras Sediments towards the northern sector of the Paraíba Basin.

REFERENCES

ABRAMS, M. The advanced spaceborne thermal emission and reflection radiometer (aster): data products for the high spatial resolution imager on nasa's terra platform. **International Journal of Remote Sensing**, v. 21, n. 5, p. 847–859, 2000. 21, 22

ALEXANDER, D. Relief inversion by denudation of the Monte Nerone anticline, central Italy. **Geomorphology**, v. 1, n. 2, p. 87–109, 1988. 108

ALLEVATO, S. R.; PINGARILHO, M. N. F. Análise e tratamento de material fotográfico no Projeto RADAMBRASIL. **Revista Brasileira de Cartografia**, v. 19, n. 24, p. 19–24, 1979. 18

ALMEIDA, F. F. M.; HASUI, Y.; BRITO NEVES, B. B.; FUCK, R. A. Brazilian structural provinces: an introduction. **Earth-Science Reviews**, v. 17, n. 1-2, p. 1–29, 1981. 31

ALMEIDA, F. F. M. D.; BRITO NEVES, B. B. D.; DAL RÉ CARNEIRO, C. The origin and evolution of the South American platform. **Earth Science Reviews**, v. 50, n. 1-2, p. 77–111, 2000. 31

ALVES, F.; VALERIANO, M. M.; ROSSETTI, D. F. Quaternary dome-like relief in the Northern Paraíba Basin, Northeastern Brazil. In: INTERNATIONAL CONFERENCE ON GEOMORPHOLOGY, 9., 2017. **Proceedings...** [S.l.], 2017. p. 1. 2

ALVES, F. C.; ROSSETTI, D. F. Neotectonic record in South American passive margin based on morphostructural analysis of northern Paraíba Basin, Brazil. **Zeitschrift fur Geomorphologie**, v. 61, n. 2, p. 95–108, 2017. 1

AMIT, R.; ZILBERMAN, E.; PORAT, N.; ENZEL, Y. Relief inversion in the Avrona Playa as evidence of large-magnitude historical earthquakes, Southern Arava Valley, Dead Sea Rift. **Quaternary Research**, v. 52, n. 1, p. 76–91, 1999. 108

ANDRADES-FILHO, C. O.; ROSSETTI, D. F. Intensidade da atividade tectônica na porção emersa da Bacia Paraíba e embasamento cristalino adjacente, Nordeste do Brasil. **Pesquisas em Geociências**, v. 42, n. 2, p. 113, 2015. 2

ANDRADES-FILHO, C. O.; ROSSETTI, D. F.; BEZERRA, F. H. R.; MEDEIROS, W. E.; VALERIANO, M. M.; CREMON, E. H.; OLIVEIRA, R. G. Mapping neogene and quaternary sedimentary deposits in northeastern brazil by integrating geophysics, remote sensing and geological field data. **Journal of South American Earth Sciences**, v. 56, p. 316–327, 2014. 20, 27, 29, 37, 116, 117

ANDREANI, L.; GLOAGUEN, R. Geomorphic analysis of transient landscapes in the Sierra Madre de Chiapas and Maya Mountains (northern Central America): implications for the North American-Caribbean-Cocos plate boundary. **Earth Surface Dynamics**, v. 4, n. 1, p. 71–102, 2016. 14

ANDREANI, L.; STANEK, K. P.; GLOAGUEN, R.; KRENTZ, O.; DOMÍNGUEZ-GONZÁLEZ, L. DEM-based analysis of interactions between tectonics and landscapes in the ore mountains and eger rift (East Germany and NW Czech Republic). **Remote Sensing**, v. 6, n. 9, p. 7971–8001, 2014. 1, 7, 11, 109, 110

ARTHAUD, M. H.; CABY, R.; FUCK, R. A.; DANTAS, E. L.; PARENTE, C. V. Geology of the northern Borborema Province, NE Brazil and its correlation with Nigeria, NW Africa. **Geological Society Special Publication**, v. 294, p. 49–67, 2008. 31, 33

ASSUMPÇÃO, M.; DIAS, F. L.; ZEVALLOS, I.; NALIBOFF, J. B. Intraplate stress field in South America from earthquake focal mechanisms. **Journal of South American Earth Sciences**, v. 71, p. 278–295, 2016. 108

BAATZ, M.; SCHÄPE, A. Multiresolution Segmentation: an optimization approach for high quality multi-scale image segmentation. In: ANGEWANDTE GEOGRAPHISCHE INFORMATIONS VERARBEITUNG. **Proceedings...** [S.l.], 2000. p. 12–23. 28, 38, 46

BARBOSA, A. J.; BRAGA, A. P. G. **Projeto Leste da Paraíba e Rio Grande do Norte. Relatório final integrado, folhas SB-25-V-C e SB-25-Y-A. R**. Recife, 1974. 31

BARBOSA, J. A.; SOUZA, E.; LIMA FILHO, M.; NEUMANN, V. A estratigrafia da Bacia Paraíba: uma reconsideração. **Estudos Geológicos**, v. 13, p. 89–108, 2003. 34

BERLIN, M. M.; ANDERSON, R. S. Modeling of knickpoint retreat on the Roan Plateau, western Colorado. **Journal of Geophysical Research: Earth Surface**, v. 112, n. 3, p. 1–16, 2007. 110, 111, 112

BERNARD, T.; SINCLAIR, H. D.; GAILLETON, B.; MUDD, S. M.; FORD, M. Lithological control on the post-orogenic topography and erosion history of the Pyrenees. **Earth and Planetary Science Letters**, v. 518, p. 53–66, 2019. 41

BEURLEN, K. Estratigrafia da faixa sedimentar costeira Recife-João Pessoa. **Boletin Geologico**, v. 16, n. 1, p. 43–53, 1967. 34

BEZERRA, F. H.; BRITO NEVES, B. B.; CORRÊA, A. C.; BARRETO, A. M.; SUGUIO, K. Late Pleistocene tectonic-geomorphological development within a passive margin - the Cariatá trough, northeastern Brazil. **Geomorphology**, v. 97, n. 3-4, p. 555–582, 2008. 2, 34, 43, 44, 65, 66, 76, 105, 109, 114

BEZERRA, F. H.; CASTRO, D. L. de; MAIA, R. P.; SOUSA, M. O.; MOURA-LIMA, E. N.; ROSSETTI, D. F.; BERTOTTI, G.; SOUZA, Z. S.; NOGUEIRA, F. C. Postrift stress field inversion in the Potiguar Basin, Brazil – implications for petroleum systems and evolution of the equatorial margin of South America. **Marine and Petroleum Geology**, p. 88–104, 2020. 2, 34, 106, 108

BEZERRA, F. H.; NASCIMENTO, A. F. do; FERREIRA, J. M.; NOGUEIRA, F. C.; FUCK, R. A.; NEVES, B. B.; SOUSA, M. O. Review of active faults in the Borborema Province, intraplate South America - integration of seismological and paleoseismological data. **Tectonophysics**, v. 510, n. 3-4, p. 269–290, 2011. 31, 33

BEZERRA, F. H.; ROSSETTI, D. F.; OLIVEIRA, R. G.; MEDEIROS, W. E.; NEVES, B. B.; BALSAMO, F.; NOGUEIRA, F. C.; DANTAS, E. L.; ANDRADES FILHO, C.; GÓES, A. M. Neotectonic reactivation of shear zones and implications for faulting style and geometry in the continental margin of NE Brazil. **Tectonophysics**, v. 614, p. 78–90, 2014. 2, 31, 33, 34, 43, 44, 65, 66, 76, 105, 106, 108, 109

BEZERRA, F. H.; VITA-FINZI, C. How active is a passive margin? palaeoseismicity in Northeastern Brazil. **Geology**, v. 28, n. 7, p. 591–594, 2000. 1

BEZERRA, F. H. R.; AMARO, V. E.; VITA-FINZI, C.; SAADI, A. Pliocene-Quaternary fault control of sedimentation and coastal plain morphology in NE Brazil. **Journal of South American Earth Sciences**, v. 14, n. 1, p. 61–75, 2001. 2

BLASCHKE, T.; HAY, G. J.; KELLY, M.; LANG, S.; HOFMANN, P.; ADDINK, E.; QUEIROZ FEITOSA, R.; MEER, F. V. D.; WERFF, H. V. D.; COILLIE, F. V.; TIEDE, D. Geographic object-based image analysis - towards a new paradigm.

ISPRS Journal of Photogrammetry and Remote Sensing, v. 87, p. 180–191, 2014. 28

BOULTON, S. J.; STOKES, M.; MATHER, A. E. Transient fluvial incision as an indicator of active faulting and Plio-Quaternary uplift of the Moroccan high Atlas. **Tectonophysics**, v. 633, n. 1, p. 16–33, 2014. 16, 17, 70, 110, 111, 112

BOX, G. E. P.; COX, D. R. An analysis of transformations. **Journal of the Royal Statistical Society: Series B (Methodological)**, v. 26, n. 2, p. 211–243, 1964. 27, 46

BREIMAN, L. Random forests. **Machine Learning**, v. 45, n. 1, p. 5–32, 2001. 29

BRITES, R. S.; BIAS, E. S.; ROSA, A. N. C. S. Classificação por regiões. In: MENESES, P. R.; ALMEIDA, T. (Ed.). **Introdução ao processamento de imagens de sensoriamento remoto.** Brasília: Universidade de Brasília, 2012. chapter 13, p. 266. 28

BRITO-NEVES, B.; RICCOMINI, C.; FERNANDES, T. M. G.; SANTANNA, L. G. O sistema tafrogênico terciário do saliente oriental nordestino na paraíba: um legado proterozóico. **Revista Brasileira de Geociências**, v. 1, n. 34, p. 127–134, 2004. 2, 31, 65, 66, 105, 109

BRITO-NEVES, B. B.; ALBUQUERQUE, J. P. T.; COUTINHO, J. M. V.; BEZERRA, F. H. R. Novos dados geológicos e geofísicos para caracterização geométrica e estratigráfica da Sub-Bacia de Alhandra (sudeste da Paraíba). **Geologia USP-Série Científica**, v. 9, n. 2, p. 63–87, 2009. 2, 105, 109

BURBANK, D. W. Characteristic size of relief. **Nature**, v. 359, n. 6395, p. 483–484, 1992. 110

BURSZTYN, N.; PEDERSON, J. L.; TRESSLER, C.; MACKLEY, R. D.; MITCHELL, K. J. Rock strength along a fluvial transect of the Colorado Plateau - quantifying a fundamental control on geomorphology. **Earth and Planetary Science Letters**, v. 429, p. 90–100, 2015. 41

CARVALHO, A. A. de; MONTENEGRO, A. A. d. A.; SILVA, H. P. da; LOPES, I.; MORAIS, J. E. F. de; SILVA, T. G. F. da. Trends of rainfall and temperature in Northeast Brazil. **Revista Brasileira de Engenharia Agrícola e Ambiental**, v. 24, p. 15–23, 2020. 110

CASSETI, V. **Elementos de geomorfologia**. Goiânia: UFG, 1994. 137 p. 6

CHRISTOFOLETTI, A. **Geomorfologia fluvial. Vol I - canal fluvial**. São Paulo: [s.n.], 1981. 137 p. 12

COMPANHIA DE PESQUISA DE RECURSOS MINERAIS (CPRM). **Fosfato de Miriri - estados de Pernambuco e Paraíba**: biblioteca digital. 2001. Available from: <http://rigeo.cprm.gov.br/xmlui/bitstream/handle/doc/1551/rel_fosfato_miriri.pdf?sequence=1&isAllowed=y>. Access in: 08 março 2021. 37

CONGALTON, R. G. A review of assessing the accuracy of classifications of remotely sensed data. **Remote Sensing of Environment**, v. 37, n. 1, p. 35–46, 1991. 49

CONRAD, O.; BECHTEL, B.; BOCK, M.; DIETRICH, H.; FISCHER, E.; GERLITZ, L.; WEHBERG, J.; WICHMANN, V.; BÖHNER, J. System for Automated Geoscientific Analyses (SAGA) v. 2.1.4. **Geoscientific Model Development**, v. 8, n. 7, p. 1991–2007, 2015. 24, 25, 38

COSTA, L. R. F.; MAIA, R. P.; BARRETO, L. L.; SALES, V. C. C. Geomorfologia do nordeste setentrional brasileiro: uma proposta de classificação. **Revista Brasileira de Geomorfologia**, v. 21, n. 185-208, 2020. 35

COUTAND, I.; COBBOLD, P. R.; URREIZTIETA, M. de; GAUTIER, P.; CHAUVIN, A.; GAPAIS, D.; ROSSELLO, E. A.; LÓPEZ-GAMUNDÍ, O. Style and history of Andean deformation, Puna plateau, northwestern Argentina. **Tectonics**, v. 20, n. 2, p. 210–234, 2001. 107, 108

COX, K. G. The role of mantle plumes in the development of continental drainage patterns. **Nature**, v. 342, n. 6252, p. 873–877, 1989. 107

CRACKNELL, M. J.; READING, A. M. Geological mapping using remote sensing data: a comparison of five machine learning algorithms, their response to variations in the spatial distribution of training data and the use of explicit spatial information. **Computers and Geosciences**, v. 63, p. 22–33, 2014. 29

CRIPPEN, R.; BUCKLEY, S.; AGRAM, P.; BELZ, E.; GURROLA, E.; HENSLEY, S.; KOBRICK, M.; LAVALLE, M.; MARTIN, J.; NEUMANN, M.; NGUYEN, Q.; ROSEN, P.; SHIMADA, J.; SIMARD, M.; TUNG, W. NASADEM global elevation model: methods and progress. In: ISPRS ANNALS OF PHOTOGRAMMETRY, REMOTE SENSING AND SPATIAL INFORMATION SCIENCES, 2016. **Proceedings...** Prague, Czech Republic, 2016. p. 125–128. 22, 23

CROSBY, B. T.; WHIPPLE, K. X. Knickpoint initiation and distribution within fluvial networks: 236 waterfalls in the Waipaoa River, North Island, New Zealand. **Geomorphology**, v. 82, n. 1, p. 16–38, 2006. 17, 111, 112

CSILLIK, O.; EVANS, I. S.; DRăGUţ, L. Transformation (normalization) of slope gradient and surface curvatures, automated for statistical analyses from DEMs. **Geomorphology**, v. 232, p. 65–77, 2015. 26, 27, 38, 46

DAS, J. D.; SARAF, A. K.; SHUJAT, Y. A remote sensing technique for identifying geometry and geomorphological features of the Indo-Burman frontal fold belt. **International Journal of Remote Sensing**, v. 31, n. 16, p. 4481–4503, 2010. 7

DEFFONTAINES, B.; CHOROWICZ, J. Principles of drainage basin analysis from multisource data: application to the structural analysis of the Zaire Basin. **Tectonophysics**, v. 194, n. 3, p. 237–263, 1991. 1, 5, 6, 7, 9, 39, 108

DEMOULIN, A. Testing the tectonic significance of some parameters of longitudinal river profiles: the case of the Ardenne (Belgium, NW Europe). **Geomorphology**, v. 24, n. 2, p. 189–208, 1998. 13, 15, 110

DRăGUţ, L.; BLASCHKE, T. Automated classification of landform elements using object-based image analysis. **Geomorphology**, v. 81, n. 3-4, p. 330–344, 2006. 27, 28, 29, 116

DRăGUţ, L.; EISANK, C. Object representations at multiple scales from digital elevation models. **Geomorphology**, v. 129, n. 3-4, p. 183–189, 2011. 28

DRăGUţ, L.; TIEDE, D.; LEVICK, S. R. ESP: A tool to estimate scale parameter for multiresolution image segmentation of remotely sensed data. **International Journal of Geographical Information Science**, v. 24, n. 6, p. 859–871, 2010. 28, 29

EISANK, C.; SMITH, M.; HILLIER, J. Assessment of multiresolution segmentation for delimiting drumlins in digital elevation models. **Geomorphology**, v. 214, p. 452–464, 2014. 28

EL HAGE, M.; SIMONETTO, E.; FAOUR, G.; POLIDORI, L. Impact of DEM reconstruction parameters on topographic indices. **The International Archives of the Photogrammetry, Remote Sensing and Spatial Information Sciences**, v. 38, p. 40–44, 2010. 25

El HAMDOUNI, R.; IRIGARAY, C.; FERNÁNDEZ, T.; CHACÓN, J.; KELLER, E. A. Assessment of relative active tectonics, southwest border of the Sierra Nevada (southern Spain). **Geomorphology**, v. 96, n. 1-2, p. 150–173, 2008. 1, 11, 109, 110

EVANS, I. S. General geomorphometry, derivatives of altitude, and descriptive statistics. In: CHORLEY, R. J. (Ed.). **Spatial analysis in geomorphology.** London: Methuen & Co., 1972. p. 17–90. 23, 24

_____. **Properties of the Wessex land surface: an investigation of dimensionality and the choice of key variables**. Durham, 1984. 137 p. 27, 46

FARR, T. G.; ROSEN, P. A.; CARO, E.; CRIPPEN, R.; DUREN, R.; HENSLEY, S.; KOBRICK, M.; PALLER, M.; RODRIGUEZ, E.; ROTH, L.; SEAL, D.; SHAFFER, S.; SHIMADA, J.; UMLAND, J.; WERNER, M.; OSKIN, M.; BURBANK, D.; ALSDORF, D. The shuttle radar topography mission. **Reviews of Geophysics**, v. 45, n. 2, 2007. 22

FERREIRA, J. M.; BEZERRA, F. H. R.; SOUSA, M. O. L.; NASCIMENTO, A. F. do; SÁ, J. M.; FRANÇA, G. S. The role of Precambrian mylonitic belts and present-day stress field in the coseismic reactivation of the Pernambuco lineament, Brazil. **Tectonophysics**, v. 456, n. 3, p. 111–126, 2008. 33

FORTE, A. M.; WHIPPLE, K. X. Criteria and tools for determining drainage divide stability. **Earth and Planetary Science Letters**, v. 493, p. 102–117, 2018. 1, 17, 18, 38, 44, 80

_____. Short communication: the Topographic Analysis Kit (TAK) for TopoToolbox. **Earth Surface Dynamics**, v. 7, n. 1, p. 87–95, 2019. 1, 10, 38, 43

FORTE, A. M.; YANITES, B. J.; WHIPPLE, K. X. Complexities of landscape evolution during incision through layered stratigraphy with contrasts in rock strength. **Earth Surface Processes and Landforms**, v. 41, n. 12, p. 1736–1757, 2016. 114

FOSSEN, H. **Structural geology**. Cambridge: Cambridge University Press, 2010. 362 p. 5, 6

GALLAGHER, K.; BROWN, R.; JOHNSON, C. Fission track analysis and its applications to geological problems. **Annual Review of Earth and Planetary Sciences**, v. 26, n. 1, p. 519–572, 1998. 2

GALLEN, S. F. Lithologic controls on landscape dynamics and aquatic species evolution in post-orogenic mountains. **Earth and Planetary Science Letters**, v. 493, p. 150–160, 2018. 41

GALLEN, S. F.; WEGMANN, K. W. River profile response to normal fault growth and linkage: an example from the Hellenic forearc of south-central Crete, Greece. **Earth Surface Dynamics**, v. 5, n. 1, p. 161–186, 2017. 1, 10, 14, 38, 40

GALLEN, S. F.; WEGMANN, K. W.; BOHNENSTIEHL, D. W. R. Miocene rejuvenation of topographic relief in the southern Appalachians. **GSA Today**, v. 23, n. 2, p. 4–10, 2013. 1, 16, 107, 111

GANDINI, R.; ROSSETTI, D. d. F.; NETTO, R. G.; BEZERRA, F. H. R.; GÓES, A. M. Neotectonic evolution of the Brazilian northeastern continental margin based on sedimentary facies and ichnology. **Quaternary Research (United States)**, v. 82, n. 2, p. 462–472, 2014. 2, 34, 106, 107

GARZIONE, C. N.; HOKE, G. D.; LIBARKIN, J. C.; WITHERS, S.; MACFADDEN, B.; EILER, J.; GHOSH, P.; MULCH, A. Rise of the Andes. **Science**, v. 320, n. 5881, p. 1304 – 1307, 2008. 107, 108

GERENTE, J.; VALERIANO, M. M.; MOREIRA, E. P. Regionalização de variáveis geomorfométricas para o mapeamento dos domínios morfoestruturais da bacia hidrográfica do rio Itajaí-Açu (SC). **Revista Brasileira de Geomorfologia**, v. 19, n. 3, p. 433–446, 2018. 27, 29, 116, 117

GÓMEZ, J.; SCHOBBENHAUS, C.; MONTES, N. **Geological Map of South America 2019. Scale 1:5 000 000.** Paris, 2019. 32

GROHMANN, C. H. Effects of spatial resolution on slope and aspect derivation for regional-scale analysis. **Computers and Geosciences**, v. 77, p. 111–117, 2015. 25

GURGEL, S. P.; BEZERRA, F. H.; CORRÊA, A. C.; MARQUES, F. O.; MAIA, R. P. Cenozoic uplift and erosion of structural landforms in NE Brazil. **Geomorphology**, v. 186, p. 68–84, 2013. 2, 34, 105, 106

HACK, J. Studies of longitudinal stream profiles in Virginia and Maryland. **USGS Professional Paper 249**, p. 97, 1957. 14, 43, 75, 111

HACK, J. T. Stream-profile analysis and stream-gradient index. **Journal of Research of the U.S. Geological Survey**, v. 1, n. 4, p. 421–429, 1973. 14

HARE, P. W.; GARDNER, T. W. Geomorphic indicators of vertical neotectonism along converging plate margins, Nicoya Peninsula, Costa Rica. In: MORISAWA, M.; HACK, J. (Ed.). **15th Annual Bighamton Geomorphology Symposium.** Boston: [s.n.], 1985. p. 75–104. 11, 12, 40, 109

HAREL, M. A.; MUDD, S. M.; ATTAL, M. Global analysis of the stream power law parameters based on worldwide 10Be denudation rates. **Geomorphology**, v. 268, p. 184–196, 2016. 41

HAVIV, I.; ENZEL, Y.; WHIPPLE, K. X.; ZILBERMAN, E.; MATMON, A.; STONE, J.; FIFIELD, K. L. Evolution of vertical knickpoints (waterfalls) with resistant caprock: insights from numerical modeling. **Journal of Geophysical Research: Earth Surface**, v. 115, n. F3, 2010. 16

HENDERSON, F. M.; LEWIS, A. J. **Principles and applications of imaging radar: manual of remote sensing**. New York: John Wiley and Sons, 1998. 896 p. 19, 21, 23

HOWARD, A.; DIETRICH, W.; SEIDL, M. Modeling fluvial erosion on regional to continental scales. **Journal of Geophysical Research: Solid Earth**, v. 99, p. 13971– 13986, 1994. 14

HOWARD, A. D. Drainage analysis in geologic interpretation: a summation1. **AAPG Bulletin**, v. 51, n. 11, p. 2246–2259, 1967. 1, 5, 6, 7, 8, 9, 39, 108

INSTITUTO NACIONAL DE PESQUISAS ESPACIAIS (INPE). **Topodata: banco de dados geomorfométricos do Brasil**: biblioteca digital. 2008. Available from: <http://www.dsr.inpe.br/topodata>. Access in: 08 março 2021. 23

JAPSEN, P.; BONOW, J. M.; GREEN, P. F.; CHALMERS, J. A.; LIDMAR-BERGSTRÖM, K. Elevated, passive continental margins: long-term highs or Neogene uplifts? New evidence from West Greenland. **Earth and Planetary Science Letters**, v. 248, n. 1, p. 330–339, 2006. 2

JAPSEN, P.; BONOW, J. M.; GREEN, P. F.; COBBOLD, P. R.; CHIOSSI, D.; LILLETVEIT, R.; MAGNAVITA, L. P.; PEDREIRA, A. Episodic burial and exhumation in NE Brazil after opening of the South Atlantic. **Bulletin of the Geological Society of America**, v. 124, n. 5-6, p. 800–816, 2012. 2

JAPSEN, P.; CHALMERS, J. A.; GREEN, P. F.; BONOW, J. M. Elevated, passive continental margins: not rift shoulders, but expressions of episodic,

post-rift burial and exhumation. **Global and Planetary Change**, v. 90-91, p. 73–86, 2012. 2, 106, 107

KALE, V. S.; SHEJWALKAR, N. Uplift along the western margin of the Deccan Basalt Province: is there any geomorphometric evidence? **Journal of Earth System Science**, v. 117, n. 6, p. 959–971, 2008. 1

KEGEL, W. Geologia do fosfato de Pernambuco. **Boletim do Departamento Nacional de Produção Mineral - DNPM**, v. 157, p. 1–54, 1955. 34

KELLER, E. A.; PINTER, N. Geomorphic indices of active tectonics. **Active Tectonics: Earthquakes, Uplift, and Landscape**, p. 121–147, 1996. 1, 5, 7, 10, 11, 12

KENT, E.; BOULTON, S. J.; WHITTAKER, A. C.; STEWART, I. S.; Cihat Alçiçek, M. Normal fault growth and linkage in the Gediz (Alaşehir) Graben, Western Turkey, revealed by transient river long-profiles and slope-break knickpoints. **Earth Surface Processes and Landforms**, v. 42, n. 5, p. 836–852, 2017. 111, 112

KING, L. A geomorfologia do Brasil Oriental. **Revista Brasileira de Geografia**, n. 2, p. 37–72, 1956. 1

_____. **The morphology of the Earth**. Edinburgh: Oliver and Boyd, 1967. 1

KIRBY, E.; WHIPPLE, K. X. Expression of active tectonics in erosional landscapes. **Journal of Structural Geology**, v. 44, p. 54–75, 2012. 1, 14, 15, 16, 40, 43, 73, 111, 112, 113

KLÖCKING, M.; HOGGARD, M. J.; RODRÍGUEZ TRIBALDOS, V.; RICHARDS, F. D.; GUIMARÃES, A. R.; MACLENNAN, J.; WHITE, N. J. A tale of two domes: Neogene to recent volcanism and dynamic uplift of northeast Brazil and southwest Africa. **Earth and Planetary Science Letters**, v. 547, p. 116464, 2020. 107

LAGUE, D. The stream power river incision model: evidence, theory and beyond. **Earth Surface Processes and Landforms**, v. 39, n. 1, p. 38–61, 2014. 14

LEROY, M.; DAUTEUIL, O.; COBBOLD, P. R. Incipient shortening of a passive margin: the mechanical roles of continental and oceanic lithospheres. **Geophysical Journal International**, v. 159, n. 1, p. 400–411, 2004. 107

LIMA, J. C.; BEZERRA, F. H.; ROSSETTI, D. F.; BARBOSA, J. A.; MEDEIROS, W. E.; de Castro, D. L.; VASCONCELOS, D. L. Neogene–Quaternary fault reactivation influences coastal basin sedimentation and landform in the continental margin of NE Brazil. **Quaternary International**, v. 438, p. 92–107, 2017. 2, 34, 43, 44, 65, 66, 76, 105, 106

LIMA NETO, H. C.; FERREIRA, J. M.; BEZERRA, F. H. R.; ASSUMPÇÃO, M. S.; NASCIMENTO, A. F.; SOUSA, M. O. L.; MENEZES, E. A. S. Upper crustal earthquake swarms in São Caetano: reactivation of the Pernambuco shear zone and trending branches in intraplate Brazil. **Tectonophysics**, v. 608, p. 804–811, 2013. 33

LOPES, A. E. V.; ASSUMPÇÃO, M.; NASCIMENTO, A. F.; FERREIRA, J. M.; MENEZES, E. A. S.; BARBOSA, J. R. Intraplate earthquake swarm in Belo Jardim, NE Brazil: reactivation of a major Neoproterozoic shear zone (Pernambuco Lineament). **Geophysical Journal International**, v. 180, n. 3, p. 1303–1312, 2010. 33

MABESOONE, J. Relief of Northeastern Brazil and its correlated sediments. **Zeitschrift für Geomorphologie**, v. 10, n. 4, p. 419–453, 1966. 31

MABESOONE, J. M.; CASTRO, C. Desenvolvimento geomorfológico do Nordeste Brasileiro. **Boletim do Núcleo Nordeste da Sociedade Brasileira de Geologia**, v. 3, p. 5–35, 1976. 1

MACKIN, J. H. Concept of the Graded River. **Geological Society of American Bulletin**, v. 59, p. 463–512, 1948. 13

MAHMOOD, S. A.; GLOAGUEN, R. Appraisal of active tectonics in Hindu Kush: insights from DEM derived geomorphic indices and drainage analysis. **Geoscience Frontiers**, v. 3, n. 4, p. 407–428, 2012. 1, 7, 10, 11, 12, 109, 110

MAIA, R.; BEZERRA, F. H. R. Inversão neotectônica do relevo na Bacia Potiguar, Nordeste do Brasil. **Revista Brasileira de Geomorfologia**, v. 15, n. 1, p. 61–74, 2014. 2, 105, 106, 108

MANTELLI, L. R.; ROSSETTI, D. F.; ALBUQUERQUE, P. G.; VALERIANO, M. M. Applying SRTM digital elevation model to unravel Quaternary drainage in forested areas of Northeastern Amazonia. **Computers & Geosciences**, v. 35, n. 12, p. 2331–2337, 2009. 22

MARK, D. M. Geomorphometric parameters: a review and evaluation. **Geografiska Annaler: Series A, Physical Geography**, v. 57, n. 3-4, p. 165–177, 1975. 24

MARLIYANI, G. I.; ARROWSMITH, J. R.; WHIPPLE, K. X. Characterization of slow slip rate faults in humid areas: Cimandiri fault zone, Indonesia. **Journal of Geophysical Research: Earth Surface**, v. 121, n. 12, p. 2287–2308, 2016. 1, 41

MARQUES, F. O.; NOGUEIRA, F. C.; BEZERRA, F. H.; CASTRO, D. L. de. The Araripe Basin in NE Brazil: an intracontinental graben inverted to a high-standing horst. **Tectonophysics**, v. 630, n. 3, p. 251–264, 2014. 2, 34, 105, 106, 108, 114

MATOS, R. M. D. The Northeast Brazilian rift system. **Tectonics**, v. 11, n. 4, p. 766–791, 1992. 34

MILIARESIS, G. C.; VENTURA, G.; VILARDO, G. Terrain modelling of the complex volcanic terrain of Ischia Island, Italy. **Canadian Journal of Remote Sensing**, v. 35, n. 4, p. 385–398, 2009. 20, 23, 24, 27, 28, 29, 116

MOORE, I. D.; GRAYSON, R. B.; LADSON, A. R. Digital terrain modelling: a review of hydrological, geomorphological, and biological applications. **Hydrological Processes**, v. 5, n. 1, p. 3–30, 1991. 21, 24

MORAIS NETO, J. M.; HEGARTY, K. A.; KARNER, G. D.; ALKMIM, F. F. Timing and mechanisms for the generation and modification of the anomalous topography of the Borborema province, northeastern Brazil. **Marine and Petroleum Geology**, v. 26, n. 7, p. 1070–1086, 2009. 107

MOREIRA, E. P. **Análise regional da geomorfometria de microbacias hidrográficas**. 2018. 151 p. Thesis (PhD in Remote Sensing) — Instituto Nacional de Pesquisas Espaciais (INPE), São José dos Campos, 2018. 27, 28, 29, 116, 117

MUDD, S. M.; CLUBB, F. J.; GAILLETON, B.; HURST, M. D. How concave are river channels? **Earth Surface Dynamics**, v. 6, n. 2, p. 505–523, 2018. 15

MUELLER, J. E. Re-evaluation of the relationship of master streams and drainage basins. **Geological Society of America Bulletin**, v. 83, p. 3471–3474, 1972. 111

MUÑOZ, V. A.; VALERIANO, M. M. Modelagem da dissecação por geoprocessamento para delineamento de manchas de solo. In: SIMPÓSIO BRASILEIRO DE SENSORIAMENTO REMOTO, 2009, Natal. **Proceedings...** São José dos Campos: INPE, 2009. p. 77417748. 24, 25, 26

NIEMANN, J. D.; GASPARINI, N. M.; TUCKER, G. E.; BRAS, R. L. A quantitative evaluation of Playfair's law and its use in testing long-term stream erosion models. **Earth Surface Processes and Landforms**, v. 26, n. 12, p. 1317–1332, 2001. 17, 112

NOETHER, G. E. **Introduction to statistics: the nonparametric way**. Stanford, CA: Springer, 1991. 414 p. 43

NOGUEIRA, F. C.; BEZERRA, F. H.; FUCK, R. A. Quaternary fault kinematics and chronology in intraplate northeastern Brazil. **Journal of Geodynamics**, v. 49, n. 2, p. 79–91, 2010. 2

NOGUEIRA, F. C.; MARQUES, F. O.; BEZERRA, F. H.; CASTRO, D. L. de; FUCK, R. A. Cretaceous intracontinental rifting and post-rift inversion in NE Brazil: insights from the Rio do Peixe Basin. **Tectonophysics**, v. 644, p. 92–107, 2015. 2, 34, 105, 106, 108, 114

OBRUCHEV, V. A. Osnovnye cherty kinetiki i plastiki neotektonik. **Akademii Nauk Izvetiya Seriya Geologicheskaya**, v. 5, p. 13–24, 1948. 5

O'LEARY, D. W.; FRIEDMAN, J. D.; POHN, H. A. Lineament, linear, lineation: some proposed new standards for old terms. **GSA Bulletin**, v. 87, n. 10, p. 1463–1469, 1976. 5, 6

OWONO, F. M.; NTAMAK-NIDA, M. J.; DAUTEUIL, O.; GUILLOCHEAU, F.; NJOM, B. Morphology and long-term landscape evolution of the South African plateau in South Namibia. **Catena**, v. 142, p. 47–65, 2016. 1, 11, 109

PEDOJA, K.; HUSSON, L.; REGARD, V.; COBBOLD, P. R.; OSTANCIAUX, E.; JOHNSON, M. E.; KERSHAW, S.; SAILLARD, M.; MARTINOD, J.; FURGEROT, L.; WEILL, P.; DELCAILLAU, B. Relative sea-level fall since the last interglacial stage: are coasts uplifting worldwide? **Earth-Science Reviews**, v. 108, n. 1-2, p. 1–15, 2011. 106, 107, 115

PÉREZ-PEÑA, J. V.; AL-AWABDEH, M.; AZAÑÓN, J. M.; GALVE, J. P.; BOOTH-REA, G.; NOTTI, D. SwathProfiler and NProfiler: two new ArcGIS Add-ins for the automatic extraction of swath and normalized river profiles. **Computers and Geosciences**, v. 104, p. 135–150, 2017. 1, 11, 38, 39, 40, 109, 110

PÉREZ-PEÑA, J. V.; AZAÑÓN, J. M.; BOOTH-REA, G.; AZOR, A.; DELGADO, J. Differentiating geology and tectonics using a spatial

autocorrelation technique for the hypsometric integral. **Journal of Geophysical Research: Earth Surface**, v. 114, n. 2, p. 1–15, 2009. 11

PÉREZ-PEÑA, J. V.; AZOR, A.; AZAÑÓN, J. M.; KELLER, E. A. Active tectonics in the Sierra Nevada (Betic Cordillera, SE Spain): insights from geomorphic indexes and drainage pattern analysis. **Geomorphology**, v. 119, n. 1-2, p. 74–87, 2010. 108

PERRON, J. T.; ROYDEN, L. An integral approach to bedrock river profile analysis. **Earth Surface Processes and Landforms**, v. 38, n. 6, p. 570–576, 2013. 15, 40

PIKE, R. J. The geometric signature: quantifying landslide-terrain types from digital elevation models. **Mathematical Geology**, v. 20, n. 5, p. 491–511, 1988. 24

PIKE, R. J.; EVANS, I. S.; HENGL, T. Geomorphometry: a brief guide. **Developments in Soil Science**, v. 33, p. 3–30, 2009. 23

PIKE, R. J.; WILSON, S. E. Elevation-relief ratio, hypsometric integral, and geomorphic area-altitude analysis. **Bulletin of the Geological Society of America**, v. 82, n. 4, p. 1079–1084, 1971. 11

POLIDORI, L.; SIMONETTO, E. Effect of scale on the correlation between topography and canopy elevations in an airborne InSAR product over Amazonia. **Procedia Technology**, v. 16, p. 180–185, 2014. 22

RABUS, B.; EINEDER, M.; ROTH, A.; BAMLER, R. The shuttle radar topography mission—a new class of digital elevation models acquired by spaceborne radar. **ISPRS Journal of Photogrammetry and Remote Sensing**, v. 57, n. 4, p. 241–262, 2003. 1, 21, 22

RATHJE, E. M.; ADAMS, B. J. The role of remote sensing in earthquake science and engineering: opportunities and challenges. **Earthquake Spectra**, v. 24, n. 2, p. 471–492, 2008. 19

RIEGLER, G.; HENNIG, S. D.; WEBER, M. WorldDEM - A novel global foundation layer. **International Archives of the Photogrammetry, Remote Sensing and Spatial Information Sciences - ISPRS Archives**, v. 40, p. 183–187, 2015. 22, 23

RIGON, R.; RODRIGUEZ-ITURBE, I.; MARITAN, A.; GIACOMETTI, A.; TARBOTON, D. G.; RINALDO, A. On Hack's law. **Water Resources Research**, v. 32, n. 11, p. 3367–3374, 1996. 111

ROSIM, S.; RICARDO, J.; OLIVEIRA, D. F.; JARDIM, A. C.; NAMIKAWA, L. M. TerraHidro: a distributed hydrology modelling system with high quality drainage extraction. **International Conference on Advanced Geographic Information Systems**, n. 5, p. 161–167, 2013. 37, 38

ROSSETTI, D. F.; BEZERRA, F. H. R.; DOMINGUEZ, J. M. L. Late Oligocene–Miocene transgressions along the equatorial and eastern margins of Brazil. **Earth-Science Reviews**, v. 123, p. 87–112, 2013. 34

ROSSETTI, D. F.; BEZERRA, F. H. R.; GÓES, A. M.; VALERIANO, M. M.; ANDRADES-FILHO, C. O.; MITTANI, J. C. R.; TATUMI, S. H.; BRITO-NEVES, B. B. Late Quaternary sedimentation in the Paraíba Basin, Northeastern Brazil: landform, sea level and tectonics in eastern South America passive margin. **Palaeogeography, Palaeoclimatology, Palaeoecology**, v. 300, n. 1, p. 191–204, 2011. 2, 105, 106

ROSSETTI, D. F.; BEZERRA, F. H. R.; GÓES, A. M.; NEVES, B. B. B. Sediment deformation in Miocene and post-Miocene strata, Northeastern Brazil: evidence for paleoseismicity in a passive margin. **Sedimentary Geology**, v. 235, n. 3, p. 172–187, 2011. 2, 34, 105, 106

ROSSETTI, D. F.; GÓES, A. M.; BEZERRA, F. H.; VALERIANO, M. M.; BRITO-NEVES, B. B.; OCHOA, F. L. Contribution to the stratigraphy of the onshore Paraíba basin, Brazil. **Anais da Academia Brasileira de Ciencias**, v. 84, n. 2, p. 313–333, 2012. 34, 35, 37, 39, 42, 49, 59, 63, 95, 96, 97, 98, 103, 117

SAADI, A.; BEZERRA, F. H. R.; COSTA, R. D.; IGREJA, H. L. S.; FRANZINELLI, E. Neotectônica da plataforma brasileira. In: SOUZA, C. R. G.; SUGUIO, K.; OLIVEIRA, A. M. S.; OLIVEIRA, P. E. (Ed.). **Quaternário do Brasil**. São Paulo: Holos, 2005. p. 1–31. 5

SANTOS, E. J.; FERREIRA, C. A.; SILVA JR, J. M. F. **Geologia e recursos minerais do Estado da Paraíba**. Brasília, 2002. 234 p. 37, 49, 93, 101, 117

SCHWANGHART, W.; SCHERLER, D. Short communication: TopoToolbox 2 - MATLAB-based software for topographic analysis and modeling in Earth surface sciences. **Earth Surface Dynamics**, v. 2, n. 1, p. 1–7, 2014. 1, 10, 38

SCOTTI, V. N.; MOLIN, P.; FACCENNA, C.; SOLIGO, M.; CASAS-SAINZ, A. The influence of surface and tectonic processes on landscape evolution of the Iberian Chain (Spain): quantitative geomorphological analysis and geochronology. **Geomorphology**, v. 206, p. 37–57, 2014. 1, 11, 109, 110

SHACKLETON, N. Oxygen isotopes, ice volume and sea level. **Quaternary Science Reviews**, v. 6, n. 3, p. 183 – 190, 1987. 113

SHAHZAD, F.; GLOAGUEN, R. TecDEM: A MATLAB based toolbox for tectonic geomorphology, Part 1: drainage network preprocessing and stream profile analysis. **Computers and Geosciences**, v. 37, n. 2, p. 250–260, 2011. 1, 10

SHARY, P. A.; SHARAYA, L. S.; MITUSOV, A. V. Fundamental quantitative methods of land surface analysis. **Geoderma**, v. 107, n. 1, p. 1–32, 2002. 23

SMART, J. S.; SURKAN, A. J. The relation between mainstream length and area in drainage basins. **Water Resources Research**, v. 3, n. 4, p. 963–974, 1967. 111

SNYDER, N. P.; WHIPPLE, K. X.; TUCKER, G. E.; MERRITTS, D. J. Stream profiles in the Mendocino triple junction region, northern California. **GSA Bulletin**, v. 112, n. 8, p. 1250–1263, 2000. 14, 15

SOARES, P. C.; FIORI, A. P. Lógica e sistemática na análise e interpretação de fotografias aéreas em geologia. **Notícia Geomorfológica**, v. 16, p. 71–104, 1976. 18

STRAHLER, A. N. Hipsometric (area-altitude) analysis and erosional topography. **Geological Society of America Bulletin**, v. 63, n. 10, p. 1117–1142, 1952. 11

STRONG, C. M.; ATTAL, M.; MUDD, S. M.; SINCLAIR, H. D. Lithological control on the geomorphic evolution of the Shillong Plateau in Northeast India. **Geomorphology**, v. 330, p. 133–150, 2019. 17, 114

SUERTEGARAY, D. M. A.; ROSSATO, M. S.; BELLANCA, E. T.; FACHINELLO, A.; CANDIDO, L. A.; SILVA, C. R. **Terra feições ilustradas**. Porto Alegre: UFRGS, 2003. 263 p. 6

SUGUIO, K.; MARTIN, L. The role of neotectonics in the evolution of the Brazilian coast. **Geonomos**, v. 4, p. 45–53, 1996. 2, 34

TADONO, T.; TAKAKU, J.; TSUTSUI, K.; ODA, F.; NAGAI, H. Status of ALOSWorld 3D (AW3D) global DSM generation. In: INTERNATIONAL

GEOSCIENCE AND REMOTE SENSING SYMPOSIUM (IGARSS), 2015, Milan, Italy. **Proceedings...** Milan, 2015. p. 3822–3825. 21, 22

TELBISZ, T.; KOVÁCS, G.; SZÉKELY, B.; SZABÓ, J. Topographic swath profile analysis: a generalization and sensitivity evaluation of a digital terrain analysis tool. **Zeitschrift fur Geomorphologie**, v. 57, n. 4, p. 485–513, 2013. 10, 39, 110

TOUTIN, T.; GRAY, L. State-of-the-art of elevation extraction from satellite SAR data. **ISPRS Journal of Photogrammetry and Remote Sensing**, v. 55, n. 1, p. 13–33, 2000. 21

TRIBALDOS, R. V.; WHITE, N. J.; ROBERTS, G. G.; HOGGARD, M. J. Spatial and temporal uplift history of South America from calibrated drainage analysis. **Geochemistry, Geophysics, Geosystems**, v. 18, n. 6, p. 2321–2353, 2017. 106, 107, 115

TUCKER, G. E.; WHIPPLE, K. X. Topographic outcomes predicted by stream erosion models: sensitivity analysis and intermodel comparison. **Journal of Geophysical Research: Solid Earth**, v. 107, n. B9, p. 1–16, 2002. 16

TURNER, J. P.; WILLIAMS, G. A. Sedimentary basin inversion and intra-plate shortening. **Earth-Science Reviews**, v. 65, n. 3, p. 277–304, 2004. 108

VALERIANO, M. M.; ROSSETTI, D. F. Análise digital do padrão de coerência da orientação de vertentes em terrenos planos. In: CONGRESSO DA ASSOCIAÇÃO BRASILEIRA DE ESTUDOS DO QUATERNÁRIO (ABEQUA), 2011, Búzios, Brazil. **Proceedings...** Búzios, 2011. p. 1–5. 24, 25, 116

_____. Regionalization of local geomorphometric derivations for geological mapping in the sedimentary domain of central Amazônia. **Computers & Geosciences**, v. 100, p. 46–56, 2017. 20, 23, 24, 27, 28, 45, 82, 116, 117

VAN SCHMUS, W. R.; OLIVEIRA, E. P.; SILVA FILHO, A. F.; TOTEU, S. F.; PENAYE, J.; GUIMARÃES, I. P. Proterozoic links between the Borborema Province, NE Brazil, and the Central African fold belt. **Geological Society Special Publication**, v. 294, p. 69–99, 2008. 31

VASCONCELOS, D. L.; BEZERRA, F. H.; CLAUSEN, O. R.; MEDEIROS, W. E.; CASTRO, D. L. de; VITAL, H.; BARBOSA, J. A. Influence of Precambrian shear zones on the formation of oceanic fracture zones along the continental margin of Brazil. **Marine and Petroleum Geology**, v. 101, p. 322–333, 2019. 34

VASCONCELOS, D. L.; BEZERRA, F. H.; MEDEIROS, W. E.; CASTRO, D. L. de; CLAUSEN, O. R.; VITAL, H.; OLIVEIRA, R. G. Basement fabric controls rift nucleation and postrift basin inversion in the continental margin of NE Brazil. **Tectonophysics**, v. 751, p. 23–40, 2019. 2, 34, 105, 106, 108

VASCONCELOS, D. L.; MARQUES, F. O.; NOGUEIRA, F. C. C.; PEREZ, Y. A. R.; BEZERRA, F. H. R.; STOHLER, R. C.; SOUZA, J. A. B. Tectonic inversion assessed by integration of geological and geophysical data: the intracontinental rio do peixe basin, ne brazil. **Basin Research**, v. 33, p. 705–728, 2020. 105, 106, 108

VENABLES, W. N.; SMITH, D. M. **An introduction to R**. [S.l.], 2007. 105 p. 43

WHIPPLE, K.; DIBIASE, R.; CROSBY, B. Bedrock rivers. In: _____. **Treatise on geomorphology**. [S.l.]: Elsevier, 2013. v. 9, p. 550–573. 15, 16, 70, 73, 112

WHIPPLE, K. X.; FORTE, A. M.; DIBIASE, R. A.; GASPARINI, N. M.; OUIMET, W. B. Timescales of landscape response to divide migration and drainage capture: implications for the role of divide mobility in landscape evolution. **Journal of Geophysical Research: Earth Surface**, v. 122, n. 1, p. 248–273, 2017. 17

WHIPPLE, K. X.; TUCKER, G. E. Dynamics of the stream-power river incision model: Implications for height limits of mountain ranges, landscape response timescales, and research needs. **Journal of Geophysical Research: Solid Earth**, v. 104, n. B8, p. 17661–17674, 1999. 13

_____. Implications of sediment-flux-dependent river incision models for landscape evolution. **Journal of Geophysical Research**, v. 107, 2002. 16

WHITTAKER, A. C.; ATTAL, M.; COWIE, P. A.; TUCKER, G. E.; ROBERTS, G. Decoding temporal and spatial patterns of fault uplift using transient river long profiles. **Geomorphology**, v. 100, n. 3-4, p. 506–526, 2008. 15

WHITTAKER, A. C.; BOULTON, S. J. Tectonic and climatic controls on knickpoint retreat rates and landscape response times. **Journal of Geophysical Research: Earth Surface**, v. 117, n. 2, p. 1–19, 2012. 113

WILLEMIN, J. H. Hack's law: sinuosity, convexity, elongation. v. 36, n. 11, p. 3365–3374, 2000. 111

WILLETT, S. D.; MCCOY, S. W.; TAYLOR PERRON, J.; GOREN, L.; CHEN, C. Y. Dynamic reorganization of River Basins. **Science**, v. 343, n. 6175, p. 1–19, 2014. 1, 17

WOBUS, C.; WHIPPLE, K. X.; KIRBY, E.; SNYDER, N.; JOHNSON, J.; SPYROPOLOU, K.; CROSBY, B.; SHEEHAN, D. Tectonics from topography: procedures, promise, and pitfalls. **Special Paper of the Geological Society of America**, v. 398, n. 04, p. 55–74, 2006. 14, 15, 16, 17, 40

YANG, R.; WILLETT, S. D.; GOREN, L. In situ low-relief landscape formation as a result of river network disruption. **Nature**, v. 520, n. 7548, p. 526–529, 2015. 17

ZONDERVAN, J. R.; STOKES, M.; BOULTON, S. J.; TELFER, M. W.; MATHER, A. E. Rock strength and structural controls on fluvial erodibility: implications for drainage divide mobility in a collisional mountain belt. **Earth and Planetary Science Letters**, v. 538, p. 116221, 2020. 17, 41